# University of Alberta

# Assessment of hyperspectral features and damage modeling in bitumen flotation process

by

**Vivek Bhushan**

A thesis submitted to the Faculty of Graduate Studies and Research

in partial fulfillment of the requirements for the degree of

*Master of Science*

in

*Engineering Management*

Department of Mechanical Engineering



Spring 2011

Edmonton, Alberta

# Examining Committee

*Prof. M.G. Lipsett*

Department of Mechanical Engineering, University of Alberta

*Prof. Rivard Benoit*

Earth and Atmospheric Sciences, University of Alberta

*Prof. D.S. Nobes*

Department of Mechanical Engineering, University of Alberta

# Dedicated to

My parents Rama Kant Pandey and Lalita Devi

# ABSTRACT

Flotation process is mineral processing technique used for separating valuable minerals from the gangue. The research presented in this thesis deals with assessing features that can help in measuring the performance (observing) bitumen flotation process and modeling damage in flotation units.

A timely measure of oilsands and process stream contents can be used to observe and control the separation performance. To this end, flotation experiments were conducted and hyperspectral images of the ore and the process stream were taken to determine whether spectral information can predict the bitumen and fines content of ore samples and establish relationship a between these variables and the froth colour. Several features that appear to correspond to clay and quartz were present.

Flotation cells are prone to wear damage by particles entrained in the slurry. A wear damage model was developed to predict the damage accumulated over a period of time. Particle image velocimetry experiments were conducted on physical flotation model to understand the flow behavior of the solid particles near the wall of the flotation unit. A preliminary wear test was conducted for qualitative assessment of wear. Recommendations were made for validating the damage model.

# ACKNOWLEDGEMENT

No amount of words is sufficient to express my gratitude to Dr. Mike Lipsett, my supervisor for the thesis. His guidance, support and advice have not only helped me through my journey of developing the project and writing the thesis but also have helped me grow as an individual. He has subtly instilled in me some invaluable attributes which I am sure, I will carry lifelong. He deserves special thanks for creating and maintaining an environment conducive to learning and sharing knowledge within the research group and the University at large.

I am sincerely thankful to Dr. Benoit Rivard for giving me an opportunity to work on Centre of Oil Sands Innovation (COSI) project. It was through this collaboration that I was exposed to the world of hyperspectral techniques. His encouragements and feedbacks were truly helpful in seamlessly carrying out the flotation experiments. It was also a pleasure to work with Dr. Jilu Feng, who showed a lot of patience in working with a relatively young researcher and took the time to succinctly explain the hyperspectral imaging and analysis techniques.

The work would not have completed without the generous support and technical advice of Dr. David S. Nobes. His help and guidance in developing the physical model and conducting the PIV experiments was very crucial to the project. I am also indebted to Mr. Alireza Setayeshgar and Mr. Eric Penner for assisting me in PIV experiments.

I would like to specially acknowledge Mr. Bernie Faulkner for unrelenting devotion towards helping students. He has been very cooperative in procurement and assembling parts required for the set of flotation system. Jim Skwarok was very accommodating in providing us the flotation test protocol and advice of the experiment design.

The indirect support and encouragement of my friends; Shishir, Yash, Chaitaniy, Satradru, Manjeet, Samidh, Arjun, and Ganesh has helped me stay focused and motivated. Enrique, Arun, Suheil, Nathan, Ali and Derek made my university life easy. I am also grateful to my family (Bhaiya and Didi) for loving me and supporting me in each walk of my life. Lastly, and most importantly, I want to thanks my parents for bringing me to this world, raising me, supporting me, and being my first teachers. I would not have achieved anything without their selfless, benign love and wishes. I would like to know the reader that unless otherwise stated all the figures in the thesis are produced by me.

# TABLE OF CONTENTS

APPENDIX

# LIST OF TABLES

# LIST OF FIGURES

# NOMENLCLATURE

## *Abbreviations*

CHWE - Clark Hot Water Extraction

PSV- Primary Separation Vessel

FMEA- Failure Modes and Effects Analysis

BEU- Batch Extraction Unit

OSA- Online Stream Analyzer

XRF- X-ray Fluoresce

FFT- Fast Fourier Transform

LDV- Laser Doppler Velocimetry

PIV- Particle Image Velocimetry

ASD- Analytical Spectral Devices

FTIR- Fourier Transform Infra Red

VNIR- Visible near Infra-Red

TBC- Total Bitumen Content

TIR- Thermal Infra-red

***Symbols***

$Q_a$ - Volumetric flow rate

$\omega$ , $n$ -Impeller Speed

$d$ - Impeller diameter

$k$ - Rate constant

$C$ - Concentration

$R$ -Recovery rate

$t$ - Time

$D$ - Tank diameter

$T$ - Tank height

$Q$ - Circulating capacity

$H$ - Velocity Head

$N_Q$ - Pumping Number

Re- Impeller Reynolds Number

$\rho$ - Density

$\mu$ - Viscosity

$N_p$ - Power number

$\varepsilon$ - Molecular energy dissipation

$v_r$ - Radial velocity

$v_t$ - Tangential velocity

$v_z$ - Axial Velocity

$r$ - Radial distance from the impeller shaft

$z$ - Axial distance from the impeller mid-plane

$P$ - Power consumed

$V_F$ - Impeller Discharge

$\Omega_p$ - Angular Velocity of the particle

$B$ - Basset Force

$M$ - Magnus Force

$\alpha$ - Impact angle

$V_p$ - Particle Velocity

$D_p$ - Particle diameter

$Hv$ - Material hardness

$D_p$ - Particle diameter

$Hv$ - Material hardness

**Chapter 1**

# Introduction

In recent years, oilsands have become a valuable and economically feasible source of heavy petroleum. Naturally occurring oilsands are mixtures of sand, clay, water, and extremely viscous form of petroleum, called bitumen. Oil sands, mainly found in Canada and Venezuela, are mined to extract bitumen, which can be processed and upgraded to usable products. Clark Hot Water Extraction (CHWE) process is one of the most widely used methods for separation of bitumen form oil sands and other minerals [1]. The recovery of bitumen from mineable oil sands by the CHWE process is described in the following paragraph.

## 1.1 Clark Hot Water Extraction Process

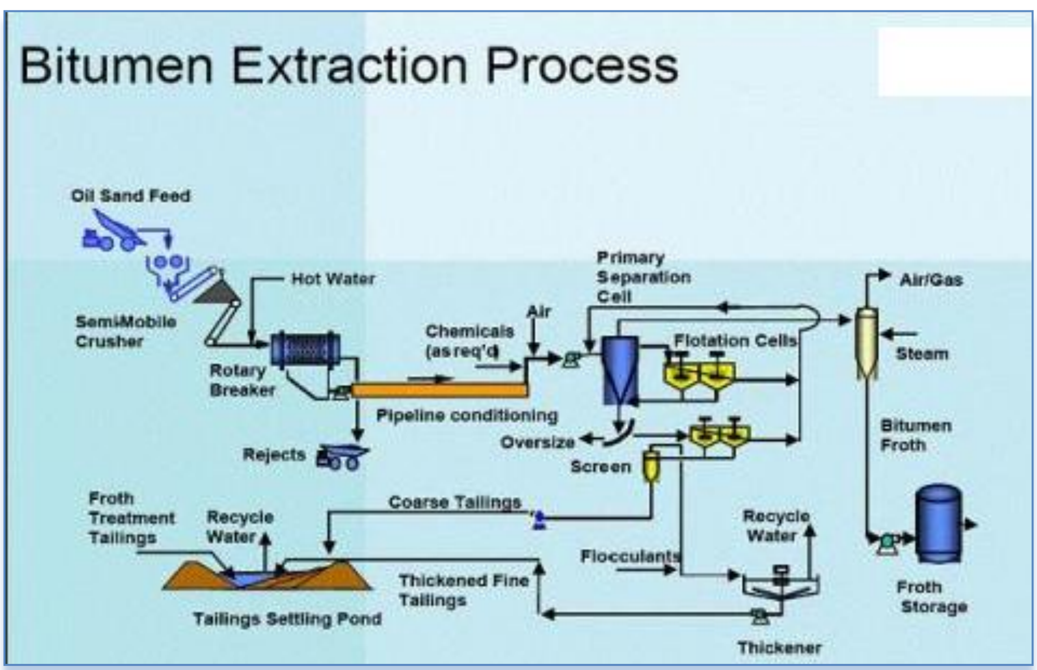


*__Figure 1.1__: Oil sands mining and extraction process schematic (Courtesy: Alberta Innovates-Technology Futures (Appendix A-5))*

Figure 1.1 shows the schematic of the processes involved in oilsands mining and extraction. Conventional open-cast surface mining methods are used in surface mining based bitumen production from oil sands. These methods involve fragmentation and loading by shovels and haulage of ore by trucks to in-pit crushing and slurry transport systems [2]. Hot water and process additives (caustic soda or other reagents) are added to the crushed oil sand in a slurry preparation facility [2]. The warm water promotes ablation of lumps and the generation of natural surfactants in the appropriate water chemistry conditions (aided by addition of caustic or other reagents). Once bitumen is liberated into the water phase, agitation in the pipeline promotes coalescence of bitumen droplets and air attachment (conditioning). The slurry is transported from the mine site to the extraction plant through the hydrotransport pipeline. Hydro-transport conditioning involves separation of bitumen from the sand and fine solids (silts and clays). Short pipelines may not allow sufficient residence time for the oil sand to be fully conditioned. Separation removes sand and clays from the water phase, and bitumen froth is collected as a supernatant. Froth typically contains 60% bitumen, 30% water, and 10% solids [2,3].

Primary separation mostly relies on gravity separation, owing to sufficient density difference between solids, water, and aerated bitumen. The conditioned oil sands slurry is fed into a primary separation vessel or cell (PSV). The bitumen floating at the top is removed and then deaerated, heated and sent to froth treatment units to remove remaining water and solids prior to upgrading. Sand and rocks sink to the bottom of the vessel and are pumped out as a coarse tailings stream. The middlings, containing water, fine solids, small aerated bitumen droplets, and unaerated bitumen droplets, are pumped into secondary separation units for additional conditioning and separation [2]. The froth from secondary units is sent back to the PSV. Secondary separation units are often flotation cells. The work presented is mostly centred on flotation and flotation cells.

Flotation cells are widely used in mineral separation process, especially for low-grade ores in which the average particle size is too small for a gravity separation process. The flotation process typically involves aeration of slurry that is agitated to suspend the solid particles. In most flotation cells, the agitation is achieved using a rotating impeller, as illustrated in Figure 1.2. The suspended solid particles collide with the bubbles, which leads to three-phase contact amongst the bubble, the particle, and the liquid [5]. The reduced apparent density of the resulting particle-bubble agglomerate allows the mineral-laden bubble to rise to the top of the slurry as froth. Minerals are then recovered from the froth. In oil sands bitumen is the material of interests and mineral solids are gangue materials. Overall recovery depends on micro-level processes such as suspension, collision, and adhesion.

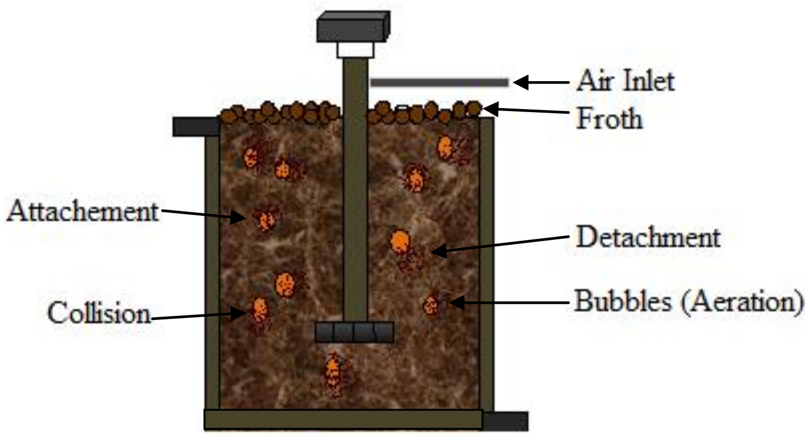


***Figure 1.2***: *Processes involved in flotation*

## 1.2 Motivation for the Present Work

The prime objective of any industrial process is to maximize the profit. The operating profit can be maximized by having an optimal control on the process to enhance the process output. One of the ways to improve the control of a particular process is to explore and deploy additional features (variables) that can be employed in control. In the case of flotation process, observable processibility features can help to improve the recovery from the flotation process by facilitating an improved control. This is the motivation for the first part of the study (discussed in section 1.2.1).

Another way to maximize the profit is to minimize the maintenance cost of the process unit. Timely information of the equipment health can be useful in maintenance scheduling as well as can avert the risk of degraded process performance and unplanned downtime. This leads to the motivation of second part of the work (discussed in section 1.2.2).

### 1.2.1 Processibility Feature

The first part of the thesis concerns observability of a mechanical separation process. Observability means the ability to know how well is the process performing by looking at the outputs of the process. It is difficult to predict the oilsands bitumen flotation performance because the recovery depends not only on the ore type, but also the process conditions for a given process configuration [4]. Improved monitoring and control of bitumen flotation process is essential for improved recovery and froth quality. Controllability of the process is limited by non-observability of features that are known to affect process performance [4]. Currently, open-loop process control is used both for slurry preparation and bitumen separation from slurry. The estimates of the grade and fines content of the ore blend are used to adjust setpoints for water addition rate and addition of process additives such as sodium hydroxide [4]. Adjusting the setpoints based on the actual grade and fines content instead of using estimates would improve the recovery. Hence, there is a need to observe and control the features that affect the recovery and use this for control.

There is strong empirical evidence that the grade-to-fines ratio of oil sands affects how much bitumen is recoverable from the ore [3]; but this relationship is based on estimates of the ore blend based on ore delineation from widely spaced core sampling and shovel locations. This method of estimating the fines content of the ore as it enters the conditioning and extraction processes is at best approximate, given the heterogeneity of oilsands deposits; error arises both from the variability of the ore and variability in the process, as shovel productivity changes and machines are relocated to other parts of the mine [4]. Thus, there is a need to determine some real-time observable features that directly relate to grade-to-fine ratio, and indirectly to the processibility. This would eventually lead to improved control of flotation process. This is precisely the motivation for the second part of the study: to assess whether on-line processibility features might be used to monitor and control separation processes for improved recovery and froth quality.

### 1.2.2 Fault Detection and Modeling

The second part of the thesis pertains to fault modeling in mechanical separation process. A flotation process is usually run in vessels equipped with a motor-driven impeller. Figure 1.3 shows the different mechanical parts of a laboratory-scale flotation cell called a Denver cell. As shown in the figure, the power from the motor is transmitted to impeller shaft via V-belt pulley. The impeller attached to the impeller shaft agitates the slurry in the vessel. Vessels can be of different geometries, often cylindrical..

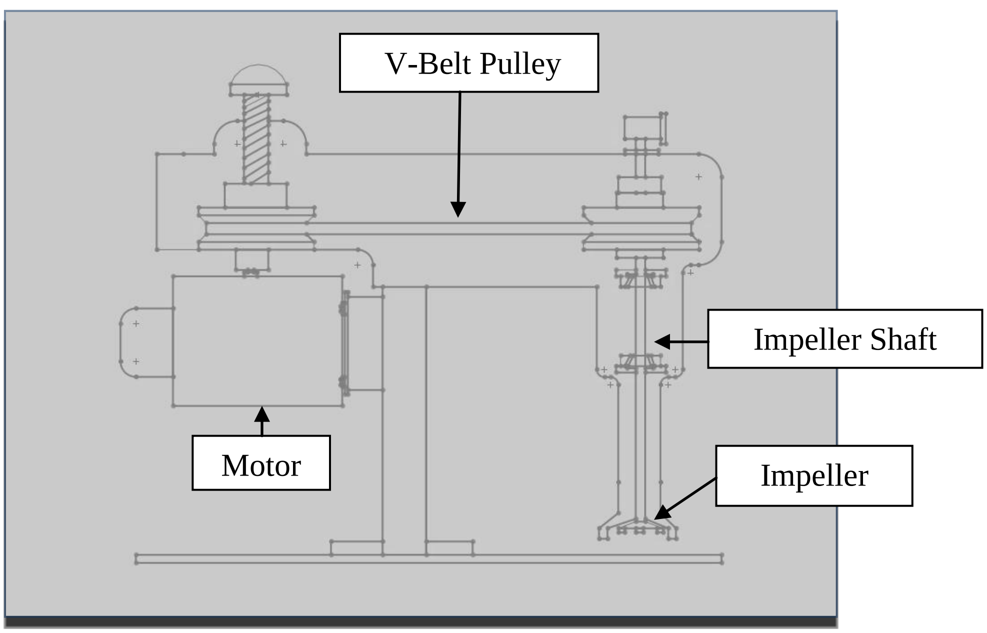


***Figure 1.3:*** *Denver cell schematic*

A flotation cell is subject to different types of faults, such as mass imbalance and misalignment of the impeller shaft, and deformation of the impeller blades. The damage mechanism of interest in this work is wear, which is most prevalent on the walls of the vessel and on the impeller.

Wear occurs in these process units because the process fluid contains solid particles that are entrained with the impeller stream and can contact the impeller or the wall of the vessel. Figure 1.4 shows how an immersed impeller produces a jet that expels fluid (and particles) from the discharge of the impeller. If the particles have sufficient energy, they may transfer some of that energy into the impeller blades or the wall of the vessel, resulting in erosion damage.

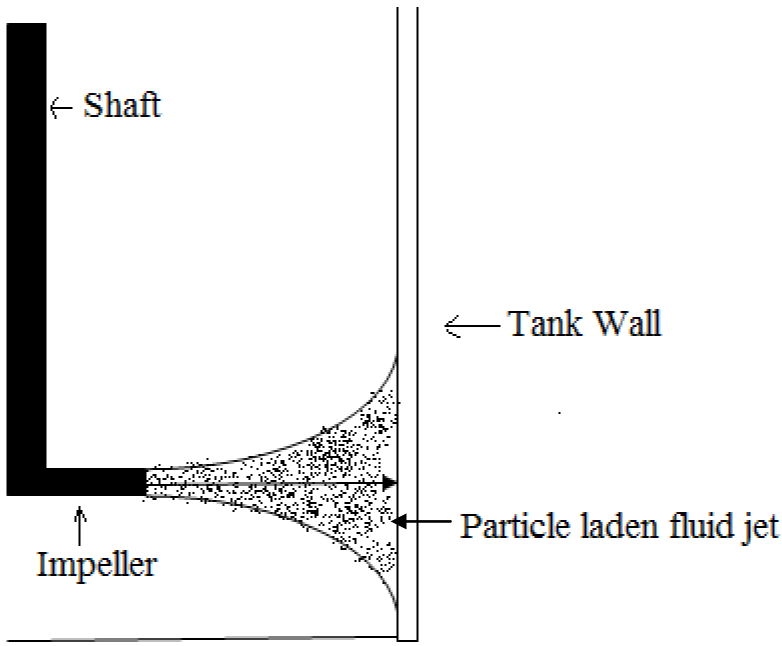


***Figure 1.4***: *Impingement of the impeller jet against the vessel wall*

Wall damage is characterized as a progressive thinning of the shell of the vessel in specific locations, leading eventually to leakage and loss of structural integrity. Impeller damage is a progressive loss of material at different parts of the impeller, such as the leading edge, which reduces the efficiency of the fluid mixing in the cell. If the damage is more pronounced on one blade, then the impeller becomes unbalanced.

Monitoring the condition of a flotation cell is difficult for the following reasons. Most flotation cells are not particularly large, and so they are not typically built with ready access for inspection personnel. Manual ultrasonic wall thickness inspections are time-consuming; inspections often require extensive scaffolding;

and some surfaces may be completely inaccessible, rusty, or covered in dirt. In the case of impeller wear, the process unit must be shut down, drained, and scaffolded for inspectors to gain access for a physical inspection, and so, inspection results are error-prone. Other components are also prone to damage: particle impingement accelerates wear at elbows and valves in the piping system that connects the cell to the rest of the mineral processing circuit.

For both wear-related failure modes, the inspection interval needs to be managed carefully so that the mean time between inspections is shorter than the mean time to failure. Estimating the mean time to failure is the key to a predictive maintenance program; but wear rates are variable, due to the changes in operating conditions and flow rates, and so they not fully predictable. Without a predictive model of damage accumulation, maintenance decision-makers will prefer a condition-based maintenance strategy, provided that there is clear understanding of how to estimate the damage accumulation rate in locations that can not be inspected. This leads to the motivation of developing a predictive model for damage accumulation on the wall of a flotation cell, which is the first part of the work.

## 1.3 Proposed Approach

Erosion is a combined phenomenon of fluid-particle interaction and particle-target interaction. The problem of predicting the erosive damage of the walls was broken down into the following smaller parts:

I. Modeling the fluid flow in a flotation cell
II. Predicting the motion of abrasive particles under the fluid field. Hence, the impact velocities and the impact angle at the surface of the walls.
III. Determining the amount material removal using an appropriate wear model and the impact velocities and impact angles found in step II.

Using the above steps, material lost by abrasive particles in the flow field can be predicted. In order to determine the overall damage accumulation at the locations of interest, the individual wear events must be connected together over a period of time. This was achieved by first calculating the damage on a cylindrical strip of unit thickness based on the particle concentration in the slurry and the impact frequency of the particles. The physics of failure approach was used to understand the damage mechanism. Understanding of the damage mechanism was useful to develop a model for damage rate. The damage accumulation was eventually estimated by integrating the damage rate over the period of interest.

A timely estimate of bitumen and fines content in the ore and the process stream can be used to improve the processability as discussed in the motivation section. Reflectance hyperspectral analysis of the ore and the froth has been successful in predicting the composition of the contents in various minerals processing. Reflectance hyperspectral analysis of being capable of estimating bitumen content and fines fraction in real time from a small set of spectral features was established by Rivard *et.al.* [6,7] and Rogge *et.al* [8]. The objective of the study was to determine whether hyperspectral features of the ore and the process streams were used to relate the observable features such as color of the froth, froth quality etc. to the processibility. To this end, flotation experiments were designed and conducted to compare hyperspectral data collected during batch extractions for ores exhibiting poor recovery and samples with good recovery. Hyperspectral images were taken on the froth at two stages: in-situ (from the surface of the froth layer while the froth was in the separation cell) and after froth sample collection. Hyperspectral features which enabled the classification of ores and the froth quality based the recovery performance were extracted to build a classification model.

## 1.4 Thesis Outline

The research reported in the thesis considers with two aspects of mechanical flotation: a) modeling of wear damage in flotation cell; b) assessing whether on-line processibility features could be used to monitor and control the recovery performance. Chapter 2 is a literature review on specifics of mixing/flotation process and wear. It starts with a short description of flotation process, flotation of bitumen and use of hyperspectral imaging in controlling the process. It then moves on to explaining the design of mixing vessels, the flow modeling in mixing vessels. This is followed by a short description on common failure modes in flotation cell, types of wear and wears modeling. Chapter 3 considers flotation observability and deals with the solution approach, methodology, experimental design, apparatus development, experiments, result, and discussion for the second objective of the study. Chapter 4 is devoted to wear modeling in flotation cell. It starts with model development and then proceeds into experimental design for model verification and discussions of results of flow analysis in a physical model and implications of developing a combined process and wear model. A preliminary verification based on the multilayer paint scheme is also presented. Chapter 5 presents some conclusions and recommendations for future work.

# References:

[1] SYNCRUDE website. (www.syncrude.com) (Date accessed: 12.12.2010)

[2] Kasongo T, Zhou Z, Xu Z, Masliyah J. Effect of clays and calcium ions on bitumen extraction from athabasca oil sands using flotation. Can J Chem Eng. 2000;78(4):674-81.

[3] Zhou Z, Kasongo T, Xu Z, Masliyah J. Assessment of bitumen recovery from the athabasca oil sands using a laboratory denver flotation cell. Can J Chem Eng. 2004;82(4):696-703

[4] Dr. M.G. Lipsett's project proposal to Centre of Oil Sands Innovation.

[5] Bloom, F., & Heindel, T. J. Mathematical modelling of the flotation deinking process. *Mathematical and Computer Modelling* 25 (5), 13-58, 1997

[6] Rivard, B. Feng, J., Lyder, D., Gallie, A., and Cloutis, 2007a. Rapid characterization of oil sand properties using near infrared and thermal infrared reflectance spectroscopy." 57th Canadian Chemical Engineering Conf. Sept. 2007.

[7] Rivard, B, Lyder, D, Feng, J., Gallie, A., and Cloutis, E. 2007b. Determining bitumen content from reflectance spectra of oil sands using wavelet, singlet, and broad band analysis. 9th Geoide annual conference. Halifax, NS, June 6-8.

[8] Rogge, D., and Rivard, B. 2008. "Applications of imaging spectroscopy to the characterization of rock and oil sand core." Proc. CIM Conf Edmonton, May 4-7 2008, session exploration and innovation 2.

**Chapter 2**

# Literature Review

The study presented in the thesis deals with bitumen flotation processes with an objective of maximizing the profit by looking into two aspects of flotation:

1) Process observability- New ways to observe the process can be useful in improving the control over the process. In an attempt to explore new observable features bitumen flotation process was studied and experiments were conducted to assess if reflectance hyperspectral features of the ore and process stream relate to the processability.

2) Damage modeling and prognostics – A timely estimate of equipment health leads to improve maintenance decision. To estimate the damage accumulation of a period of time, wear by solid particle impingement was modeled.

For the first part of the work, it is necessary to understand the details of the flotation processes by considering the key sub-processes, reagents requirements, conditions required for optimal recovery. This understanding was used in experimental design and apparatus development. This is followed by identifying technological gaps in the current ways of controlling the bitumen separation process and establishing how an additional set of observable features based on hyperspectral analysis of the ore and froth can help in bridging the gaps.

Flotation process units can be approximated as mixing vessels for the purpose of modeling wear, with the assumption that bubble generation does not affect the motion of fluids and the undesirable solid particles. Knowledge of the design of mixing vessel, such as geometric parameters and impeller characteristics is important for the development of the fluid flow modeling the vessel. The same knowledge was also used for experimental design and execution.

Failure modes and effects analysis (FMEA) were conducted to present the common failure modes in flotation cells. Since damage due to erosive wear was a failure mode of interest, a short literature survey is presented before delving into particulars of wear types of interests and their models.

## 2.1 The Flotation Process

In the flotation process, air bubbles are injected into the slurry agitated by an impeller. The agitation keeps the solid particles in suspension. The degree of suspension depends on the size and density distribution of the solids. The particles collide with the rising bubbles and depending on the surface characteristics may get attached to the bubbles. The particles therefore are carried upward to the top of the vessel where they are skimmed mechanically or by overflow.

### 2.1.1 Types of Possible Phases in Flotation Cell

The phases within the cell are usually divided into four zones: pulp, bubble, froth, and entrained [1]. Figure 2.1 illustrates these phases.

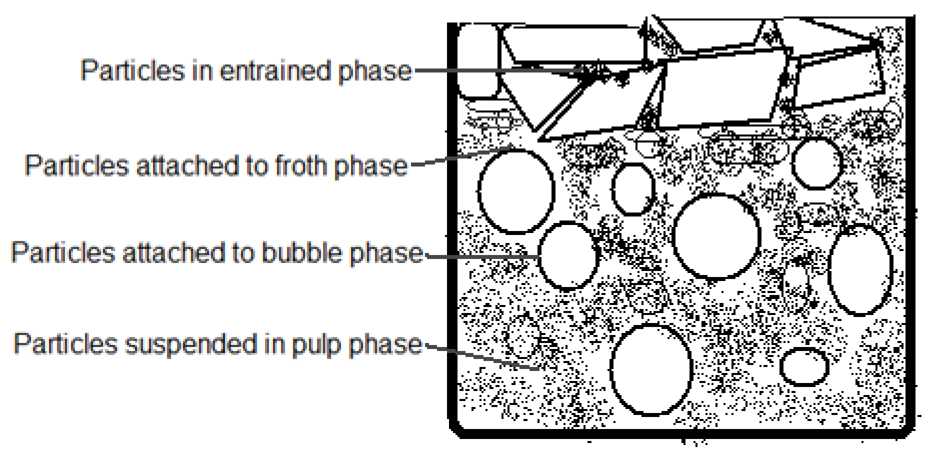


***Figure 2.1:*** *Types of phases in flotation*

<u>*Pulp Phase*</u>*:* Solid particles are suspended throughout the pulp by the help of an agitator. The pulp phase is also aerated so that the bubbles are formed

continuously and rise through the pulp. Particles can leave the pulp phase either by collision and attachment to a bubble or by entrainment at the pulp-froth interface. In oil sands flotation, bitumen droplets are the particles of interest. There are other gangue materials and solids too. The gangue are the rejects from the process.

*Bubble phase:* This phase consists of clouds of rising bubbles through the pulp phase. In the process they get laden with particles.

*Froth Phase:* The particle laden bubble enters the froth phase after successfully crossing the pulp-froth interface. Here the liquid drains from the surface of the bubble which makes them thinner and they break causing it to coalesce with the adjacent bubble to coalesce. The liquid drains and the particles attached to the surface of the bubbles in the froth move with the froth until it passes over the lip of the flotation cell in concentrated forth form. Some particles can be detached from the liquid film in the process.

*Entrained phase:* Some particles are entrained in the plateau borders of the froth. These particles have a tendency to move down towards the pulp-froth interface under the influence of the gravity.

### 2.1.2 Flotation Reagents

Flotation reagents are the chemicals added to the slurry to enhance the rate of flotation process. There are three general types of chemicals used in flotation [2]: collectors, frothers, and modifiers.

*Collectors:* These organic chemicals make the surface hydrophobic and make the minerals being capable of being collected together.

*Frothers:* These organic chemicals reduce the surface tension of water to stabilise the bubbles in the froth layer at the top of the flotation cell, making concentrate removal easier.

*Modifiers:* These are the chemicals used to modify the slurry conditions to enhance the difference in surface chemistry between the valuable and gangue minerals.

### 2.1.3 Factors Affecting Flotation Recovery

The recovery performance of flotation depends on the aeration, impeller speed, suspension, and particle size distribution. The effect of these factors on the recovery is discussed below.

*a) Aeration*: It is generally observed that at a given impeller speed, the rate constant for a given species increases with increasing airflow rate [1]. This is because more surface area bubbles are exposed to the suspended solid particles, leading to greater rate of particle-bubble attachment. Effective aeration also provides stable froth of reasonable depth [1]. With increasing air rate the power consumption decreases as more space in the cell is occupied by the gas, reducing the force of the impeller on the fluid. Excessive gas addition is undesirable because the liquid volume fraction and the liquid circulation rate are impeded. Gas retention time should be enough to allow the mass transfer [2] and successful rising of the particle-laden bubble through the pulp phase into the froth phase.
The effect of volumetric air flow rate, $Q_a$ on the formation and number of bubbles is described in terms of dimensionless air-flow rate $Q_{vl}$ [1], defined as:

$$Q_{vl} = Q_a / \omega D^3 \tag{2.1}$$

where, $\omega$ is the angular speed of the impeller in radians per unit time, and $D$ is the impeller diameter. For small values of air-flow number, the number of bubbles and the mean bubble size is small. As the air-flow number increases, the size and the number increases. At large gas rates, the phenomenon called flooding occurs, which is marked by sudden drop in the power consumption. During flooding very large bubbles are formed, resulting in loss of adequate gas holding properties and liquid pumping. For good operational performance gas flow rate should be below the flooding gas velocity [1].

*b) Impeller speed*: The rotational energy of impellers is the prime source of energy in the flotation cell. Hence, its speed must be enough to support effective suspension of the solid particles in the cell, disperse air into bubbles, and provide sufficient turbulence for bubble-particle collision [3]. It has been observed that increase in impeller speed improves each of these performances leading to a better recovery [1]; however, beyond a certain speed, the turbulence becomes so strong that the hydrodynamic shear forces disrupt the particle bubble collision and attachment, sometimes leading to detaching the particle from the bubble. This sets the boundary for optimal impeller speed.

*c) Suspension*: It is required that an impeller or air jet of the machine keeps the solids in the pulp in suspension. If the degree of agitation is not sufficient, then the solids will tend to settle out. A significant sanding of the floor upsets the pulp flow pattern within the cell and prevents the proper contact between suspended particles and air bubbles. Particles not in suspension cannot make effective contact with air bubbles [2].

*d) Particle Size*: The probability of collision and adhesion of a particle with a freely moving bubble varies with the particle size because of the following reasons [2]:

i) Particle projected area, normal to the direction of motion

ii) Particle inertia, which determines whether it will be able to cut through the thin fluid film around the bubble

iii) Possibility of getting detached from the bubble due to high hydrodynamic shear forces

iv) Extent to which collision may distort the bubble and alter the time of contact (or even cause the bubble to break apart)

In general, coarser particles tend to become concentrated in the lower parts of the cell where the chances of collision are greatly reduced. In any given cell, there is a maximum size beyond which the particles cannot be floated due to the disruptive forces resulting from the turbulence of the pulp. The possibility of getting detached after collision and attachment decreases with the decreasing size. In practice, the different sized particles of the same mineral under the same chemical conditions may have different rate constants. The actual affect for different minerals can be assessed by carrying out laboratory experiments [2].

### 2.1.4 Kinetics

The mineral obtained from a batch operation of the flotation cell changes with time as the particles floating change in size, grade and quantity [2]. If $C$ is the concentration of the valuable material remaining in the cell at time $t$, then the equation for the flotation rate is given by:

$$-\frac{dC}{dt} = kC^n \tag{2.2}$$

where $k$ and $n$ are the rate constant and order of the reaction respectively.

<u>*First order rate equation*</u>: With , $n = 1$, the integration of the above equation will yield

$$C = C_0 e^{-kt} \tag{2.3}$$

where $C_0$ is the concentration of the valuable mineral in the cell at zero time. The recovery $R$ is defined as:

$$R = \left( \frac{C_0 - C}{C_0} \right) \tag{2.4}$$

and after prolonged flotation times, the ultimate recovery is:

$$R_\infty = \left( \frac{C_0 - C_\infty}{C_0} \right) \tag{2.5}$$

where $C_\infty$ is the concentration of the valuable mineral that has not reported to the surface of the cell after an infinite flotation time. The first order equation can be then written as:

$$R = R_\infty (1 - e^{-kt}) \tag{2.6}$$

The derivation assumes that the only independent variable is the amount of floatable material. If factors such as bubble concentration, size and size distribution, reagent concentrations, and cell operating conditions change with time, then the rate equation takes the following form:

$$-\frac{dC}{dt} = k \prod C_i^{n_i} \tag{2.7}$$

where $C_i$ is the concentration of any species present in the slurry that might change the rate of flotation of the desirable species and $n_i$ is the order of the equation with respect to $C_i$ .

For a flotation test, we assume that the reagent concentrations and other variables remain constant, with the exception of air bubbles population and size and the population of floatable particles, in which case, the equation simplifies to:

$$-\frac{dC}{dt} = kC_s{}^m C_a{}^n \tag{2.8}$$

where $C_a$ and $C_s$ are the concentration of air bubbles and floatable particles [2].

### 2.1.5 Flotation of Bitumen

Clark hot water extraction (CHWE) process is commercially used for separation of bitumen form sand and other minerals. The open-pit mined oil sands are digested and aerated in a tumbler with hot (80°C) or warm (50°C) water [3]. A small amount of caustic (NaOH) is added to encourage the liberation of bitumen from other fines and solids. The conditioned slurries are then feed in primary separation vessels (PSV) where float to the top by engulfing the air bubbles [4]. Middling from the PSV are feed into flotation cells while the tailings from PSV and flotation units are discharged into tailing ponds [3, 4].

Flotation of oil sands is different from other mineral processing for the following reasons:

1) Bitumen can produce natural surfactants, which facilitate bubble formation and bitumen attachment to the bubbles;

2) The temperature requirements for oil sands flotation are higher than other minerals, to break up lumps of oil sand and to generate surfactants. The bitumen droplets also become less viscous at higher temperature;

3) Bitumen droplets can coalesce to form larger drops, provided that temperature allows for reduced viscosity and favourable interfacial & hydrodynamic conditions exists.

Bubble break up is relatively low possibility because of the presence of surfactants. Recovery from flotation process is the result of particle-bubble attachment hydraulic circulation [3]. Since both the gangue and the bitumen can be carried to the top, true recovery from a batch flotation process follows a first order kinetics and is given by [5]:

$$R_{true} = R_{\infty}[1 - \exp(-k(t + \phi))] \tag{2.9}$$

where $R_{\infty}$ is the maximum recovery after infinite flotation time, $k$ is the first order rate constant, and $\phi$ is the zero time correction factor which is the time taken for the process variables to stabilize at the set points.

Experimental techniques and design of experiments

Batch extraction units (BEU) developed by Sanford *et al.* [6] have been extensively used for laboratory scale testing of oil sands processibility [3,4]. The BEU, gives information about the overall recovery, but it is not very useful in investigating the flotation kinetics [3]. At operating temperatures less than 50 degree Celsius, the tests becomes less sensitive [4]. To overcome these issues, a laboratory Denver Flotation unit of approximately 1 litre capacity is used for bitumen flotation experiments [4]. A metal jacket is fabricated around the cell and is connected to a temperature control thermal bath. The temperature of the slurry inside the vessel is controlled by regulating the temperature of the water circulating in the jacket. Aeration can either be staged or continuous. In a continuous aeration scheme, 300 grams of oil sands is added to 950 ml of untreated tap water [7]. The first 5 minutes of the run time is conditioning stage and for the next 10 minutes the froth is collected in two equal intervals of 5 minutes. The bitumen, solids, and water content in the ore and the froth are analysed using standard Dean-Stark Method developed by Bulmer et.al [8].

### 2.1.6 Flotation Process Observability and Potential Use of Hyperspectral Imaging

The objectives of flotation control are: 1) stabilizing the process at desired levels, 2) achieving the expected grades or recovery, and 3) maximising the profit by optimizing the process [13,14]. The exercise of controlling the process starts with stabilizing the process and then moving to a desired set point without undergoing considerable change in the concentrate grade [12]. The ultimate goal is to achieve optimal control, which yields a greater recovery at higher concentrate grade [12].

The control of flotation process has been a challenge because of the following points [9]:

1) The process is highly multivariate, with a number manipulated variables including slurry feed from the grinding section, air, water, and process additives such as frother, collectors, etc.
2) The process is subject to various disturbances such as particle size distribution, ore content (chemical and/or physical), air temperature, oxidation state, and step changes during manual operating procedures.

These factors make it difficult to control and predict the recovery performance. Automatic control systems such as online stream analyzers (OSAs) are in place in many flotation process plants but are not robust enough to cater to all the variations without human intervention. In the case of oil sands, assaying is done off-line except where on-line analyzers are used to estimate the bitumen losses in tailings [57]. X-ray fluorescence (XRF) has been traditionally used for online assaying of flotation process streams especially in base metal mineral processing [15]. OSAs are also expensive and difficult to maintain [11]. Furthermore the sampling times of OSAs (10-20 min) are long as compared to the dynamic disturbances [9]. Heuristic control methods based on visual observations have also been used to adjust operating setpoints. Heuristics based control methods have been successful because flotation recovery performance bears a correlation with the froth visual characteristics [16,17]. Heuristics methods suffer from subjectivity of the operators and also may not be precise. Hence, there is a need to explore additional set of features that can be used to monitor and control the flotation performance.

For the above mentioned reasons, the colours of the froth have been a subject of investigation. Analysis of colour, structure, and morphology of froth by image processing has been widely studied as candidates providing features for analyzing the process state [8,18] . Froth images features reflect important process states and react to the changes in manipulated variable [9]. In spite of the advantages, very few real applications have used the colour characteristics for analysing the grade of froth and slurry [12]. This offers opportunity for research.

With recent advancements in the field of reflectance spectroscopy, measurements of color have greatly improved [12]. Hence, reflectance spectroscopy has potential application in froth image analysis. Images of the froth are taken in-situ followed by segmentation of images [19]. Segmentation gives way to feature extraction from the froth image such as bubble size, texture, minerals contents in the bubble [20,21]. Statistical properties of the image have also been used to analyse the froth [12] such as Fast Fourier Transform (FFT) of the image features by Moolman *et* *al.* [22] and multivariate image analysis [18]. Colour of the froth has been utilized for assaying purposes [12]. For example Gebhardt et.al [23] used a sensor for measuring color as adjustable linear combination of red, green, and amber [12]. The combination correlated well with the mineral contents in the ore as well as in the froth. Hargrave et.al [24] examined the features in the froth from coal flotation to establish a correlation between the gray level distribution and the ash content in the froth.

Infrared reflectance spectroscopy has been used in a variety of investigations such as studies on the variations of oil sand slurry, the mineralogy of oil sands, bitumen characteristics, and bitumen content in ground ore [25]. The hyperspectral analysis of the froth in relation to processibility of oil sands is however new and is the scope of the present study. The details of hyperspectral technologies and techniques used for oil sands are provided later in Chapter 3, section 3.1.1.

## 2.2 Mixing Vessel: Design and Flow Fields

Mixing vessels are widely used in the process industry for mixing, dispersion and suspension of liquid-liquid, liquid-solids and liquid-gas-solids mixtures. A flotation process includes mixing to promote air attachment but mixing should not be so vigorous that aerated bitumen can separate as froth. Some important design parameters and flow characteristics in mixing vessels as discussed in reference [29] are briefly explained in the flowing section.

### 2.2.1 Design of Mixing Vessel

Achieving the right blend (mixing), right degree of solids suspension (lifting of solids) and, optimal mass transfer rates are some of the objectives of mixing process. The objectives dictate the design of mixing systems. Optimum design also involves design of mechanical components such as impeller shaft diameter, impeller, baffles, bearings, seals, etc.

Mixing process units are usually equipped with a rotary mixer. The rotating mixer comprises an impeller, shaft, shaft seal, gearbox, and a motor drive. Baffles are installed to achieve transitional or turbulent flow during mixing process. Baffles also facilitate a high level of axial mixing. Figure 2.2 shows the notations used to define the geometric parameters: D and d are the tank diameter and the impeller diameter respectively; C is the off-bottom clearance defined as the distance between the bottom of the tank and the impeller mid-plane; and T is the tank height. These geometric parameters are related to each other based on the process requirements.

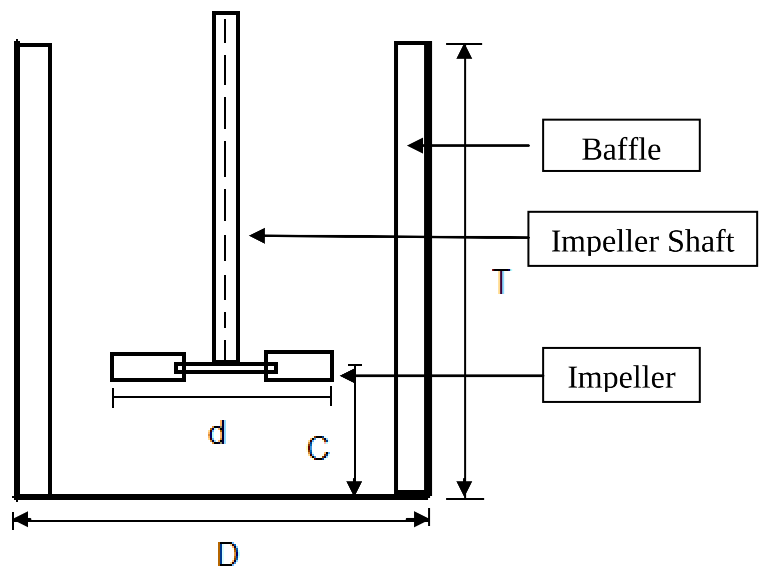


***Figure 2.2***: *Mixing vessel*

#### 2.2.1.1 Impeller

The impeller determines the flow pattern, flow regime and the shear level in the mixing process. Table 2.1 gives the classification, applications and examples of impellers based on the flow pattern and shear level [29]. The flow pattern developed by an axial impeller consists on two axial loops on either side of an impeller shaft. Figure 2.3 below shows the flow patterns for radial and axial impellers. Flow pattern from a radial impeller consists of an impeller jet emanating from the impeller, two circulation loops (one above and the other below the impeller plane) on each side of the impeller shaft.

***Table 2.1*** *-Impeller types and characteristics*

| Impeller Type | Characteristics/Applications | Examples |
|---|---|---|
| Axial Flow Impeller | • High circulation level, less shear<br>• Blending, solids suspension, solids incorporation, gas | Propeller, pitched blade turbine |
| Radial Flow Impeller | • High shear and turbulence levels, lower pumping<br>• Gas–liquid and liquid–liquid | Flat-blade impeller, disk turbine (Rushton), hollow- |
| Hydrofoil Impeller | • Axial flow, less shear<br>• Liquid blending and solids suspension | Lightnin A310, Chemineer HE3, EMI Rotofoil |
| High-shear Impeller | • High shear, low pumping<br>• Addition of second phase in grinding, dispersing pigments, and making emulsion | Chemshear impeller, Bar turbine, Sawtooth Impeller |

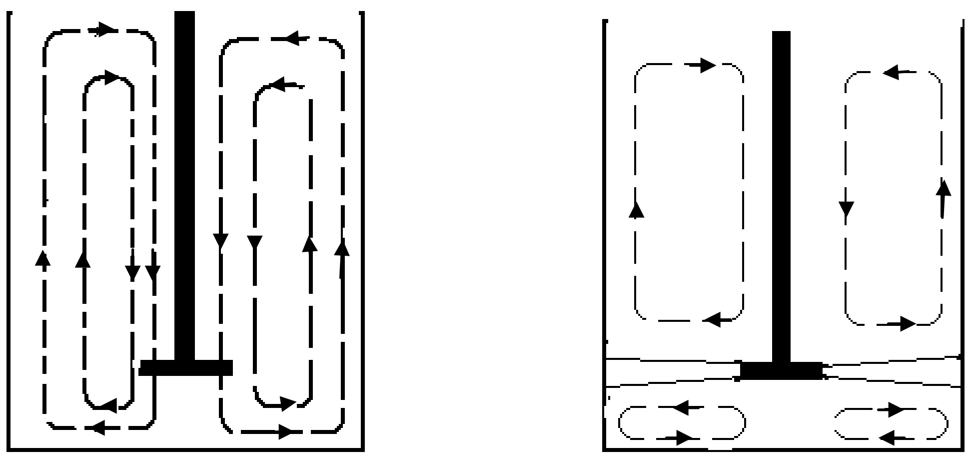

***Figure 2.3:*** *Flow Pattern from Axial Impeller (left) and Radial Impeller (right)*

### 2.2.1.2 Impeller characteristics: Pumping and Power

The power input to the mixing system gives rise to a circulating capacity (pumping) $Q$ and a velocity head $H$. $Q$ represents the volume discharged by the impeller while velocity head $H$ provides the kinetic energy that provides the shear. At molecular level this shear provides the molecular kinetic energy which is eventually dissipated by turbulence. Circulating capacity $Q$ and the head $H$ are given by

$$Q = N_Q n d^3 \tag{2.10}$$

and

$$H = n^2 d^2 \tag{2.11}$$

where $n$, $d$ is the impeller speed and diameter respectively. $N_Q$ an empirical pumping number that depends on the impeller type, vessel diameter to vessel height ratio (D/T), and impeller Reynolds number ($\mathrm{Re}$) given by

$$\mathrm{Re} = \frac{\rho n d^2}{\mu} \tag{2.12}$$

where $\rho$ and μ are the density and viscosity of the fluid respectively. Pumping numbers ($N_Q$) for various impeller types under turbulent conditions are given in Table 2.2 [29].

***Table 2.2:*** *Pumping number for different impeller types*

| **Impeller Type** | **Pumping number ($N_Q$)** |
|---|---|
| Pitched blade turbine | 0.79 |
| Propeller | 0.4–0.6 |
| Hydrofoil impellers | 0.55–0.73 |
| Retreat curve blade | 0.3 |
| Flat-blade turbine | 0.7 |
| Disk flat-blade turbine (Rushton) | 0.72 |
| Hollow-blade turbine (Smith) | 0.76 |

Power consumed by the impeller is the product of the pumping ($Q$) and the head $H$, and can be expressed as

$$P = Q \times H = \frac{N_p \rho n^3 d^5}{g} \tag{2.13}$$

For the same amount of pumping and head a higher power number ( $N_p$ )would mean greater consumption of power. Figure 2.8 shows the power number at different impeller Reynolds number for various impellers. A good treatment on dependence of $N_p$ on geometry and impeller Reynolds number is presented in [29].

## 2.2.2 Flow Field in Mixing Vessel

The flow field in a flotation vessel can be generalized with one in a mixing vessel, with assumption that the bubble generated in the flotation vessel does not interfere with the flow pattern. Mathematical models of the flow field in an agitated vessel can be formulated by either of two general approaches [31]:

1) models based on numerical solutions of the Navier-Stokes equations (with various forms of k-$\varepsilon$ turbulence model, which include transport terms for the kinetic energy and dissipation energy due to turbulence); or

2) models that divide the tank into characteristic regions with different velocity profiles in different regions.

### 2.2.2.1 DeSouza & Pike Model

In the DeSouza & Pike [32] model a set of regions is used for modeling the flow, using approximated solutions of the velocity distribution developed either empirically or analytically by solving simple balance equations.

One of the earliest attempts to model the flow in stirred tanks with a radial flow impeller using approach 2) was made by DeSouza *et al.* [32]. They proposed that since different types of flows; (tangential jets, stagnation flows, irrotational flows) exist in the tank, the tank can be divided into various regions to model the flow as illustrated in Figure 2.4. The regions are as follows:

I. Tangential jet originating from the impeller

II. Impeller discharge impinging the wall modeled as stagnation flow
III. The corners of the tanks as potential flow
IV. The top and the bottom of the vessel near the tank axis modeled as potential flow
V. The area around the tank axis as circular jet
VI. The two doughnut shaped regions with no fluid circulation

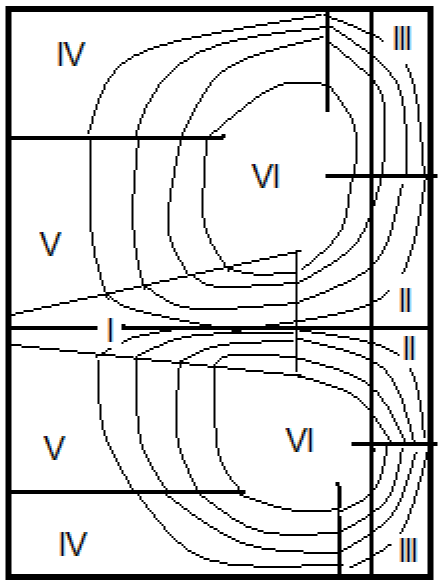


***Figure 2.4***: *Different fluid zone generated by radial flow impeller ( redrawn from [32])*

Using continuity and momentum equations and assumptions of steady state, axial symmetry, incompressible and turbulent flow, DeSouza *et al.* [32] developed a tangential jet model to describe the flow from the impeller. The present study concerns the impeller jet only; its motion is given by following set of equations for the radial ($v_r$), tangential ($v_t$), and axial ($v_z$) velocity components as function as a function of axial distance:

$$v_r(r,s) = V_{\max}[1-\tanh^2(\eta/2)] \tag{2.14}$$

$$v_t(r,z) = v_r \tan\theta_y \tag{2.15}$$

$$v_z = -\frac{V_{\max}}{\sigma}\left[\frac{2r^2 - a^2}{r^2 - a^2}\tanh(\eta) - \eta[1 - \tanh^2(\eta/2)]\right] \tag{2.16}$$

where

$$V_{\max} = 1/2A(\sigma/r^3)^{1/2}(r^2 - a^2)^{1/4} \tag{2.17}$$

$$\eta = \frac{\sigma z}{r} \tag{2.18}$$

$$\theta_y = \tan^{-1}[a/(r^2 - a^2)^{1/2}] \tag{2.19}$$

The three parameters in the model $a, \sigma$ and $A$ where found by velocity measurements of the impeller stream as:

$$\sigma = 12.621 \tag{2.20}$$

$$a = 0.06924(D - d)/D \tag{2.21}$$

$$A = 1.1436[nd^3/(R^2 - a^2)^{1/4}]^{0.8337} \tag{2.22}$$

### 2.2.2.2 Platzer Model

Platzer *et al* [31] divided the tank into three regions contending that models with 6-8 regions are not fit for practical applications because they involved too many parameters. Platzer *et al* [31] modeled the local distributions of the velocity components in stirred vessels with radial or axial flow with different ranges of Reynolds number (laminar, transition and turbulent). The three tank regions have the following characteristic flows.

i. Rotational flow: fluid moving concentrically with respect to the impeller rotation, ;
ii. Circulating flow: loops above and below the impeller with axial velocity having self-similar velocity profiles with varying axial distance (z); and
iii. Impeller jet: tangential flow from the impeller discharge moving radially to the vessel wall.

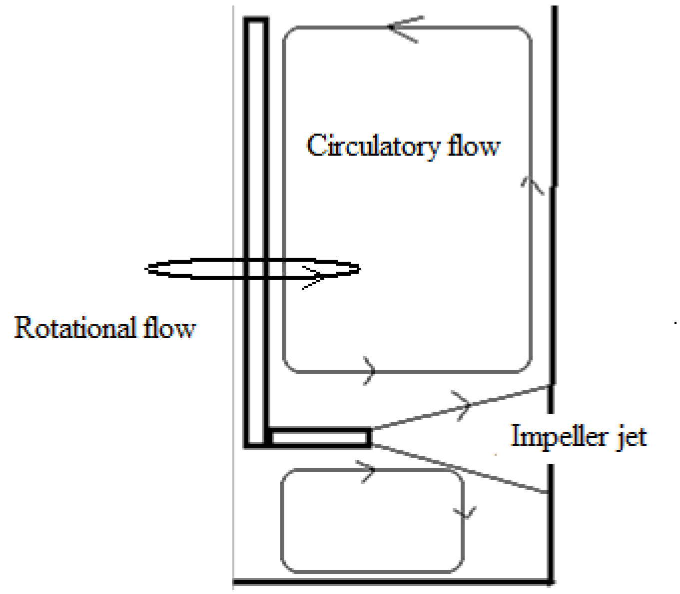


**Figure 2.5:** Flow regions

For each of these regions, shown in Figure 2.5, parametric equations of the flow were developed using continuity and momentum balance equations, the velocities of characteristic points, and analysis of experimental data at points where the velocities were measured. For each of these flows they analysed the existing experimental data and provided the model formulation.

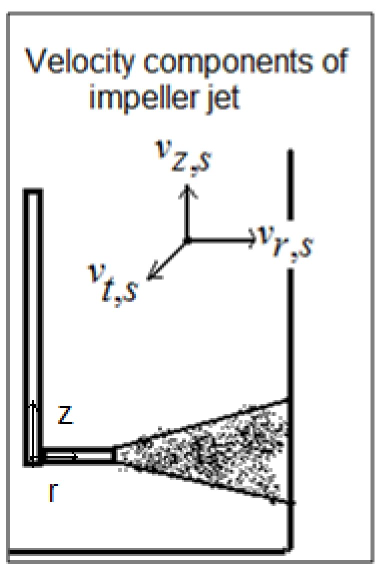


**Figure 2.6:** Velocity components in Impeller Jet

For the impeller jet region (as shown in figure 2.6), they modified the three tangential parameters as:

$$\sigma = 19\exp(-0.108c_p) \tag{2.23}$$

$$2a/d = \begin{cases} [B'/(1+B')]^{0.5} & B' < 2 \\ 0.816 & B' \geq 2 \end{cases} \tag{2.24}$$

$$B' = \left\{ \frac{1.772\tanh[\sigma w/(2d)]}{c_F(\sigma/c_p)^{0.5}} \right\}^4 \tag{2.25}$$

$$A/nd^2 = \begin{cases} 0.282[(c_p \frac{d}{2})/a]^{0.5} & \text{B'}<2 \\ \frac{0.21\text{c}_\text{F}\sigma^{0.5}}{\tanh[\sigma w/2d]} & \text{B'} \geq 2 \end{cases} \tag{2.26}$$

where $A$ and $a$ are geometry-dependent parameters, $c_F = v_F / nd^3$ is the coefficient of discharge, $c_P = P/\rho n^3 d^5$ is the power number, $n$ is the impeller speed (rps), $P$ is power consumption, $V_F$ is the impeller discharge per second, $w$ and $d$ are the impeller blade width and impeller diameter respectively, $\text{Re} = d^2 n\rho/\mu$ is the impeller Reynolds number.

Although Platzer *et al* [31] found good agreement in estimating parameters for the individual regions, each region was modeled independently from each others, resulting in a lack of interconnection between the regions and discontinuities existed at the transition from the jet region to the circulating region. The model does not take into account near-wall effects such as the presence of boundary layers and other particle interaction forces, for example Basset and Magnus forces.

Basset forces are the forces due to lagging boundary layer development when the relative velocity of a fully submerged solid changes with time [33]. Basset forces can be significantly large when the acceleration of the relative velocity is large. Mathematically, the force is expressed as:

$$B = -6\pi\mu r_p \left( v_p + \frac{r_p}{(\pi \frac{\mu}{\rho})^{0.5}} \int_{t_0}^{t} \frac{v'_p(t_1)}{(t-t_1)^{0.5}} dt \right) \tag{2.27}$$

where $r_p$ is the particle diameter, $v_p$ is the particle velocity, and $v'_p$ is the particle acceleration.

Magnus forces are the forces acting perpendicular to the line of motion of a rotating solid. The force is the result of differential pressures acting along the edge of the solid [33]. The force can be expressed as:

$$M = \pi\rho(r_p)^3\,\Omega_p \times v_p \tag{2.28}$$

where $\Omega_p$ is the angular velocity of the particle. If the angular velocity is high, Magnus forces will substantially affect the motion of solids.

## 2.3 Damage of Flotation Cell

Process output depends on the health of a machine while the health of the machine deteriorates with time. It is thus necessary to keep a track of the equipment health and ensure that the machine does not fail leading to downtime losses. Some of the ways in which Denver Cell can be damaged are given in the Table 2.3 with the possible causes and effects.

The damage mechanism of interest in this work is wear by particle impingement (erosion), which is most prevalent on the walls of the vessel and on the impeller. The following section presents modeling erosion with a short introduction on wear, its types and related damage mechanisms.

***Table 2.3:*** *Common Fault Modes, Causes & Effects of Denver Cell*

| **Faults mode** | **Causes** | **Effects** |
|---|---|---|
| **Impeller damage** | • Worn out blades<br>• Tread stripping<br>• Deformations | • Less power consumption<br>• Inadequate mixing<br>• Poor gas bubble dispersion<br>• Mass of impeller lost<br>• Poor recovery |
| **V-belt pulley** | • Improper tension<br>• Normal wear<br>• Misalignment | • Power losses<br>• Vibrations (may be transmitted to the impeller shaft) |
| **Impeller shaft** | • Mass imbalance<br>• Looseness<br>• Hydraulic forces<br>• Belt and pulley | • Vibrations<br>• Power losses<br>• Inadequate mixing performance |
| **Wall of the vessel** | • Wear by solid particle impingement | • Loss of structural integrity |

### 2.3.1 Wear

Wear can be defined as removal of material from a solid surface during the course of interaction with another surface. The methods of separation of the solid as wear debris are given below [34]:

a. Mechanical action

1. Single action: Ductile or brittle failure
2. Repeated action: High cycle (elasctic) or low cycle (plastic) fatigue

b. Chemical action

1. Loss by simple chemical dissolution
2. Removal of products formed by chemical reaction with substrate

c. Thermal action

1. Melting
2. Change in material properties to allow high wear rate.

Table 2.4 gives common types of wear and their definition by common usage in literature [34].

**Table 2.4:** Types of wear and their definition

| **Types of wear** | **Definition by common usage in literature** |
|---|---|
| **Adhesive** | Asperities of two surfaces adhere under pressure followed by shearing |
| **Diffusive** | Transfer of single atom from one body to another |
| **Abrasive** | Some combination of cutting, fatigue failure and material transfer |
| **Cutting** | Indentation by a sharp body, followed by fracture of material |
| **Deformation** | Fracture of material |
| **Fatigue** | Failure of material after cyclic straining |
| **Sliding** | Two bodies in contact erode their surfaces |
| **Cavitations** | Fatigue failure induced by collapsing bubbles in liquid |
| **Impact** | A combination of fatigue failure and loss of surface oxides |
| **Erosion** | Cutting, fatiguing and melting by impinging particles |
| **Fretting** | Fatigue failure of oxides and substrate material |
| **Scuffing** | A form of catastrophic surface failure of lubricated sliding members |
| **Chemical** | Formation of new substances that are more readily removed |
| **Corrosive** | Loss of material without formation of new substances |
| **Oxidative** | Removal of oxides formed from the surfaces |
| **Thermal** | Could cause melting or could influence chemical activity |

Of all the types of wear discussed above, erosion is most prevalent at the walls and blades of the mechanical flotation cell. Abrasion can also occur at the walls of the vessel if the entrained solids rub the walls while moving with the fluid.

## 2.3.2 Erosion

Erosion is material removal by machining action of particles entrained in high velocity fluid impinging on solid surface (Figure 2.7).

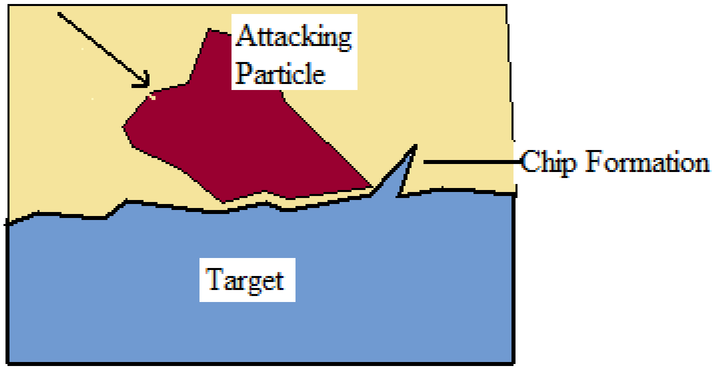


***Figure 2.7:*** *Erosion process*

While in applications such as sand-blasting, abrasive water jet machining, erosive drilling, the erosion process is helpful [35], in other processes erosion causes undesired damage, leading to degraded performance levels of the machine components and eventually failure, for example aerodynamically induced particle erosion in turbo machinery components [36], walls of pumps, pipes, chokes, valves and other fixtures used in oil and gas production industry [37] and impeller and walls of mixing vessels. Thus, in order to optimise the performance while minimising the wear damage, it is important to build a predictive model for erosion. Erosion is a combined effect of fluid-particle and particle surface interactions. Hence, the steps for building a predictive model is as follows [39,40]:

1) Determination of the fluid velocity distribution in two dimensions;

2) Evaluation of the abrasive particle impact velocity and impact angle; and

3) Application of an appropriate wear model to evaluate the mass removal

**2.3.2.1 Fluid Flow Modeling**

Early attempts to model the fluid flow was achieved by considering the flow to be a two-dimensional impinging wall jet [40,41]. The flows were considered to be two-dimensional steady potential flow (Figure 2.8). The effects of boundary layer and turbulence were neglected for the shake of simplicity. Dosanjh et.al. [39] found that relative rate of erosion decreased with the increase of flow turbulence intensity due to the enhanced axial diffusion. They suggested incorporating a two-equation (k-ε) model of turbulence to account for the turbulence. Since then, various forms of turbulence model have been included to account for turbulence for example Niu [42] used the two dimensional Reynolds-averaged Navier–Stokes equations and the kinetic energy and dissipation equations for determining the fluid flow.

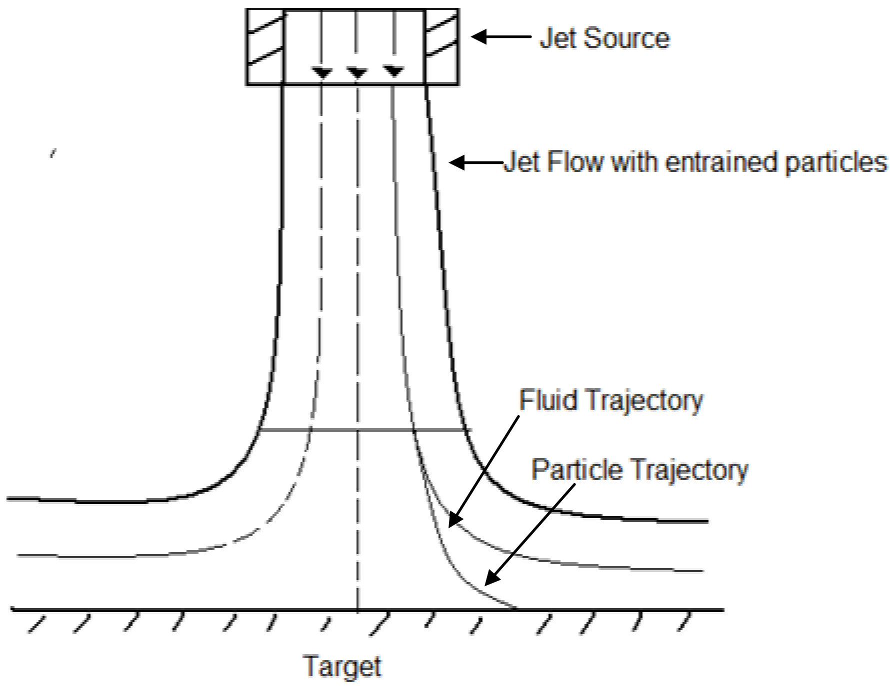


**Figure 2.8:** 2-D Impinging Wall Jet

Although numerical calculations can give fairly accurate results, they cannot be directly used in fields because its time taking and requires expert dedicated engineer. They are also expensive and can have scale-up difficulties when applied to a particular geometry. Hence, models of fluid flow that are dependent on process parameters and geometry of the unit are used to model the fluid flow in the present study. The flow modelling can be experimentally characterized by non-intrusive techniques such as laser Doppler velocimetry (LDV) and particle image velocimetry (PIV).

**2.3.2.3 Motion of particle**

Particle motion in fluid phase can described using Langrangian or Eulerian approach. In Langrangian method particle motion implies a discrete particle phase, while in Eulerian method the particle phase is treated as continuum [36]. Langrangian technique uses the force balance approach to predict the speeds and trajectories [36]. Conservation laws are used in Eulerian method to predict the field distribution of each phase [36]. The relative advantages and disadvantages of these approaches are discussed in [36]. Langrangian approach gives a better description of physical behaviour of individual particle such as velocity and trajectory in a two way coupled system. [42]. In a two-way coupling system, both the flow behaviour of the fluid and the particle motion are affected by the interaction of the particle and the fluid. If it is assumed that the motion of the dispersed particle phase is entirely dependent on the mean flow differences between the phases owing to large particle inertial momentum, it can be concluded that erosion contributed by turbulence enhanced diffusion of the particle phase is a result of turbulence enhanced diffusion of fluid phase [43-45]. In case of the mixing vessel, it follows that if the fluid flow field can be determined, the trajectories of the entrained particles can also be found. The equation of motion [36,42] for the particle is expressed as:

$$\frac{d\overrightarrow{V_p}}{dt} = g + \frac{f}{\tau}(\vec{V} - \vec{V}_p) \tag{2.29}$$

Where $\vec{V}$ and $\vec{V}_p$ are the fluid and particle velocities respectively. The empirically determined correction factor $f$ is added to make the Stokes drag formula applicable when the particle Reynolds number is of order unity or larger. The correction factor is given by Boothroyd [46] as

$$f = \begin{cases} 1+0.15\,\mathrm{Re}_p^{\ 0.687} & 0<\mathrm{Re_p} \le 200 \\ 0.914\,\mathrm{Re}_p^{\ 0.282}+0.0135\,\mathrm{Re}_p & 200<\mathrm{Re_p} \le 2500 \\ 0.0167\,\mathrm{Re}_p & \mathrm{Re_p} > 2500 \end{cases} \quad (2.30)$$

the particle response time $\tau$ is defined as :

$$\tau = d_m^{\ 2}\rho_p \big/ 18\mu \quad (2.31)$$

and

$$\mathrm{Re}_p = \left|V - V_p\right| d_m / \nu \quad (2.32)$$

where $\mu$ and $\nu$ are the dynamic and kinematic viscosity respectively. If fluid velocity components are determined, then the equation of motion as given above for a single particle can be solved using a numerical integration technique.

#### 2.3.2.3 Wear Model

With the information of particle velocity and the angle of impact, it is possible to estimate the material loss from the surface. Various models on wear have existed but models developed by Finnie and Bitter [50,51] are extensively discussed in literature. They are presented in following paragraphs, followed by the model used.

a) **Finnie's wear model**: Finnie [47,48,49] was one of the earliest researchers to propose a predictive model of erosion. He suggested that modeling wear involves determining the following:

1) Fluid flow conditions with the number, direction and velocity of particles impinging the surface.
2) The amount of material removed.

Finnie classified the target materials in two categories: a) ductile and brittle materials. In ductile materials, material was removed by plastic deformation caused by cutting action of the striking particle. Material was lost by brittle fracture in brittle materials. Stokes drag formula was used to determine the motion of the particle in the fluid and finally to come up with an expression for the mass of material removed ($Q$) by a single particle of mass $m$, velocity $v$ by assuming that the volume removed is equal to the volume of the particle beneath the surface of the plastic target:

$$Q = \frac{mv^2}{p\psi k} f(\alpha) \tag{2.33}$$

where $f(\alpha)$ is the function of impact angle , $\psi$ is the ratio of depth of cut, $p$ is the constant plastic flow stress, and $k$ is the ratio of vertical to horizontal force component on particle. The conclusion was that the severity of erosion depends on the impact angle, the velocity and the nature of the abrasive particle and the target.

b) **Bitter wear model:** J. Bitter_[50,51] proposed a model by proposing that erosion occurs because of the following two simultaneous processes:

1) Deformation wear: caused by repeated impingement of the abrasive particles on the surface at high impact angles, eventually leading to fragmentation of the surface.
2) Cutting wear: caused by the scratching action of the particles at low angles of impact.

He decomposed the impact velocity into two components: one parallel to the surface and other normal to the surface. He noted that while the normal component was responsible for deformation wear, the parallel component caused the scratching. He also found that as long as the normal component of velocity is not greater than the velocity required for a plastic collision, the parallel component would not contribute to erosion. The energy required for material removal was provided by the kinetic energy of the particles. Depending on whether the particles had some horizontal component velocity leftover and using the force balance equations, the material removed was calculated as:

$$Q = \begin{cases} Q_d + Q_{c_1} & \alpha \le \alpha_0 \\ Q_d + Q_{c_2} & \alpha \ge \alpha_0 \end{cases} \tag{2.34}$$

$$Q_d = \frac{1}{2}\frac{m(v\sin\alpha - K)^2}{\varepsilon} \tag{2.35}$$

$$Q_{c_1} = \frac{2mC(v\sin\alpha - K)^2}{(v\sin\alpha)^{0.5}}\left(v\cos\alpha - \frac{C(v\sin\alpha - K)^2}{(v\sin\alpha)^{0.5}}\rho\right) \tag{2.36}$$

$$Q_{c_2} = \frac{1}{2}\frac{m[(v\cos\alpha)^2 - K_1(v\sin\alpha - K)^{3/2}}{\rho} \tag{2.37}$$

where $K$ is the maximum normal component of velocity for which the collision is purely elastic, $K_1$ and $C$ are proportionality constants, $\varepsilon$ is the amount of energy required to remove a unit mass from the target by means of deformation, $\rho$ is the amount of energy required to remove a unit mass from the target by means of scratching, and $\alpha_0$ is the impact angle at which the horizontal component of velocity just becomes zero after leaving the target.

#### 2.3.2.4 Model Selection Options

The model proposed by Oka *et al.* [52,53] has a number of advantages. The model can be used under any impact conditions; it is applicable for any type of material; the model includes the main impact parameters (impact velocity, angle and particle size and property) as well as material hardness; and the model is applicable in cases where the particle velocity is very small compared to the fluid velocity and when the average size of the particles is small.

The erosion rate from particles impinging normal to the surface is termed $E(90)$ (volume/mass), expressed by

$$E(90) = K(Hv)^{k_1}\left(\frac{V_p}{V'}\right)^{k_2}\left(\frac{D_p}{D'}\right)^{k_3} \tag{2.38}$$

$$n_1 = s_1(Hv)^{q_1}, n_2 = s_2(Hv)^{q_2}, k_2 = 2.3(Hv)^{0.038} \tag{2.39}$$

where $Hv$ is the wall hardness (GPa), $V_p$ and $V'$ are impact speed and reference impact speed, and $D_p$ and $D'$ are average particle diameter and reference diameter. For sand particles; $s_1$=0.71, $s_2$=2.4, $q_1$=0.14, $q_2$=-0.94, $k_1$= -0.12, $k_3$=0.19, $V'$=104 m/s, $K$=64, & $D'$= 326 microns. The impact angle dependence of erosion is incorporated in the term $g(\theta)$, where $g(\theta)$ is the ratio of erosion rate $E(\theta)$ at an arbitrary angle $\theta$ with respect to damage at 90 degrees $E$(90), such that

$$E(\theta) = g(\theta)E(90) \tag{2.40}$$

$$g(\theta) = (\sin\theta)^{n_1}(1 + (\mathrm{Hv})(1 - \sin\theta))^{n_2} \tag{2.41}$$

The first term in $g(\theta)$ denotes the deformation wear; and the second term incorporates the effect of cutting action, accounting for the effect of material properties by adding the material hardness number Hv. Parameters considered for the carrier fluid, particle and the surface in literature are given in table 2.5 [36].

**Table 2.5:** Parameters considered in erosion models

| *For particles* | *For surfaces* | *For carrier fluid* |
|---|---|---|
| 1) Impact and rebound angles<br>2) Impact and rebound speed<br>3) Rotation of the particle<br>4) Shape and size<br>5) Volume concentration and surface flux<br>6) Physical properties (hardness, strength and density)<br>7) Fragmentation<br>8) Interactions( with surfaces, fluid or other particles) | 1) Physical properties<br>2) Change in shape caused by erosion<br>3) Stress level<br>4) Temperature<br>5) Presence of oxides or coatings<br>6) Simultaneous occurrence of corrosion | 1) State of motion( level of turbulence)<br>2) Velocity<br>3) Temperature<br>4) Chemical composition and physical properties |

## 2.4 Knowledge Gaps and Proposed Approach

The erosion models developed have not significantly delved into the near wall effects such as the energy interactions near the wall and reduction in velocity due to the presence of thin film just in front of the wall. These models work in isolation and are not well connected to the overall process and hence cannot be directly used in the industry. Apart from the three step modeling (fluid flow, solid motion and wear) of erosion, the above three factors: 1) energy interactions at the wall, 2) reduction in velocity just before impact, and 3) connecting the model to process parameters and predicting the damage accumulated over time, were the specific contributions of the study in modeling wear in a particular geometry. Each of these topics is briefly explained below.

### 2.4.1 Energy lost during impact process

The application of classical theory of impulse and momentum in the field of wear has not always been favourably viewed because the following contentions [54]:

1) Impulse and momentum theory only provides information of velocity changes and employs coefficient of restitution to model the specific conditions of impact. Thus, it does not provide an explanation for interacting forces and deflections.
2) The results when the impulse and momentum theory is applied to wear dynamics is often counter-intuitive or does not seem fit the experimental data.

The counter argument to the first point is provided by the Brach [54] who contests that the knowledge of velocity changes provides the foundation for calculating the energy losses. Energy losses in turn are proportional to volume and mass losses in wear and erosion processes. He attacks the second contention by attributing the lack of complete understanding of the theory applied to wear process. He suggested that the amount of material removed in wear process can be estimated by dividing the kinetic energy lost in the impact event divided by the energy required for unit mass removal. He gave an expression for the energy absorbed in shear during the impact process as:

$$T = \left[ \{1/(1+\lambda)\}(\mu/\mu_c)(2-\mu/\mu_c)\cos^2\alpha \right] \frac{1}{2} mV^2 \qquad (42)$$

where $\lambda = r^2/k^2$, $r$ being the distance between the centre of mass and the point of contact between the particle and eroding surface, and $k$ the radius of gyration, and $\alpha$ is the impact angle and for angular particles, it is reasonable to assume that the value of $\lambda$ is 3 [54]. Coefficient of restitution $e$ is the ratio of normal rebound velocity to normal incident velocity. $\mu$ represents the friction coefficient and $\mu_c$ represents the maximum coefficient of friction such that for $\mu < \mu_c$ sliding exists between the particle and the surface, whereas at $\mu = \mu_c$ sliding ends and the particle starts to roll over the surface. $e$, $\mu$, and $\mu_c$ can be determined analytically by models of stresses and deformations.

## 2.4.2 Velocity reduction due to thin film

Little literature is available on the interaction of solid particles with the fluids near the impact point. Experimental results are generally used to deduce the velocity of the particle before impact, for instance impact velocity can be derived form the size of the craters [55]. These results have shown that impact velocities of suspended particles are much less than nominal speed of the erosion test specimen. For some cases the impact velocities were as low as 10% of the nominal test speed [55].

Clark *et al.* [55] and Wong *et al.* [56] noticed that if a particle advancing towards the surface has to impinge, it has to displace the film of liquid between the particle and the surface (Figure 2.9). The pressure required to exude the fluid film can significantly reduce the impact velocity below the predicted values. This pressure provides the cushioning effect which determines the velocity of the particle just before the impact.

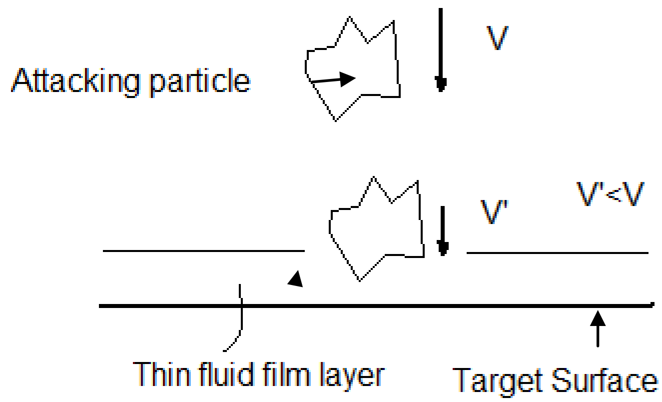


***Figure 2.19****: Velocity reduction due to thin film*

They proposed a correction factor to adjust the normal component of velocity just before impact:

$$V' = FV \tag{2.43}$$

$$F = \frac{a}{a+\xi} - \frac{12\xi^2}{a+\xi}\frac{1}{\mathrm{Re}_p^*} \tag{2.44}$$

where:

$$\mathrm{Re}_p^* = \frac{\rho V d_p}{\mu} \tag{2.45}$$

$$a = 8\left(\frac{2\rho_s}{\rho} + f_{av}\right) \tag{2.46}$$

$$f_{av} \cong 1 \tag{2.47}$$

$$\xi \approx 10 \tag{2.48}$$

where $V$ and $V'$ are the incident normal velocity before and after entering the thin film respectively, $d_p$ is the diameter of the particle, $\rho$ is the density and μ is the viscosity of the fluid.

## 2.4.3 Damage Model

Damage depends on the dissipation of energy at the component being damaged. The energy contributing towards the damage comes from process system [57]. The energy dissipated at the element getting damaged transforms to a form that results in damage accumulation [57]. If $D$ be the damage accumulation then, $D$ is a function of local damage variables which in turn is relate to process variables through some function.

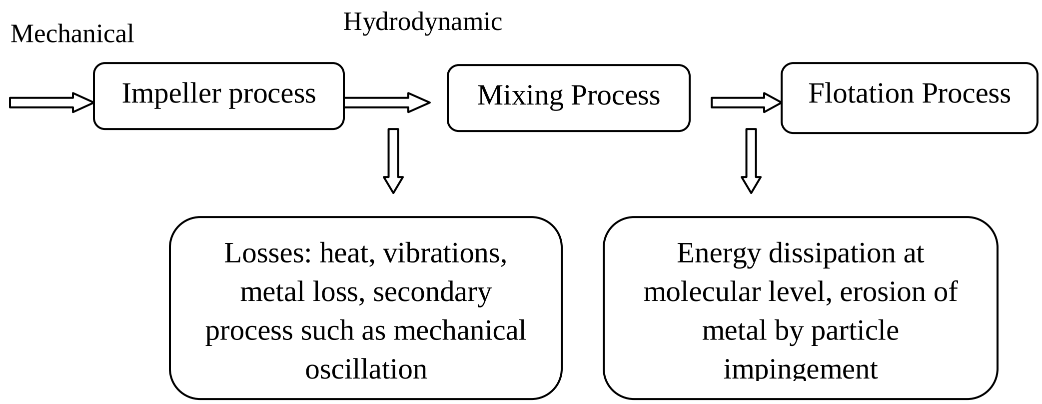


***Figure 2.10:*** *Energy transformation in Flotation Units*

In case of mixing vessel, the energy input to a mixing vessel is provided as mechanical energy of the rotating impeller. This is then transformed into the turbulent kinetic energy of the working fluid and kinetic energy of the solid particles (figure 2.10). Most of the turbulent kinetic energy of fluid is dissipated in impeller stream, bulk flow and near the walls of the vessel. A part of the kinetic energy of the particles is lost upon impingement on the walls of the vessel and the impeller while the rest of the energy can be natural dissipation of energy. This energy lost can contribute to the damage of the walls. The energy conversion process can be represented by the following Figure 2.10.

Damage, $D$ in this case can be volume of material removed, and the local damage variables can be fluid, velocity, particle velocity, solids concentration and material properties of the solids and the target. Of these variables, fluid velocity and particle velocity are related to the process through the impeller speed, power consumption etc. If $W$ is the energy lost per unit time by the impinging particles during the impact process, then the damage rate $\dot{D}$ is given by:

$$\dot{D} = \alpha W \tag{2.49}$$

where $\alpha$ is a constant that depends upon the damage mechanism and the particle-surface properties . For example, $\alpha$ can be a function of energy required to remove unit volume of material from the surface by mechanisms such as cutting or deformation. The total damage accumulation over a period of time t is given by:

$$D = \int_0^t \dot{D} dt = \int_0^t \alpha W dt \tag{2.50}$$

If the cumulative damage exceeds a specified limit, the component needs to maintenance.

### 2.4.4 Solution Approach

The background theory discussed so far in the chapter was helpful in devising solution approach to meet the two-fold objectives of the study. The knowledge of fluid flow in mixing vessel helped in determining the motion of abrasives in the tank. The literature on erosion helps in understanding the concept and enabled to select a suitable model for the mixing vessel. The near wall energy interactions and reduction in the velocity before the walls helps to analyse the particle-surface interactions. Linking the erosive damage accumulation to the process is useful in damage prevention by tuning the process parameters. The damage model can be utilized to estimate the time-to-failure of the component. Figure 2.11 recapitulates the methodology.

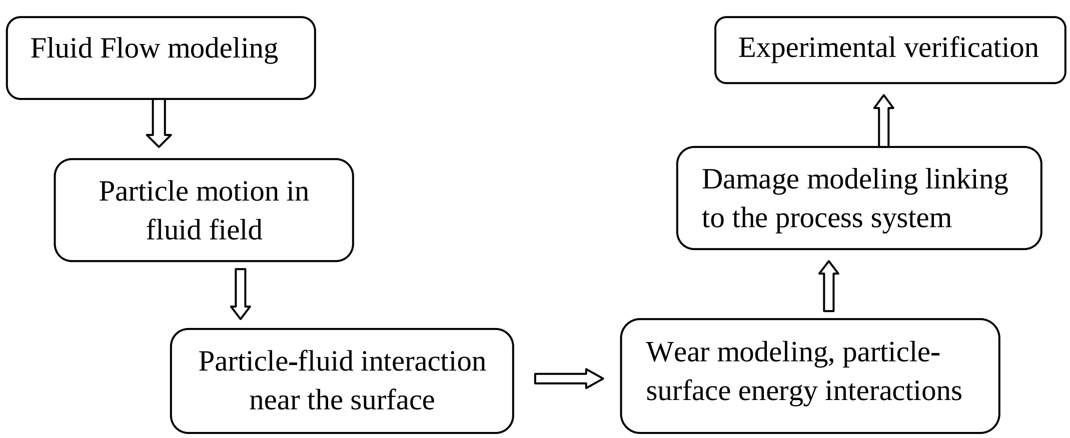


***Figure 2.11**: Outline of wear modeling*

Understanding of the flotation process was necessary to understand how different sub-processes interact with each other. Ore composition such as valuable mineral and undesirable solids reporting to the top as the response to the process conditions can be used for feed-back control of the process.

# References:

[1] King R. Peter [2001] “Modeling and simulation of mineral processing systems”, Butterworth-Heinemann publishing, **ISBN-10 / ASIN:** 0750648848, pp 289-311.

[2] Gupta A., Yan D [2006], “Mineral processing design and operation: An introduction”, Elsevier Science publishers, **ISBN / ASIN:** 0444516360, pp 557-586

[3] Kasongo T, Zhou Z, Xu Z, Masliyah J. Effect of clays and calcium ions on bitumen extraction from athabasca oil sands using flotation. Can J Chem Eng. 2000;78(4):674-81.

[4] Zhou Z, Kasongo T, Xu Z, Masliyah J. Assessment of bitumen recovery from the athabasca oil sands using a laboratory denver flotation cell. Can J Chem Eng. 2004;82(4):696-703

[5] Xu M, Quinn P, Stratton-Crawley R. A feed-line aerated flotation column part 2: Modelling and scale-up. Minerals Eng. 1996;9(6):655-66.

[6] Sanford EC, Seyer FA. Processibility of Athabasca tar sand sand using a batch extraction unit: the role of NaOH CIM Bull. 1979;72(803):164-9.

[7] Department of Chemical Engineering, University of Alberta

[8] Bulmer, J.T. and J. Starr, “Syncrude Analytical Methods for Oil Sand and Bitumen Processing” AOSTRA technical publication series #1, Alberta Oil Sands Technology and Research Authority, Edmonton, AB (1979).

[9] Bartolacci G, Pelletier Jr. P, Tessier Jr. J, Duchesne C, Bossé P-, Fournier J. Application of numerical image analysis to process diagnosis and physical parameter measurement in mineral processes-part I: Flotation control based on froth textural characteristics. Minerals Eng. 2006;19(6-8):734-47.

[10] Wang W, Bergholm F, Yang B. Froth delineation based on image classification. Minerals Eng. 2003;16(11):1183-92.

[11] Liu JJ, MacGregor JF. Froth-based modeling and control of flotation processes. Minerals Eng. 2008;21(9):642-51.

[12] Haavisto, O. (2009). „Reflectance spectrum analysis of mineral flotation froths and slurries‟, dissertation from Helsinki University of Technology, Department of Automation and Systems Technology

[13] Wills, B.A., 1984. Automatic control of flotation. Engineering and Mining Journal (June), 62–66.

[14] McKee, D.J., 1991. Automatic flotation control – a review of 20 years of effort. Minerals Engineering 4, 653–666.

[15] Braden, T. F., Kongas, M., and Saloheimo, K. (2002). On-line composition analysis of mineral slurries. In Mular, A. L., Halbe, D., and Barrett, D. J., editors, *Mineral Processing Plant Design, Practice and Control*, pages 2020–2047. SME, Littleton, Colorado.

[16] Moolman, D.W., Aldrich, C., Van Deventer, J.S.J., Bradshaw, D.J., 1995. Interpretation of flotation froth surfaces by using digital image analysis and neural networks. Chemical Engineering Science 50, 3501–3513.

[17] Moolman, D.W., Eksteen, J.J., Aldrich, C., Van Deventer, J.S.J., 1996. The significance of flotation froth appearance for machine vision control. International Journal of Mineral Processing 48, 135–158.

[18] Liu, J., MacGregor, J.F., Duchesne, C., Bartolacci, G., 2005. Monitoring of flotation processes using multi resolutional multivariate image analysis. Minerals Engineering 18 (1), 65–76.

[19] Symonds, P. J. and De Jager, G. (1992). A technique for automatically segmenting images of the surface froth structures that are prevalent in industrial flotation cells. In *Proc. of the 1992 South African Symposium on Communications*

*and Signal Processing*, pages 111–115, University of Cape Town, Rondebosch, South Africa.

[20] Bonifazi, G., Serranti, S., Volpe, F., and Zuco, R. (1998). Flotation froth characterisation by optical-digital sectioning techniques. In *Proc. Int. Conf. on Quality Control by Artificial Vision*, Takamatsu, Kagawa, Japan.

[21] Cipriano, A., Guarini, M., Vidal, R., Soto, A., Sepulveda, C., Mery, D., and Briseno, H. (1998). A real time visual sensor for supervision of flotation cells. *Miner. Eng.*, 11(6):489–499.

[22]Moolman, D. W., Aldrich, C., and Van Deventer, J. S. J. (1994). Digital image processing as a tool for on-line monitoring of froth in flotation plants. *Miner. Eng.*, 7(9):1149–1164.

[23] Gebhardt, J. E., Tolley, W. K., and Ahn, J. H. (1993). Color measurements of minerals and mineralized froths. *Min. & Metall. Process.*, 10(2):96–99.

[24] Hargrave, J. M., Miles, N. J., and Hall, S. T. (1996). The use of grey level measurement in predicting coal flotation performance. *Miner. Eng.*, 9(6):667–674.

[25] Lyder, D., Feng, J., Rivard, B., Gallie, A., & Cloutis, E. (2010). Remote bitumen content estimation of athabasca oil sand from hyperspectral infrared reflectance spectra using Gaussian singlets and derivative of Gaussian wavelets. *Fuel*, *89*(3), 760-767.

[26] Rivard, B. Feng, J. , Lyder, D., Gallie, A., and Cloutis, E. 2007a. “Rapid characterization of oil sand properties using near infrared and thermal infrared reflectance spectroscopy.” 57th Canadian Chemical Engineering Conf. Sept. 2007.

[27] Rivard, B, Lyder, D, Feng, J., Gallie, A., and Cloutis, E. 2007b. “Determining bitumen content from reflectance spectra of oil sands using wavelet, singlet, and broad band analysis.” 9th Geoide annual conference. Halifax, NS, June 6-8.

[28]Rogge, D., and Rivard, B. 2008. “Applications of imaging spectroscopy to the characterization of rock and oil sand core.” Proc. CIM Conf Edmonton, May 4-7 2008, session exploration and innovation 2.

[29] Paul, Edward L., Atiemo-Obeng, Victor A., Kresta, Suzanne M., “Handbook of industrial mixing”, oboken, N.J. : Wiley-Interscience, c2004.

[30] www.mixmor.com (date accessed 14th Jan 2011)

[31] B. Platzer and G. Noll, Modelling of the local distributions of velocity components and turbulence parameters in agitated vessels – Method and results, *Chem. Eng. Process.* 23 (1988), pp. 13–31

[32] DeSouza, A., and R. W., Pike, “ Fluid Dynamics and Flow Patterns in Stirred Tanks with a Turbine Impeller,” *Can. J. Chem. Eng.* , **50** (1972)

[33] http://en.wikipedia.org/wiki/Basset_force (date accessed 2011-01-23)

[34] H.C. Meng and K.C. Ludema, Wear models and predictive equations: their form and content, *Wear* **181–183** (1995), pp. 443–457.

[35] I. Finnie, Erosion of surfaces by solid particles. *Wear* **3** (1960), p. 87.

[36] J.A.C. Humphrey, ‘Fundamentals of fluid motion in erosion by solid particle impact’, Int. J. Heat Fluid Flow, 2, 120-195 (1990)

[37] Y. Zhang, E. P. Reuterfors, B. S. McLaury, S. A. Shirazi and E. F. Rybicki, Comparison of Computed and Measured Particle Velocities and Erosion in Water and Air Flows [J], Wear, 2007, 263: 330–338.

[38] http://www.stle.org/resources/lubelearn/wear/default.aspx (Date accessed Jan 21, 2011)

[39] Dosanjh S, Humphrey JAC. The influence of turbulence on erosion by a particle-laden fluid jet. Wear. 1985;102(4):309-30.

[40] Benchaita MT, Griffith P, Rabinowicz E., Erosion of metallic plate by solid particles entrained in a liquid jet. Journal of engineering for industry. 1983;104(3):215-22

[41] Benchaita, M. T., "Erosion of Metal Pipe by Solid Particles Entrained in a Liquid," Ph.D thesis in Mechanical Engineering, Massachusetts Institute of Technology, Cambridge, Mass., Feb. 1980, pp. 87-98.

[42] Niu Y-. Evaluation of erosion in a two-way coupled fluid-particle system. Int J Numer Methods Fluids. 2001;36(6):711-42.

[43] Naik S, Bryden IG. Prediction of turbulent gas–solid flow in curved ducts using the Eulerian–Lagrangian method. *International Journal for Numerical Methods in Fluids* 1999; **31**: 579–600.

[44] Fan J, Zhou D, Zeng K, Cen K. Numerical and experimental study of finned tube erosion protection methods. *Wear* 1991; **142**: 171–184.

[45] Fan J, Zhou D, Jung J, Cen K. Numerical simulation of tube erosion by particle impaction. *Wear* 1992; **152**:1–19.

[46] R.G. Boothroyd, Flowing Gas-Solids Suspensions, Chapman and Hall, London, 1971

[47] Finnie I., Erosion of surfaces by solid particles. *Wear* **3** (1960), p. 87.

[48] Finnie I., Some observations on the erosion of ductile metals. *Wear* **19** (1972), p. 81.

[49] I. Finnie and D.H. McFadden, On the velocity dependence of the erosion of ductile metals by solid particles at low angles of incidence. *Wear* **48** (1978), p. 181.

[50] Bitter J.P.A., A study of erosion phenomena part I. *Wear* **6** (1963), p. 5.

[51] Bitter J.P.A., A study of erosion phenomena part II. *Wear* **6** (1963), p. 169.

[52] Y.I. Oka, K. Okamura and T. Yoshida, Practical estimation of erosion damage caused by solid particle impact. Part 1: effects of impact parameters on a predictive equation, *Wear* **259** (2005), pp. 95–101.

[53] Y.I. Oka and T. Yoshida, Practical estimation of erosion damage caused by solid particle impact. Part 2. Mechanical properties of material directly associated with erosion damage, *Wear* **259** (2005), pp. 102–109.

[54] R.M. Brach, Impact dynamics with applications to solid particle erosion. International Journal of Impact Engineering 7 (1988), pp. 37–53.

[55] Clark HM, Burmeister LC. The influence of the squeeze film on particle impact velocities in erosion. Int J Impact Eng. 1992;12(3):415-26.

[56] Wong KK, Clark HM. A model of particle velocities and trajectories in a slurry pot erosion tester. Wear. 1993;160(1):95-104

[57] MG Lipsett. Incorporating Damage Models in Deterministic System Models to Model Reliability in Time-Varying Systems. Proc British Inst. of Non-Destructive Testing Conf. on Condition Monitoring (CM2009), Dublin June 23, 2009.

[57] http://www.albertatechfutures.ca/default.aspx (date accessed 16/03/2011)

**Chapter 3**

# Processability and Hyperspectral Analysis

The separability of bitumen from oilsand depends on a number of factors. Some of these factors are observable in the ore using reflectance spectrometry in the infrared range. The present work investigated whether hyperspectral features relate to the ore processibility. A set of processability tests was conducted using a Denver cell and a standard set of operating conditions; and hyperspectral measurements were made of ore samples, homogenized samples, supernatant froth, and solids.

## 3.1 Introduction and Motivation

Naturally occurring oilsand is a mixture of bitumen, water, clay minerals and quartz grains. Bitumen recovery performance depends on the bitumen content, the type and amount of clays present, the degree of weathering of the oil sand sample before processing, and the process conditions for a given process configuration [1,2]. Controllability of a process is limited when variables that affect process performance are not observable.

Currently, open-loop process control is used both for oilsand slurry preparation and bitumen separation from slurry using the Clark Hot Water Extraction process. Based on the orebody delineation and the location of mining shovels, estimates of the grade and fines content of the ore blend that is projected to enter the process may be used to adjust setpoints for water addition rate and addition of process additives such as sodium hydroxide. Since oilsands orebodies are not homogenous and can exhibit considerable variability in the composition of feed to the extraction process, it would be advantageous to adjust the setpoints based on the actual grades and fines content instead of their estimates.

There is no current method for extracting mineral features of oilsands ore in real time, and yet there are ongoing changes in feedstock to the extraction process. Hence, there is a need to be able to measure real-time and on-line processibility features that can be used monitor and control separation processes for improved recovery and froth quality. Extending the method of measuring reflectance spectral features to look for hyperspectral features in ore and process streams that may relate to oilsands processability is the goal of the present work.

### 3.1.1 Methodology and Technology

Hyperspectral imaging collects and processes information within a specified spectral range [3]. Materials have a unique spectral signature, which can be used for their identification in the target being scanned, although reflectance spectra may be affected by illumination effects [3]. Some of the spectral ranges useful for determining the composition of oil sands are: visible to near infrared (0.5-2.5μm); mid infra-red (3-14μm); and thermal infrared (3-30μm). Infrared reflectance spectroscopy has been used in a variety of investigations such as studies on the the mineralogy of oil sands, bitumen characteristics, and bitumen content in samples of oilsands ore [4]. In this study an analytical spectral devices (ASD) spectrometers was used to collect spectra from oil sands for the visible to near infrared range, and a Bomen FTIR spectrometer was used to collect spectra in the mid-infrared range [5]. The present investigation looked for relationships between reflectance hyperspectral features and total bitumen content and fines content in a range of oilsands ore samples. The study also examined spectral features in the froth produced during batch extraction tests under standard conditions. Hyperspectral features of the ore and features observed as the froth were produced were also compared to qualitative observable features, such as colour of the froth and the apparent recovery based on how clean the coarse sand fraction appeared in samples collected in the jars.

## 3.2 Experimental Plan

Experiments were designed to compare hyperspectral data collected during batch extractions for ore exhibiting poor recovery and samples with good recovery. To this end, hyperspectral images were taken on the froth at two stages: during the batch extraction, with spectra taken from the surface of the froth layer while the froth was in the separation cell, and after froth sample collection.

Flotation experiments were conducted to rate the relative separation performance of ten different oil sands received from Syncrude Canada Limited.  Besides the quantitative analysis of the froth in terms of bitumen, solids and water content qualitative analysis of the froth was done to analyse the observed variables.

### 3.2.1. Preparation

Samples were received from Syncrude in 20 litre pails. Descriptions of the samples are given in Table 3.1 (next page), with related estimates of bitumen content, water content, total solids content, and fines content (less than 44 µm).

Part of each sample was kept in reserve as received, that is, each of the ten samples was separated, with part of each sample remaining frozen in storage in sealed containers. Each working sample was then mixed and homogenized using a comil.

***Table 3.1:*** *Indexing and description of samples*

| Sample number | Description | Facies | Fines (<44µm) | Oil | Water | Solids |
|---|---|---|---|---|---|---|
| **1** | Average | 15 | 31 | 8.23 | 5.39 | 86.05 |
| **2** | RAS11054 (marine) | 96 | 11.13 | 13.85 | 2.58 | 83.27 |

| | | | | | | |
|---|---|---|---|---|---|---|
| **3** | High grade - med fines Marine (bedded) | 95 | 27.3 | 12.35 | 4.63 | 83.02 |
| | | 95 | | 11.99 | 3.65 | 84.36 |
| | | 95 | | 11.71 | 5.11 | 83.18 |
| **4** | Low grade - high fines Estuarine (bedded) | 8 | 40.06 | 6.02 | 7.54 | 86.44 |
| | | 7 | | 6.98 | 6.28 | 86.74 |
| | | 7M<br>7 | | 9.2 | 6.33 | 84.47 |
| **5** | Med grade - high fines Marine (bedded) | 96 | 40.75 | 9.61 | 7.44 | 82.95 |
| | | 96 | | 9.89 | 6.23 | 83.88 |
| **6** | Average | 8 & 9 | 46.24 | 6.97 | 3.53 | 89.21 |
| **7** | High grade - low fines Marine | 26 | 6.71 | 10.99 | 2.86 | 86.15 |
| | | 26 | | 11.99 | 3.18 | 84.83 |
| | | 26 | | 12.85 | 4.03 | 83.12 |
| **8** | Low grade - med fines Fluvial (burrowed) | 72 | 24.98 | 8.7 | 7.95 | 83.35 |
| | | 79 | | 6.98 | 10.12 | 82.9 |
| | | 72 | | 3.2 | 7.15 | 89.66 |
| | | 41 | | 12.33 | 5.9 | 81.77 |
| **9** | High grade - low fines Estuarine | 11 | 13.83 | 14.4 | 4.37 | 81.23 |
| | | 11 | | 14.13 | 3.14 | 82.73 |
| | | 11 | | 13.92 | 3.25 | 82.83 |
| **10** | RAS11055 (Marine) | 26 | 2.44 | 13.66 | 3.12 | 83.16 |

A comil is a rotary breaker, which breaks the bigger chunks of oil sands. A comil is shown in the photo of Figure 3.1. The crushed samples were manually homogenized, but not blended with other samples. From each of the 10 homogenized samples, 4 subsamples each of 300 grams were formed to conduct separation tests

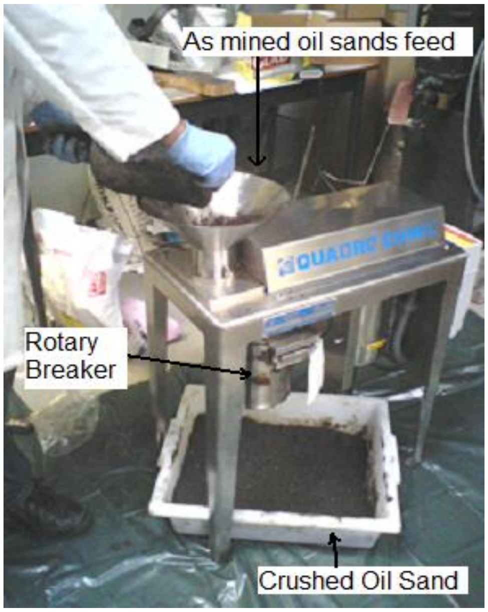


***Figure 3.1:*** *Comil used for homogenising*

***Figure 3.2****: Flotation cell*

### 3.2.2 Design & set-up

A 2 litre laboratory-scale Metso Denver flotation cell was used for the experiment. A metal jacket was fabricated around the cell to allow the circulation of heated water in the jacket. The temperature of the slurry inside the vessel was controlled by regulating the temperature of the water circulating in the jacket. A thermometer was used to check the temperature of the slurry. Compressed air was introduced into the slurry and the air flow was controlled by air flow meter. Figure 3.2 shows the flotation vessel and Figure 3.3 shows the set-up of air-flow meter and the temperature controller (attachments). The detailed list of parts required for the assembly of flotation unit is given in Appendix A-2.

### 3.2.3 Experimental Conditions

The protocol established by the Department of Chemical Engineering, University of Alberta has been used for the experiments [6]. The Table 3.2 gives the list of parameters and their ranges. Details of the procedure can be found in Appendix A-1.

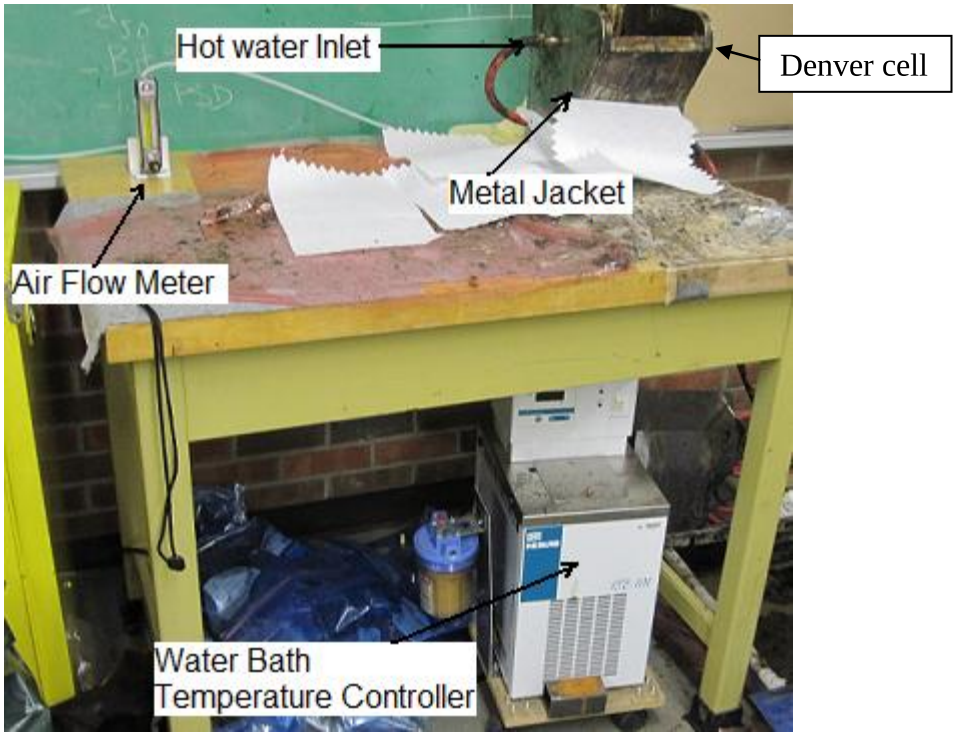


***Figure 3.3:*** *Attachments to flotation cell*

**Table 3.2:** Parameters and ranges

| **Manipulated Variables** | **Ranges** |
|---|---|
| Oil sands to water ratio | 300 g of oil sands in 950 ml of tap |
| Impeller speed | 1200,1500 and 1800 rpm |
| Aeration rate | 100,150 and 200 ml/min |
| Temperature | 45 degree Celsius |
| Ore type | 10 different types |

The only manipulated variables were the impeller speed and aeration speed. Using factorial design of experiments, an experimental matrix was generated for testing each of the 10 oil sands type. Table 3.3 shows the four different operating conditions. The four sub-samples were run at each of these four conditions. Observed variables are the variables that can be physically observed or measured. Table 3.4 gives the list of observed variables for the experiment.

***Table 3.3:*** *Experimental Matrix*

| **Trial for an oil sand type** | **Impeller speed (rpm)** | **Aeration rate (ml/min)** |
|---|---|---|
| **Operating condition 1** | 1200 | 100 |
| **Operating condition 2** | 1200 | 200 |
| **Operating condition 3** | 1800 | 100 |
| **Operating condition 4** | 1800 | 200 |

***Table 3.4:*** *Observed variables*

| **Observed variable type** | **Observed variable** |
|---|---|
| Quantitatively Measured | Percentage composition of bitumen, water, and solids |
| Qualitatively Measured | Froth quality, Froth colour, Quality of froth |

### 3.2.4 Procedure

According to the batch extraction test protocol, the run time for each experiment was fifteen minutes. The first five minutes was the conditioning stage, during which the homogenized oil sands sub-sample (300g) mixed in 950 ml of untreated Edmonton city tap water was aerated and agitated. During the next ten minutes, the froth was collected using a spatula and stored in glass jars for Dean Stark analysis, a standard test which gives the mass of bitumen, solids, and water in the froth. Images using a standard camera and hyperspectral images were taken of the froth collected during the processes and of the froth collected and allowed to settle. The froth was collected in shallow glass jars of 6 cm diameter and 2 cm depth. Visible near infra-red (VNIR) spectral reflectance measurements were taken using an Analytical Spectral Devices (ASD) Inc. FieldSpec FR portable spectroradiometer (Analytical Spectral Devices 2003), using a tungsten-halogen, 50 W, light source with a regulated DC power supply [5]. For reflectance spectra it is important to have good illumination across the light spectrum of interest. The light source was at 30 degrees incident angle and the sensor (fibre optic) was at zero degree emission angles. Three spectra were collected for each froth sample and the three spectra were averaged. The set up for the ASD is shown in Figure 3.4(a) and Figure 3.4(b) shows the ASD taking images of the froth in the glass jar. A Bomem MB102 Fourier Transform InfraRed (FTIR) spectrometer equipped with a Hg/Cd/Te (MCT) detector was used to take thermal infrared measurements [5] as shown in Figures 3.4(c) and 3.4(d).

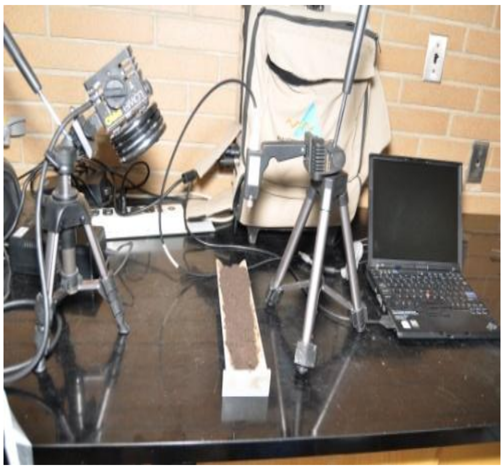

***Figure 3.4(a)****: ASD set-up*

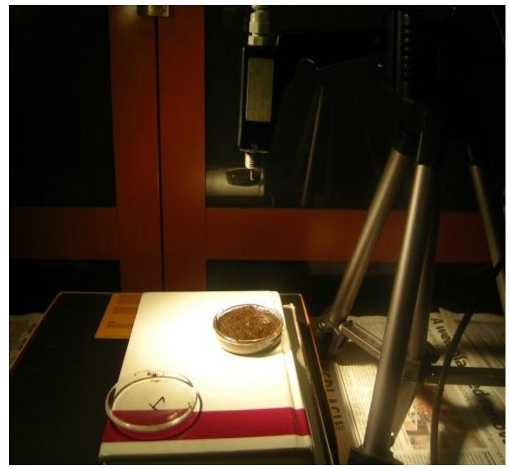

***Figure 3.4(b)****: ASD taking images*

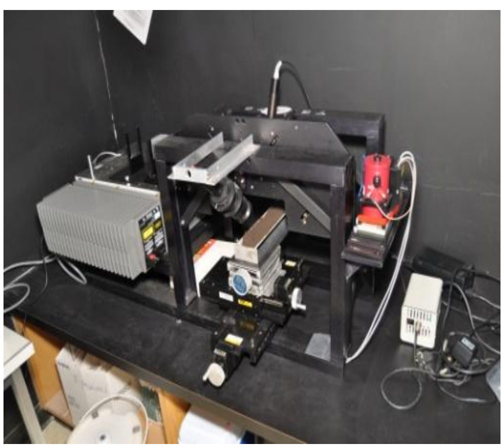

***Figure 3.4(c)****: TFIR set-up*

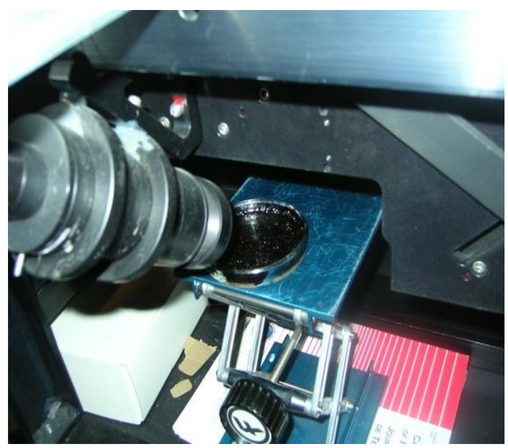

***Figure 3.4(d)****: TFIR taking images*

The reflectance spectra were taken from the ratio of each measurement to that of an illuminated 99% reflectance panel taken with the same geometry [8]. The field of view for the homogenised oil sand ore was a circle of diameter 20 mm while that for the froth was a circle with a diameter 15mm, [8]. The final spectrum of each sample and froth was obtained by averaging six spectra in the case of ore and three measured spectra from the froth [8]. Each of the spectra was obtained at a different location.

## 3.3 Results

Based on the appearance of the froth the qualitative observations were made and analysed. Standard Dean Stark analysis was conducted (by Maxxam Analytics Inc.) to estimate the amount of bitumen, water and solids in the ore and the froth for quantitative results. Hyperspectral images were analysed to extract features that would help to classify the samples based on color. These three types of analysis are presented in the following sections.

### 3.3.1 Qualitative Analysis

A preliminary qualitative assessment was made of the separation performance of different oil sands based on visual observations of the froth during the experiment and after storing samples in sealed glass jars. Such a classification was necessary to support the classification based on the hyperspectral features. The classification also helped to relate the qualitative observable features to the processibility. This qualitative assessment was done for preliminary comparison, and was not intended to replace quantitative analysis.

Time taken for the bitumen to appear on the surface as well as time taken for complete removal (after 15 minutes) was noted for each run. The qualitative figure chosen for a particular oil sand type was either the average of all the subsamples or was representative of all the subsamples. Table 3.5 shows the observations made during the experiment. Table 3.6 shows the relative grading scheme that was used to rank the individual characteristics shown in Table 3.5.

***Table 3.5***: *Qualitative Observations during the process*

| Sample # | Time taken for bitumen to appear on the surface(seconds) | Time taken after the experiment run time (in seconds) | Bubble concentration | Bitumen per unit volume of froth |
|---|---|---|---|---|
| **1** | 15 | 60 | Very Good | Average |
| **2** | 10 | 5 | Good | Very Good |
| **3** | 60 | 120 | Excellent | Good |
| **4** | 60 | 130 | Very Good | Average |
| **5** | 45 | 90 | Very Good | Good |
| **6** | 30 | 180 | Average | Poor |
| **7** | 10 | 0 | Poor | Excellent |
| **8** | 30 | 30 | Good | Good |
| **9** | 20 | 5 | Very Good | Very Good |
| **10** | 10 | 0 | Poor | Excellent |

***Table 3.6:*** *Grading Scheme*

| **Grades** | Excellent | Very Good | Good | Average | Poor |
|---|---|---|---|---|---|
| **Definition** | The best in all samples | Next to “Excellent” & better than the rest | Next to “Very Good” | Next to “Good” | The worst amongst all |

The parameters chosen for rating the performance during the experiments were bubble concentration and the apparent concentration of bitumen in the froth. Bubble concentration is related to the response of the oil sand to the presence of bubbles of an appropriate size and the presence of natural frothing agents in the oil sand. A good bubble concentration in froth indicates good separation performance, and it would also loosely relate to the volume of bitumen recovered. Bitumen per unit volume of froth is the measure of the concentration of bitumen (volume percent) in the froth; and this may be subject to interpretation as froth can deaerate over time. For this reason, froth was allowed to settle before making an assessment.

Figure 3.5 shows photographs typical of the froth removed during the experiments.

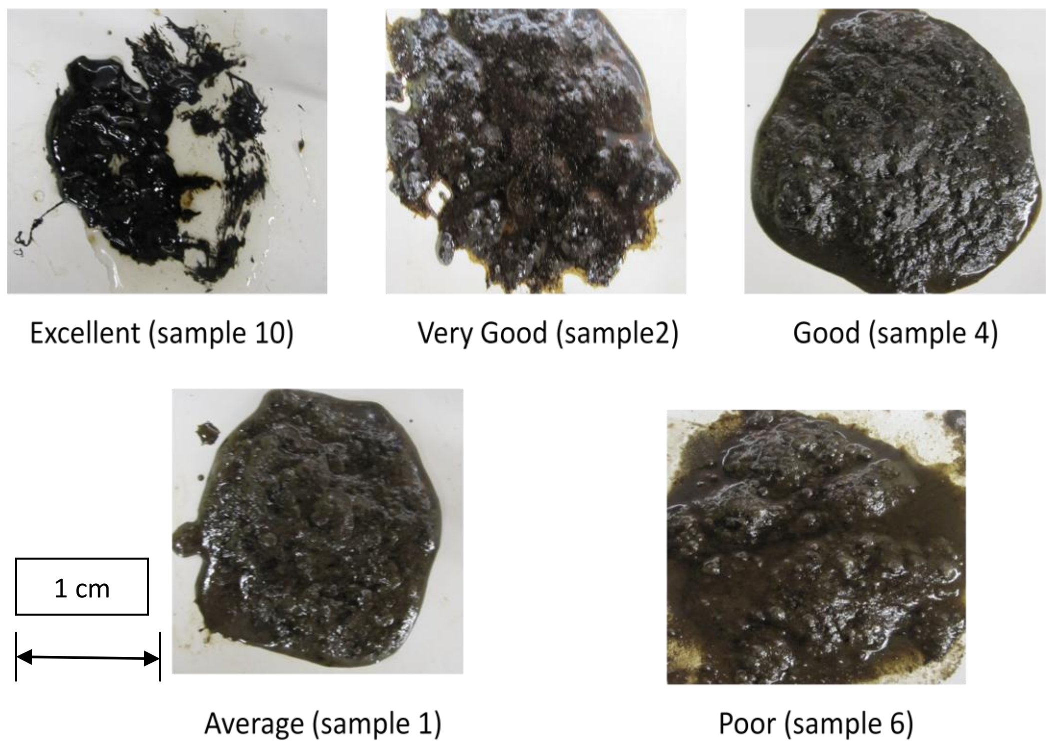


***Figure 3.5:*** *Photographs of froth*

Some care was taken in categorizing each froth sample. While ranking the performance both parameters should be considered carefully because the combined affect of the two factors give the estimate of recovery performace. For instance, in sample 10 the bubble concentration was poor but the bitumen per unit volume was high, which indicates that there was only bitumen floating at the surface. For sample 6, the bubble concentration was average but bitumen per unit volume of froth was low.

Table 3.7 gives the observation made on the froth after it was collected and allowed to settle. It was observed that the color of the bitumen and the bitumen content were the important features used for designing and controlling the processes for improved recovery.

Separation of three layers took place because of the sufficiently large density difference between the three components of the froth. It also suggests that there was no tendency to remain agglomerated or to emulsify. Some solids have a settling rate that is very slow, and so they were able to rise up to the froth layer with the bitumen. The presence of solids in the froth may also indicate that the detachment of some solids from the bitumen was not possible at the given operating conditions. In the industrial process, higher temperature or a higher rate of reagent addition can enhance this liberation [7]. A good separation would also mean a relatively easy post processing of froth. Color of the froth was used to classify the samples and the accuracy of the classification was checked using a hyperspectral feature based classification.

***Table 3.7****: Qualitative observations made after the froth was collected*

| Sample # | Volume of bitumen collected | Amount of fines settled at the bottom | Volume of water collected | Separation of the 3 layers | Color of froth collected |
|---|---|---|---|---|---|
| 1 | Average | Very Good | Very Good | Good | Brown |
| 2 | Very Good | Poor | Excellent | Excellent | Very Dark |
| 3 | Good | Excellent | Average | Good | Very Brown |
| 4 | Good | Good | Very Good | Very Good | Very Brown |
| 5 | Very Good | Excellent | Average | Good | Brown |
| 6 | Poor | Average | Average | Poor | Light |
| 7 | Excellent | Poor | Excellent | Very Good | Very dark |
| 8 | Good | Average | Average | Average | Dark |
| 9 | Very Good | Poor | Very Good | Very Good | Very Dark |
| 10 | Excellent | Poor | Poor | Excellent | Very Dark |

Figure 3.6 shows the froth of different samples collected in the jars. The volume of bitumen, solids (clay and sand), and water collected in the jars can be a good indicator of the processibility, provided that it correlates to the actual percentage composition in the froth, which is discussed below in the quantitative results section.

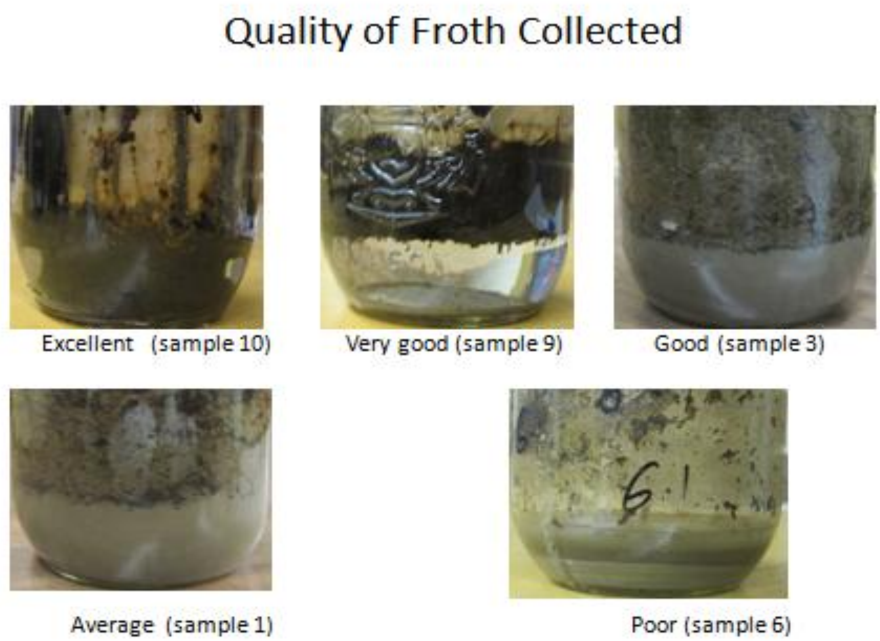


***Figure 3.6:*** *Froth of different oil sand samples collected in jars*

## 3.3.2 Quantitative Analysis

The collected froth samples and the homogenised oil sands samples were sent to Maxxam Analytics Inc. for Oil-Water-Solids analysis. Dean-Stark Analysis was used to determine the mass of bitumen, water and fines in the froth and the oil sand. In Dean Stark assaying, the bituminous solution is heated under reflux with toluene, which distills along with the water [7]. Evaporated solvent and water are trapped and weighed [7].

Figure 3.7 (a) shows the percentage of bitumen and solids in each of the ten homogenised oil sands types, and for the froth from these samples, respectively.

Figure 3.7 (b) gives the percentage of bitumen and solids in froth generated by each oil sands type.

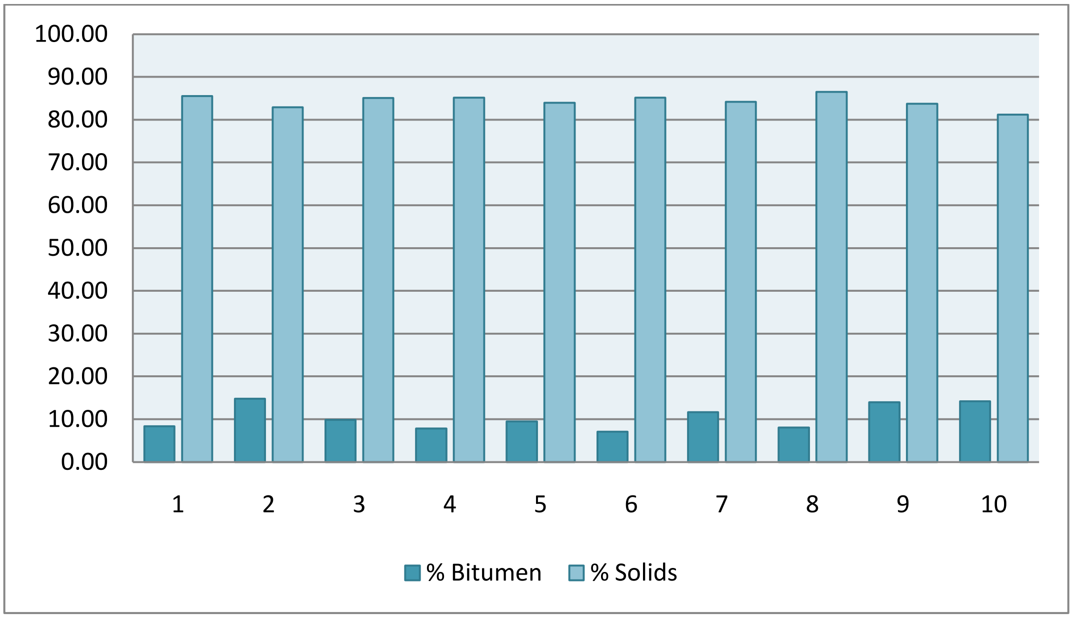


***Figure 3.7(a):*** *Percent bitumen and solids content in the oil sands sample*

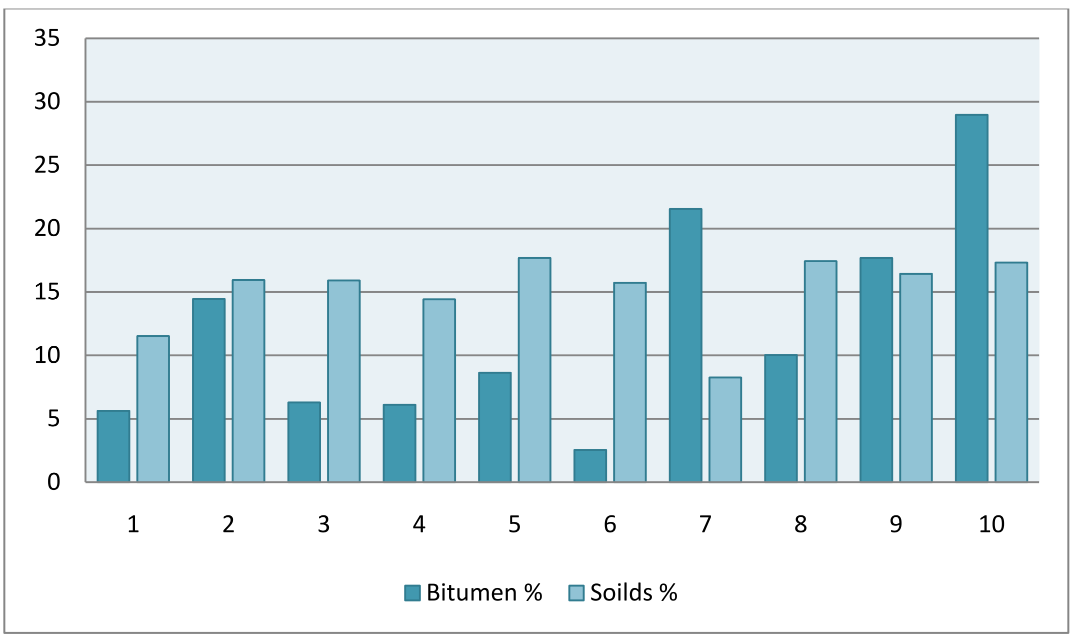


***Figure 3.7(b):*** *Percent bitumen and solids content in froth*

The percentage of solids in the ore of different samples lie within a narrow range; but the percentage of bitumen shows considerable variation. The bitumen recovery from the froth of each sample varies greatly. Both these interpretations are necessary to measure the processibility of each sample. Good processibility means high bitumen content and low solids content in the froth. This leads to consideration of how much bitumen present in the crude oil sands is recoverable by flotation processes. Figure 3.8 shows the fraction of bitumen recovered from the homogenised oil sands at the four different operating conditions.

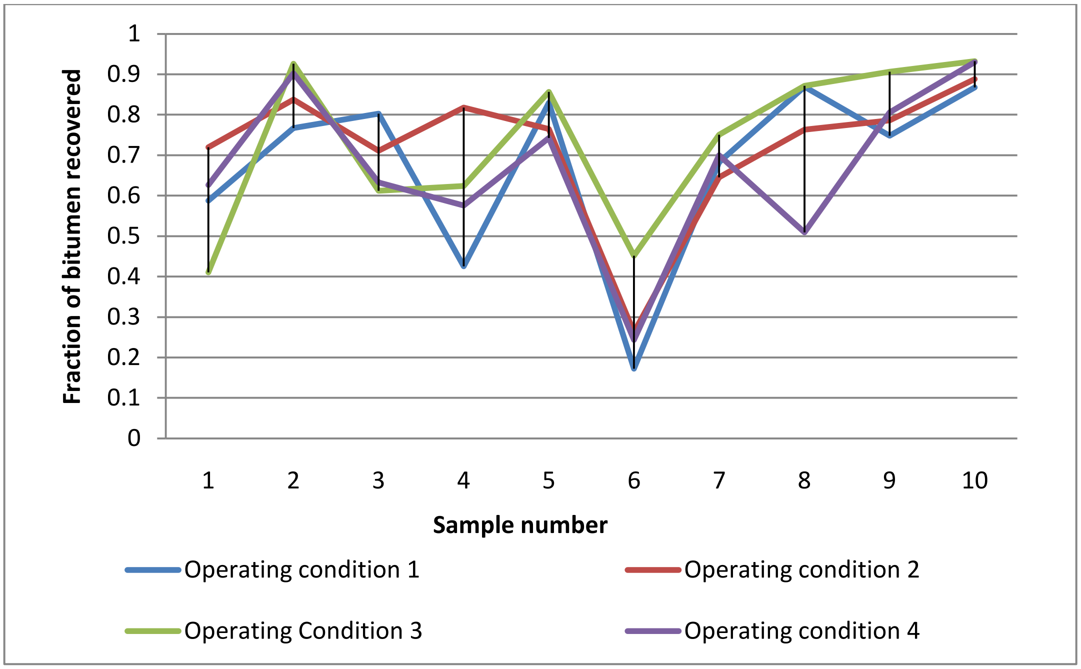


***Figure 3.8:*** *Fraction of bitumen recovered from each sample at four different operating conditions*

It can also be inferred from figure 3.8 that while moving from operating condition 1 (1200 RPM & Airflow rate; 100 ml/min) to condition 2 (1200 RPM & Airflow rate: 200 ml/min), in most of the cases the recovery increases while moving from condition 3 (500 RPM & Airflow rate 100 ml/min) to condition 4 (500 RPM & Airflow rate 200 ml/min) the recovery drops. This can be explained by reasoning that at lower impeller speed an increase in the aeration rate increases the bubble concentration and hence the recovery. At higher impeller speed, an increase in the aeration rate will lead to greater number of collision which may lead to the detachment of bitumen form the bubbles. It can also be inferred that in most of the cases the increase in the impeller speed (condition 2 to condition 3) leads to increased recovery. In general sample 10, 9, 7 and 2 had good processibility and it is also interesting to note that their recovery at all the operating conditions varied over a narrow range as compared to the sample with poor processibility such as samples 1, 4 and 6. Figure 3.9 shows the average of bitumen recovery for all the operating conditions and the original content of bitumen in oil sands.

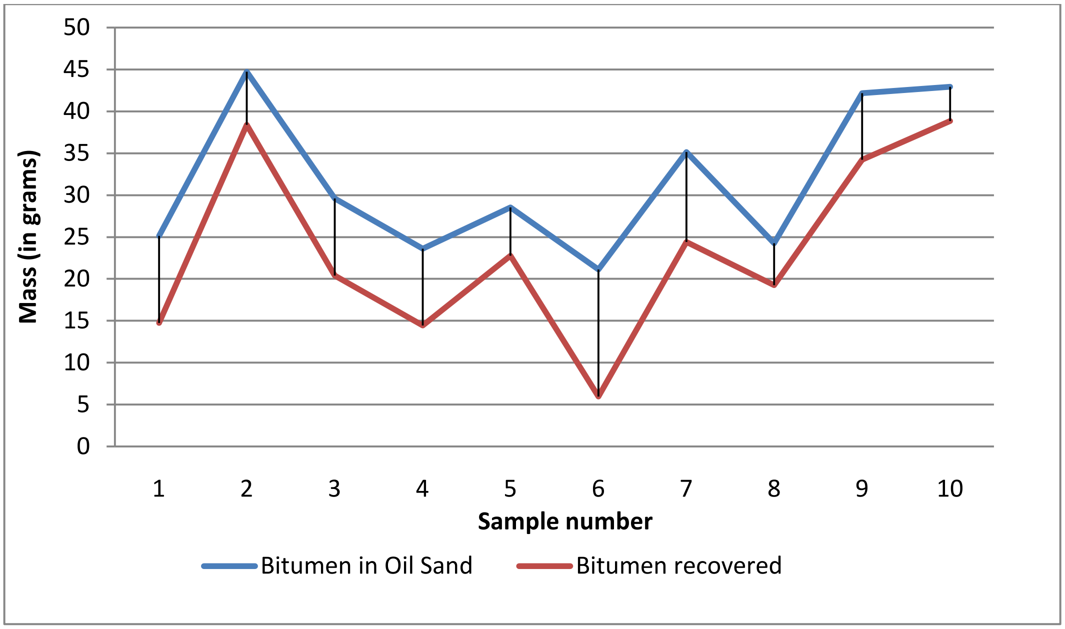


***Figure 3.9:*** *Average (of the 4 operating conditions) fractional recovery*

It can be noticed in figure 3.6 (d) that most of the samples which had high bitumen content in oil sands had high recovery with exception of samples 3 and 7. This can be explained by the following logic:

Composition of the oil sand: The amount of bitumen, solids and water mainly defines the ore type but their mutual hydrophobic/hydrophilic properties [9] play a vital role in liberation of the bitumen from the sand and clay. These properties make the detachment of bitumen form sand dependent on the ore type. The particle size of the solids also plays a crucial role in bitumen-sand interaction [10]. It is generally observed that smaller the particle size greater the attraction towards the bitumen. Alkalinity of the solution also affects the liberation of the bitumen [10]; at pH>6 the sand particles easily get liberated from the bitumen surface while at pH<6 there exists a strong attachment between them. All these factors can be put together to explain why a high bitumen rich ore may not always lead to highest recovery of bitumen via flotation process.

After comparing table 3.7 and figure 3.6 (d) if the samples which produced dark and very dark froth are labelled as dark (samples: 2, 7, 8, 9 and 10); and the samples which generated brown and very brown froth are labelled as brown (samples: 1, 3, 4 and 6) then it can be observed from figure 4.6 (d) that samples labelled as dark had better recovery from their respective ore than samples labelled as brown, which indicates that the qualitative assessment of the ore was a reasonable gauge for recovery. This can be explained by the following logic:

As noted in [10], the bitumen recovery is a function of the size and mass of the aggregate floating to the froth layer. Larger size and higher mass of the aggregates usually means higher recovery. The same information was inadvertently captured by the parameters: bubble concentration and bitumen per unit volume of froth. There is a good correlation between high bitumen per unit volume of froth and high bitumen recovery. The color of the froth is also a very good indicator of the bitumen content in the froth; the very dark color froth had the highest bitumen content, light brown had the lowest bitumen content.

The experiment run time was 15 minutes but some froth still remained floating on the slurry after 15 minutes. The extra amount of time taken to skim of the froth is given in table 3.5. In order to estimate the total recovery, one can use the recovery results (for 15 minutes) of Dean Stark assay to calculate rate constant $k$ from the following first order equation (discussed earlier in Chapter 2, section 2.1.4)

$$C = C_0 e^{-kt} \tag{3.1}$$

The initial concentration ( $C_0$ ) was calculated using the bitumen content in the homogenised oil sand. The initial volume of water was 950 ml of water plus the water content in the oil sand. The final concentration ($C$) was the mass of unfloated bitumen remaining in the tank per unit volume of water left in the tank. The time $t$ was taken to be 15 minutes. After calculating rate constant $k$, the same equation was used to calculate the total recovery after total time (15 minutes plus the extra time shown in table 3.5). Figure 4.10 gives the total estimated fractional recovery averaged for all the four operating conditions.

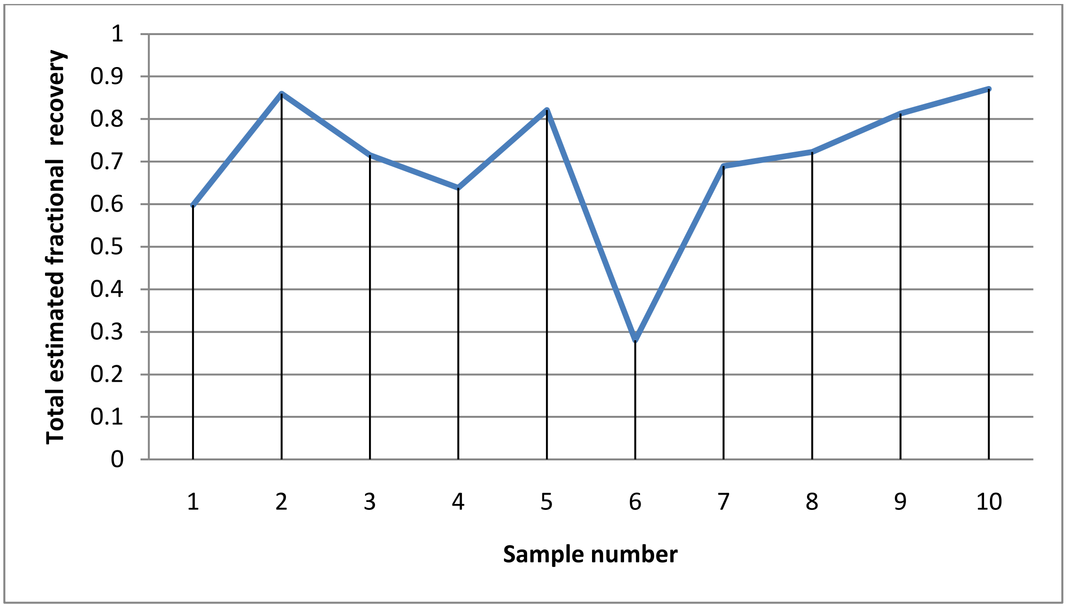


***Figure 3.10:*** *Total estimated fractional recovery (averaged over all the four conditions)*

## 3.3.3 Hyperspectral Analysis Results

The results of the analysis of the hyperspectral images of the ore and the froth are presented in the subsequent sections. The instruments were handled by Dr. Jilu Feng while the analysis was done by Dr. Benoit Rivard and Dr. Jilu Feng.

### 3.3.3.1 Analysis of the Ore

Figures 3.7(a) and 3.7(b) show the ASD and FTIR reflectance spectra over the spectral regions of interest. The spectra were collected from three samples: the white coloured shape is sample 10; the green coloured shape is sample 4; and the red coloured shape is sample 9. Labels C, O, and Q in the figures represent clay, oil and quartz features, respectively.

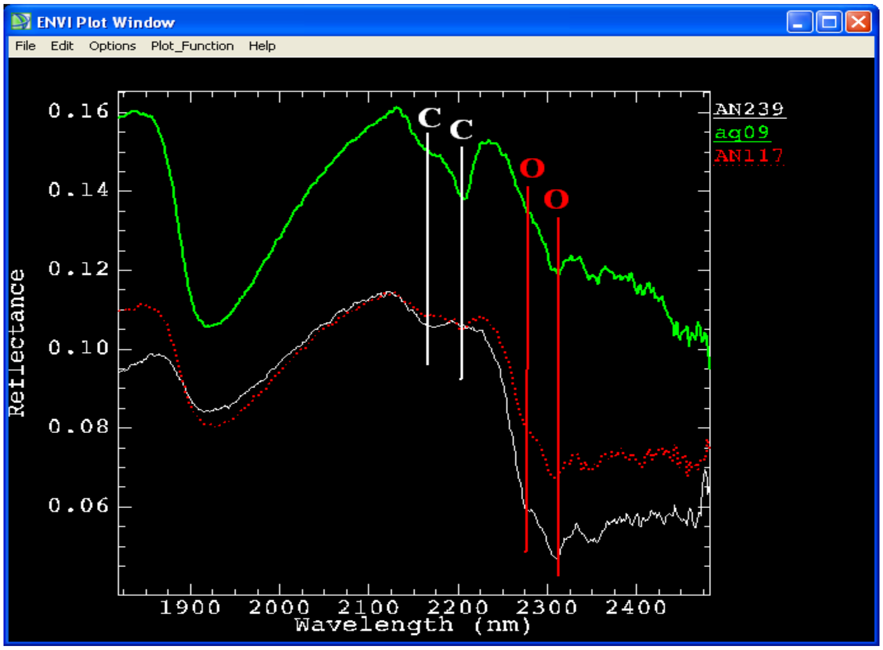


***Figure 3.11(a):*** *ASD reflectance spectra (courtesy Rivard et.al[8])*

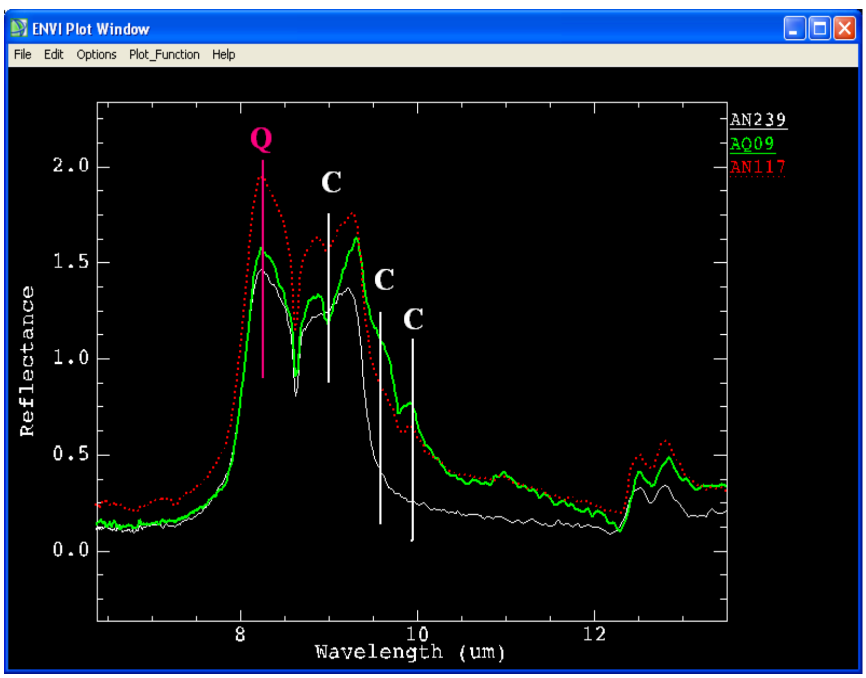


***Figure 3.11(b):*** *FTIR reflectance spectra (courtesy Rivard et.al[8])*

A feature is a change in spectral shape at a particular location that relates to reflectance from a component in the sample. Locations of features are characteristic for a material. Locations of known features can be found in standard spectral library, such as the JHU Spectral Library. Table 3.8 gives the locations for components of interest found in oil sands ore.

***Table 3.8:*** *Spectral feature locations for oil sands sample*

| **Components** | **Spectral Feature Locations** |
|---|---|
| Bitumen | 1300, 1700, and 3700 nm |
| Clay | 2100, 2230, and 8900 nm |
| Quartz | 8200 and 9200 nm |

In general, the band depth (change in reflectance) determines the percentage composition of a particular material. For example, in Figure 3.11(a), sample 4 (green) has the highest band depth over the region 2100-2230 nm, suggesting it has the highest clay content. FTIR spectra are useful in determining the relative abundance of quartz and clay in the solids. From Figure 3.11(b), it can be inferred that sample 9 (red) has the highest quartz composition amongst the samples shown.

Prediction from spectra of the bulk homogenised samples were made to determine the Total bitumen content (TBC) and fines (Pp44) content using the model developed by Lyder et.al. [4]. The complete mathematical model can be found in [4]. Figure 3.12 shows the relationship between the true and estimated values of bitumen content for the samples of interest highlighted in red amongst all oil sands samples tested.

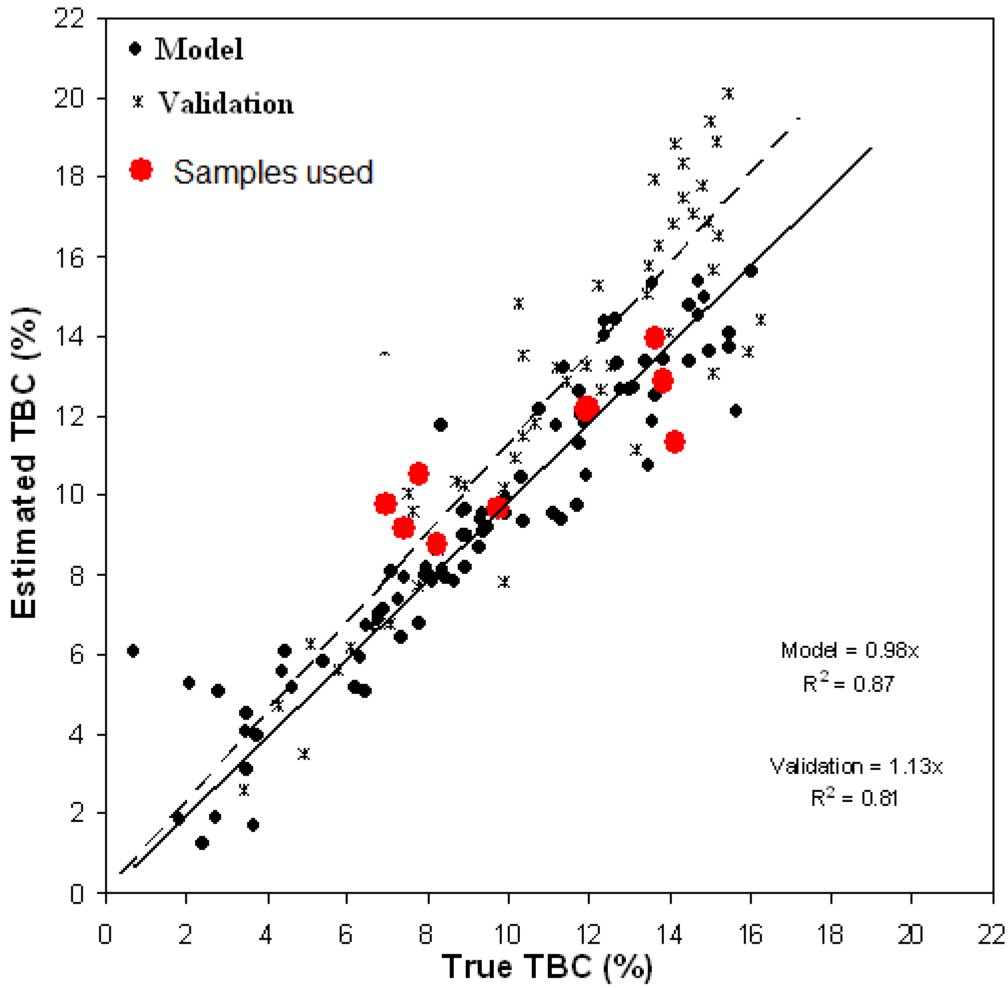


***Figure 3.12:*** *Relation between the estimated TBC and true TBC (courtesy Rivard et.al [8])*

Figure 3.13 shows the true <44 um fines content for a set of ores, and the estimated fines content based on spectral features, with the ten samples in this study highlighted in red. The rms error for fines prediction for the samples used was 6.53% while the rms for the model and validation was 6.09% and 7.35% respectively.

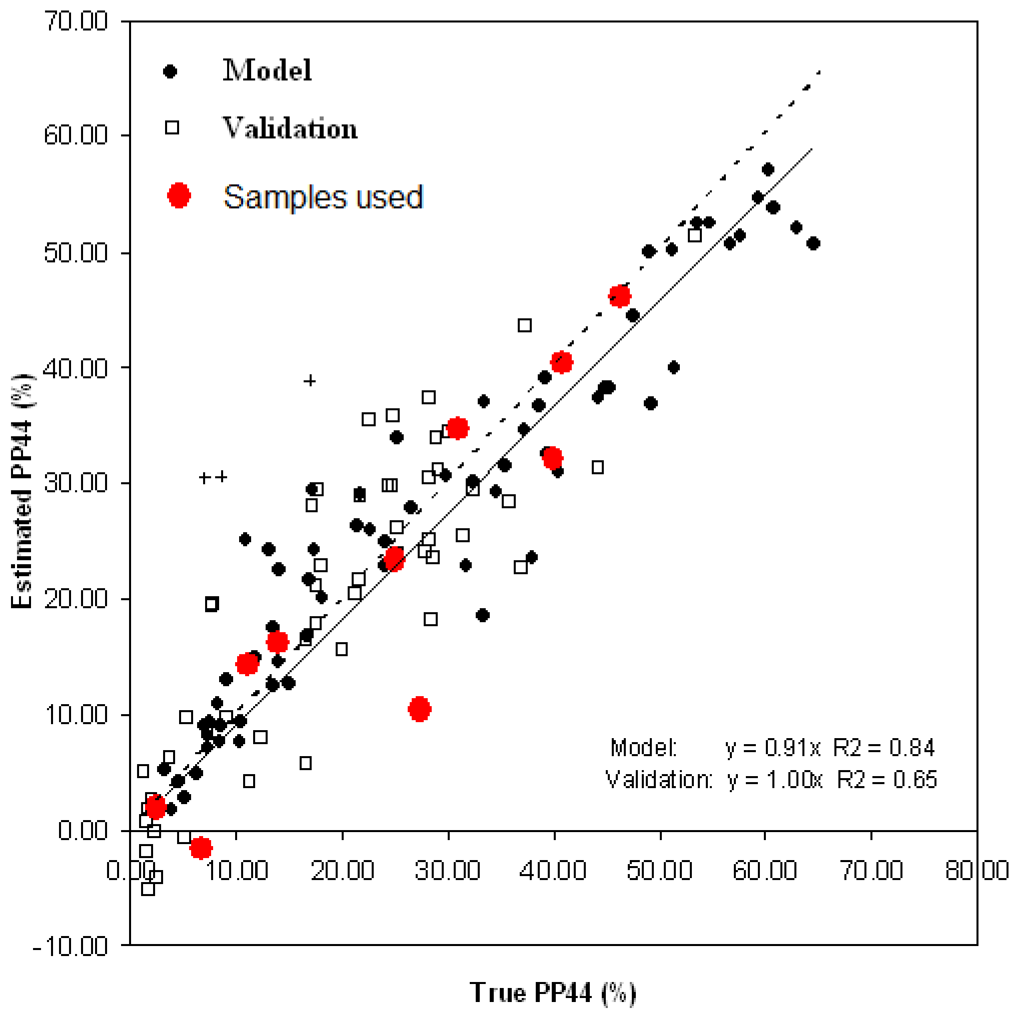


***Figure 3.13:*** *Relation between the estimated fines content and true fines content (courtesy Rivard et al. [8])*

Figure 3.14 shows the relation between of clay content (Pp 3.9) with the true oil content in the bulk sample. The ores were classified into two categories: one which generated brown froth (including very brown froth) shown as red dots, and the other which generated dark (including very dark) froth shown as green dots on the plot.

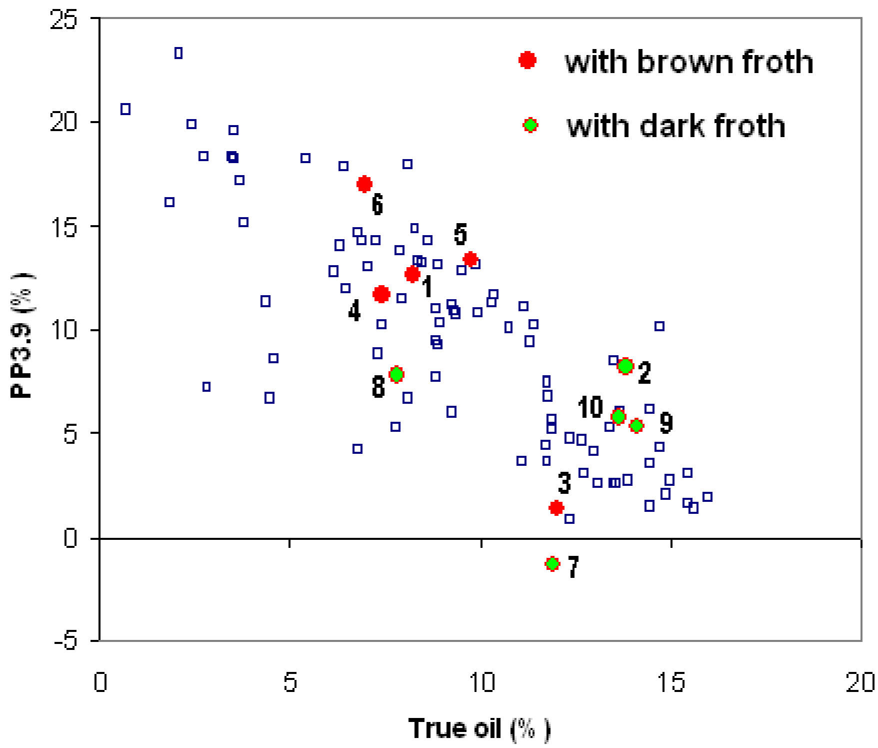


***Figure 3.14:*** *Relation between the fines content and oil content (courtesy Rivard et al. [8])*

All the samples could be categorised into two classes with expectation of sample 7 and 8. Further investigation into grain size will be done to explain the case of sample 7, which deviates from the model. As discussed in the quantitative analysis section, an ore labelled dark had better recovery from its ore. This would indicate that most of the ores labelled as dark had lower fines and better recovery, hence, better processibility (and vice-versa).

### 3.3.3.2 Analysis of the Froth

A two-class classification was devised based on the color scheme defined in the previous section for percentage fines. Class ID=0 was dark and had less than 25% fines; and class ID=1 was brown and had more than 25% fines. Table 3.9 gives the details of classification. Continuous wavelet analysis (CWA) was conducted on the ASD and TIR spectra to detect the spectral features that correlate to the two classes. CWA is a signal processing technique based on the principle that a reflectance spectrum can be represented as the sum of wave-like functions (wavelets) [11]. The representation of an original spectrum as a suite of spectra known as wavelets helps to capture spectral features of different widths, called scales [12].The shape of the wavelet base carries the information of the property of features present in the original spectrum [12] and $2^{nd}$ order derivative of Gaussian (DOG) can be used as the base [12]. Mathematical details of the analysis can be found in [12].

Seven features were found from the ASD spectral data (correlation coefficient greater than 0.92) and eight features were found from TIR spectral data (correlation coefficient greater than 0.90).

**Table 3.9:** Two class classification based on froth colour and fines composition

| Sample # | Color | % Fines | Sample ID | Color ID |
|---|---|---|---|---|
| **1** | **Brown** | **31.00** | MC09 | **1** |
| **2** | Very Dark | 11.13 | AN225 | 0 |
| **3** | **Very Brown** | **27.30** | AN397 | **1** |
| **4** | **Brown** | **40.06** | AN155 | **1** |
| **5** | **Very Brown** | **40.75** | AN178f96 | **1** |
| **6** | **Light Brown** | **46.24** | AQ09 | **1** |
| **7** | Very Dark | 6.71 | AN178f26 | 0 |
| **8** | Dark | 24.98 | AN229 | 0 |
| **9** | Very Dark | 13.83 | AN117 | 0 |
| **10** | Very Dark | 2.44 | AN239 | 0 |

It was possible to isolate the dark froths from the brown froths by employing simple 3-band composition (Short wavelength Infrared) on the ASD spectra. Figure 3.15 (a) shows the ASD spectral profile for the froths. The red, green, and the blue lines in the figure correspond to 937 nm, 2160 nm, and 2200 nm bands. Figure 3.15 (b) shows location of the froth in the three band composite of wavelet power at 937nm, 2160 nm and 2200 nm.

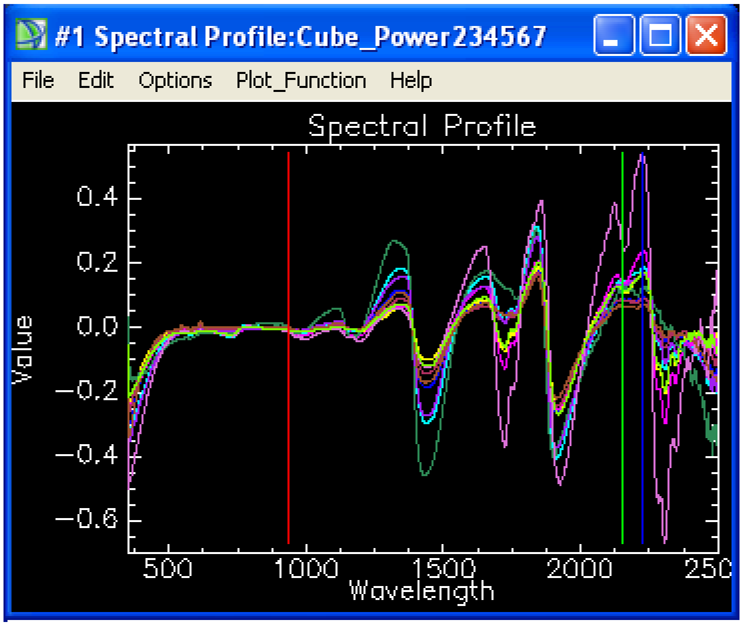


***Figure 3.15(a):*** *ASD spectral profile of the froths (courtesy Rivard et al. [8])*

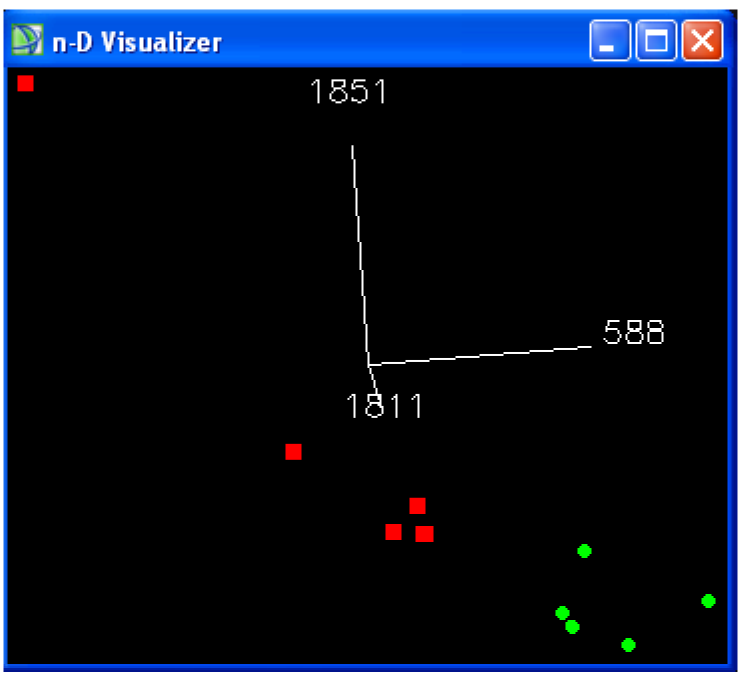


***Figure 3.15(b):*** *Three band composition of froths (courtesy Rivard et al. [8])*

While the dark froths (shown as green in Figure 3.15(b)) are tightly clustered, the brown froths are scattered. This suggests that the relative composition of the brown froths varies greatly and the relative composition of the dark froths bear some resemblance. Such information may be very useful for controlling the process, by exploiting the anomaly of spectral variation when bitumen froth exhibits spectral variability. This makes intuitive sense, as froth with low fines content should exhibit strong bitumen features and little evidence of clay or quartz mineralogy (or heavy minerals and other contaminants).

The same procedures were carried out on TIR spectra. Figure 3.16(a) shows the froth TIR spectra with the red, blue, and green lines corresponding to 8.5 µm, 9.8 µm, and 8.9 µm respectively.  Figure 3.16 (b) shows the location of the froths in the three-band composition. As noted in the ASD spectra 3 band composition, the TIR 3 band-spectrum was able to isolate the brown and the dark froth. The brown froths were again were loosely clustered, while the dark froths were tightly clustered.

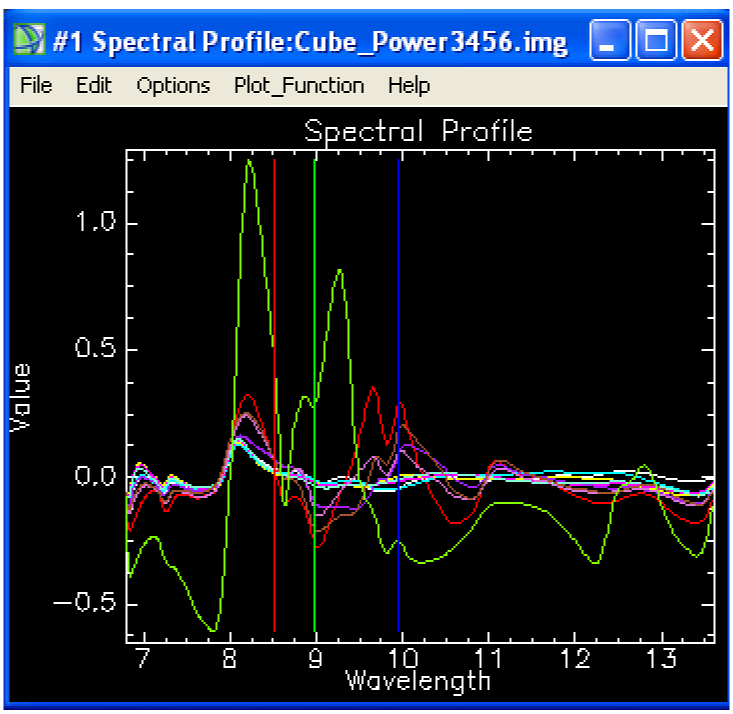


***Figure 3.16(a):*** *TIR spectral profile of the froths (courtesy Rivard et al. [8])*

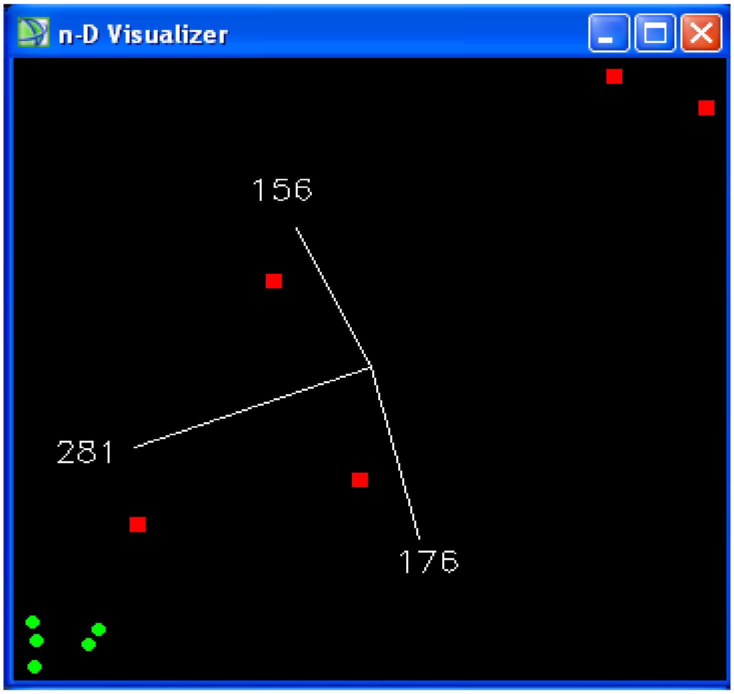


*Figure 3.16(b): Three band composition of froths (courtesy Rivard et al. [8])*

## 3.4 Error Analysis

The experiments were prone to both human as well as machine error. Error could occur while manually mixing the oil sands after comilling. Error could also occur in weight measurements while sub-sampling each oil sand. Oil sand was exposed to air at certain occasions and hence can loose some moisture. Since the froth from the Denver cell was manually collected, it can suffer from the efficiency of the worker. Also, sometimes the bitumen floating at the top of the slurry used to stick to the walls, thereby reducing the amount collected. Spectral imaging requires flat surface for the target but unfortunately both the homogenised ore as well as the froth had uneven surfaces thus affecting the accuracy of the measurements.

## 3.5 Discussion

A set of flotation experiment was conducted with an objective of relating hyperspectral features to the processibility. The color of the froth correlated well with the processibility of the oil sands. Features associated with bitumen, silica, and clay was readily visible. As well, some features were present when separation performance was good but froth quality was poor. Detailed analysis of mineralogy is proceeding to determine how components that may adversely affect processability may be observed as the extraction process is operating. Previous model (Lyder et.al. [4]) based on hyperspectral feature was able to predict the bitumen and fines content in the homogenised oil sands ore with good accuracy. With the help of hyperspectral analysis, it was possible to classify the ores based on the color of the froth generated. Hence, indirectly hyperspectral features correlate with the processibility of oil sands.

Hyperspectral features extracted from the froth (both in-situ and after the process) enabled not only to closely relate the observable features to processibility of the ore during the operation but can also helpful for further downstream steps. For example, the distribution and composition of solids such as quartz, clay minerals in the froth have direct bearing on the further processing of the froth. Hence, timely information of distribution and composition of the solids can be used to observe the separation process. Detail analysis of the mineralogy to determine the components that adversely affects the recovery.

# References:


[1] Fong N, Ng S, Chung KH, Tu Y, Li Z, Sparks BD, Bitumen recovery from model systems using a warm slurry extraction process: effects of oil sands components and process water chemistry. Fuel 2004;83:1865–80.

[2] Schramm LL, Stasiuk EN. Surfactants in Athabasca oil sands slurry conditioning, floatation recovery, and tailings processes. In: Schramm LL, editor. Surfactants: fundamentals and applications in the petroleum industry. Cambridge University Press; 2000.

[3] Wikipedia (http://en.wikipedia.org/wiki/Hyperspectral_imaging) date accessed 2011-01-19

[4] Lyder, D., Feng, J., Rivard, B., Gallie, A., Cloutis, E. (2010). Remote bitumen content estimation of Athabasca oil sand from hyperspectral infrared reflectance spectra using Gaussian singlets and derivative of Gaussian wavelets. *Fuel, 89*(3), 760-767.

[5] Benoit Rivard, Jilu Feng, A. Gallie. Estimating chalcopyrite and pyrrhotite/pentlandite in ores of the Subury mnines using visible and infrared spectroscopy. International Journal of Remote Sensing 23(11):2229-2246, 2002.

[6] Jim Shwarak, Department of Chemical Engineering, University of Alberta

[7] (http://en.wikipedia.org/wiki/Dean-Stark_apparatus) date accessed 2011-01-19

[8] B. Rivard, J. Feng, V. Bhushan, and M. Lipsett, Infra red reflectance hypspectral features of Athabasca oil sand ore and froth, Whispers, 2011, Lisbon, Portugal.

[9] Ng S., Warszynski P., Zembala M., Malysa K., "Bitumen-air aggregates flow to froth layer: II. Effect of ore grade and operating conditions on aggregate composition and bitumen recovery" (2000) *Minerals Engineering*, 13 (14-15), pp. 1519-1532.

[10] Dai, Q. and K., Chung, “Bitumen-Sand Interaction in Oil Sand Processing”, *Fuel* **74**, 1858–1864 (1995).

[11] J. Feng, B. Rivard, A. Gallie, and E. Cloutis, Feature selection and broad band bitumen content estimation of Athabasca oil sand from infrared reflectance spectra, Whispers, 2009

[12] Rivard B., Feng J., Gallie A. and Sanchez-Azofiefa A., “Continuous wavelets for the improved use of spectral libraries and hyperspectral data”, Rem. Sens. Environ. Vol.112, pp.2850-2862, 2008

**Chapter 4**

# Damage Modeling

Flotation process is mineral processing technique which typically involves agitation and aeration of slurry. The agitation enables the liberated mineral particles to collide and attach to the bubbles rising at the top. The bubbles report to the froth and are mechanically skimmed off. Undesired fines and solids, often entrained in the impeller stream might attack the wall of the cell, leading to material loss and eventually loss of structural integrity. In this chapter, the empirically developed equations for the flow field (available in literature) in a simple mixing vessel are verified by using Particle Image Velocimetry (PIV) technique. An Eulerian-Langrangian approach is used to determine the particle trajectories and the effect of squeeze film is incorporated to determine the particle-wall interaction and energy dissipation at the walls. A wear model which takes into account, the impact velocity, attack angle, hardness properties of the impinging particles and the surface is developed for material removal rate. Particle Image Velocimetry techniques were used to measure the impact velocities and impact angles.

A flotation cell is subject to different types of faults, such as mass imbalance and misalignment of the impeller shaft, and deformation of the impeller blades. The damage mechanism of interest in this work is wear, which is most prevalent on the walls of the vessel and on the impeller. Wear occurs in these process units because the process fluid contains solid particles that are entrained with the impeller stream and can contact the impeller or the wall of the vessel. If the particles have sufficient energy, they may transfer some of that energy into the impeller blades or the wall of the vessel, resulting in erosion damage. Modeling wear sequentially follows the following steps:

I. Modeling of the fluid flow in the given geometry;

II. Predicting the motion of abrasive particles under the fluid field (the impact velocities and the impact angle at the surface of the walls); and

III. Determining the amount material removal using an appropriate wear model and the impact velocities and impact angles found in step II.

The Platzer *et al.* [1] model discussed in chapter 2, section 2.2.2.2 was used to model the flow of liquid in the mixing vessel. Modified Stokes drag equation (as discussed in Chapter 2, section 2.3.2.3) was used to calculate the impact velocity and impact angles at the walls. Thin film model developed by Clark et al. [2] (presented in Chapter 2, section 2.4.2) was used to account for the velocity reduction just in front of the wall. Finally, Oka's [3,4] wear model was used to determine the material removal by single particle impingement. In order to combine all the individual impact events a damage model was developed and is discussed in the following section.

## 4.1 Damage Model

In slurry process equipment, the energy required to cause wear damage comes from the process, that is, kinetic energy transferred to the solids via impeller action. Only a fraction of the kinetic energy lost in the impingement process contributes to the damage, when energy transfer exceeds a certain threshold [5]. In order to determine the overall damage accumulation at the locations of interest, the individual wear events must be connected together over a period of time.

Consider a small cylindrical strip of height $dz$ and radius ($r$) equal to the radius of the vessel, as shown in Figure 4.1. If $m$ is the average mass of the impinging solid particles and $f$ is the impact frequency per unit area, then the total mass of the particles impinging on the strip, $M$, over a time $dt$ is given by

$$M = mfdt \times 2\pi rdz \tag{4.1}$$

If $dQ$ is the volume of material removed (Figure 4.2), then following the definition of erosion rate $E(\theta)$ and using equation (2.40) we get:

$$E(\theta)=\frac{dQ}{M}=g(\theta)E(90) \tag{4.2}$$

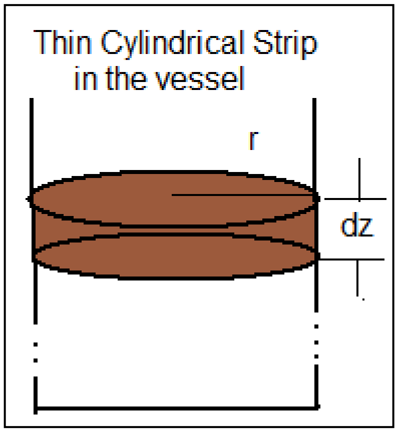


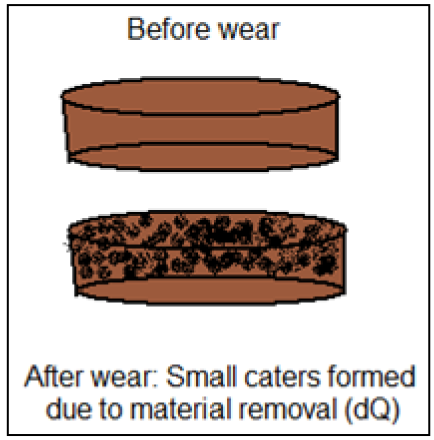


***Figure 4.1***:*Cylindrical strip of radius r* ***Figure 4.2***: *Material Removal by erosion*

$$d\dot{D}=\frac{dQ}{dt}=g(\theta)E(90)(mfdt\times 2\pi rdz) \tag{4.3}$$

where $D$ represents the cumulative damage and $\dot{D}$ represents the damage rate. As noted earlier, erosion rate $E(\theta)$ is a function of the axial distance ($z$) in the vessel. This implies that $d\dot{D}$ is also a function of ($z$). The integral of $d\dot{D}$ over a height of interest would yield the damage rate ($\dot{D}$) as:

$$\dot{D}=\int \mathrm{d}\dot{D}=\int_0^h g(\theta)E(90)mf\,(2\tau rdz) \tag{4.4}$$

Eventually, integral of $\dot{D}$ over a period would give the total damage accumulated for that time.

$$D=\int_0^t \dot{D}dt=\int_0^t\int_0^h g(\theta)E(90)mf\,(2\tau rdz)dt \tag{4.5}$$

One can similarly find the total damage accumulated through abrasive wear. If the cumulative damage exceeds a particular value, the component needs to be replaced or refurbished.

In an order to measure the process following information is needed:

1) Impact speed and impact angle
2) Concentration, size and the density of the particle
3) Impact frequency of the particles over the area which covers the impeller jet at the wall

Impact speed and impact angles can be calculated through numerical calculations using software packages such as CFD. Experiments such as hot wire anemometry, PIV are used at laboratory level to calculate the particle speeds and angle. Concentration, size and density of the particle can be deduced by analysis of a know sample of the working fluid. Rate of collisions can be known by using acoustic emissions techniques in the region of interest.

## 4.2 Experimental Verification of the Flow Field

A set of experiments was designed to determine the impact velocity and the impact angle at the walls of an idealized system, and to compare them with the flow field model. Flow visualization of a system with many particles is key to determining the particle flows. Ideally, a viewing section on the wall of the cell can be used to observe the motion of a particle and the flow field using an optical technique such as Particle Image Velocimetry (PIV). In PIV, tracer particles are added to the flow and the particles are illuminated twice within a short interval of time in a plane of flow. The light reflected from the particles is recorded in a single frame, or in a sequence of frames, and the displacement between the light images in that interval gives the velocity of the fluid in the region of the particle. Figure 4.3 (a & b) shows the experimental set-up for PIV experiment. As shown in the figure 4.3 (b) laser was used to illuminate a plane and two cameras 90 degrees apart to the photographs of the illuminated plane.

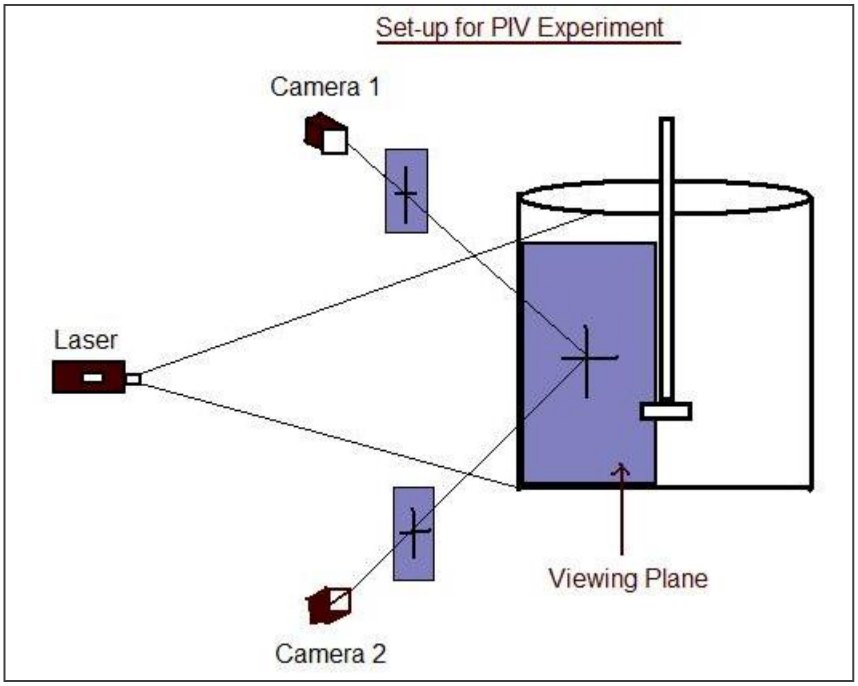


***Figure 4.3(a):*** *Experimental set-up for PIV Experiment*

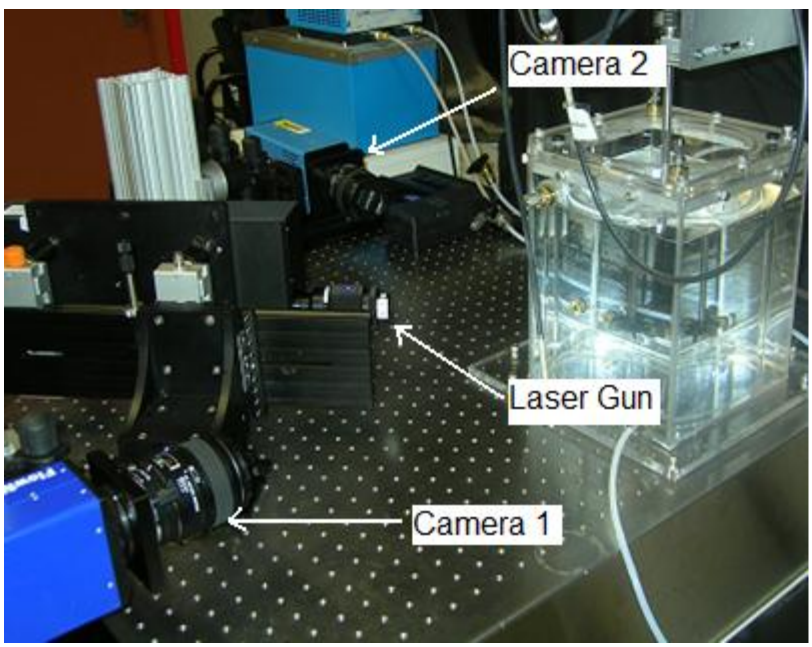


***Figure 4.3(b):*** *Laboratory set-up for PIV experiments*

## 4.2.1 Experimental Set-up

Optically clear cylindrical glass vessel with refractive index 1.4585 and diameter (D) 190 mm was used. The impeller diameter was d=D/3 and the off bottom clearances (C) chosen were D/3 and D/5. Height of the tank (T) was equal to the diameter (D) of the tank. Table 4.1 gives the different parameters described in flow field modeling and their value for the mixing process.

***Table 4.1***: *Parameters chosen for mixing process*

| ***Parameters*** | ***Value*** |
|---|---|
| D, d | 0.190 m,0 .0633m |
| H, h | 0.195 m, 0.190m |
| w | 0.0126m |
| n | 8.33 rps |
| P | 90 Watts |
| $V_F$ | 0.001162 $m^3$/sec |
| $c_F$ | 0.7 |
| $c_p$ | 5.5 |
| $\sigma$ | 10.5 |
| *B'* | 3.878 |
| *a* | 0.0255 |
| *A* | 0.02 |
| Re | 32,426 |

A viewing box was built around the vessel so that the flow could be viewed without refractive errors in direction perpendicular to viewing plane while using PIV (Figure 4.4 (a & b)). The two cameras were 90 degrees apart and the laser source was placed exactly at the centre of the two cameras.

Velocities are determined by calculating the displacements over time. Hence, errors in measurements could occur due to error due to the camera resolution (displacement error) and data acquisition and processing systems (time calculation error). The smallest resolution possible with the PIV technology used was 0.39 mm; hence the separation between the layers was 0.39 mm.

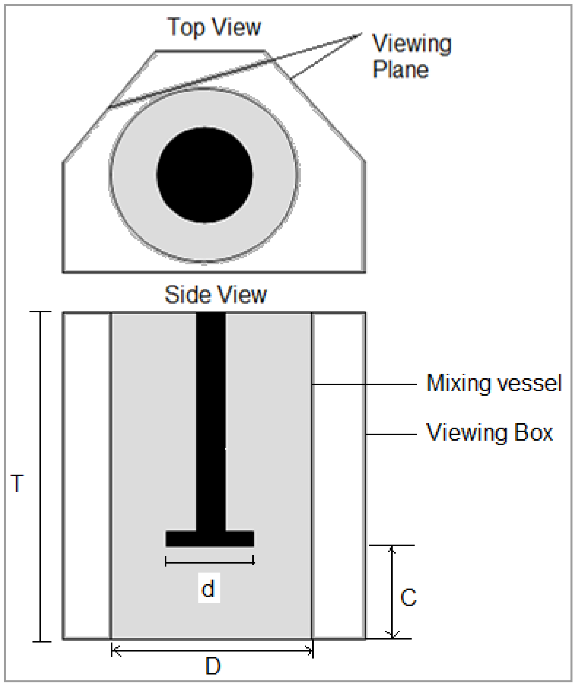


***Figure 4.4 (a):*** *Schematic of the test section*

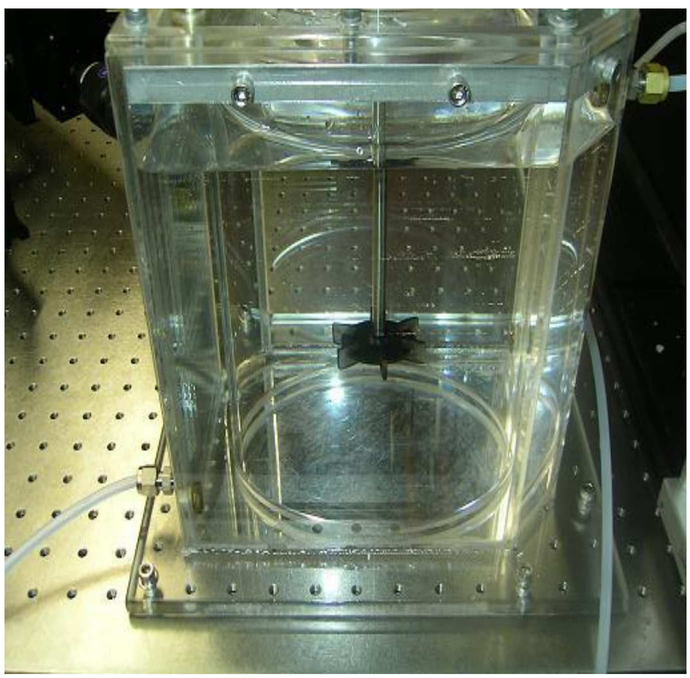

***Figure 4.4 (b):*** *Test section for PIV*

Density of tracer particles close to density of fluid to avoid: Effect of gravitational force and scattering (if density of particle is very less). To determine the velocity of particles in the vessel silica particles were added to the fluid without the tracer particles. Table 4.2 gives the experimental parameters for the PIV experiment.

Table 4.2: Parameters for PIV experiment

| ***Parameters*** | ***Values*** |
|---|---|
| Tracer Particle Sizes | 18 (Hallow glass) and 74 micron (Glass beads) |
| Impeller speeds | 300,400 and 500 RPM |
| Concentration of Solids | 3% by the weight of Liquid |
| Sampling Frequency | 4 photos per second |
| Silica particle sizes | 350, 450 and 545 microns (approximately) |

## 4.2.2 Results

PIV results provided velocity information of the continuous phase as well as the dispersed phase (solids) at various pre-selected spatial locations. Figure 4.5 & 4.6 shows a front-view half-section of the vessel in 2-D for two different particle sizes. The small arrows in the picture represent the velocity vector of the tracer particles. The image shows a distinct radial jet and two circulation loops.

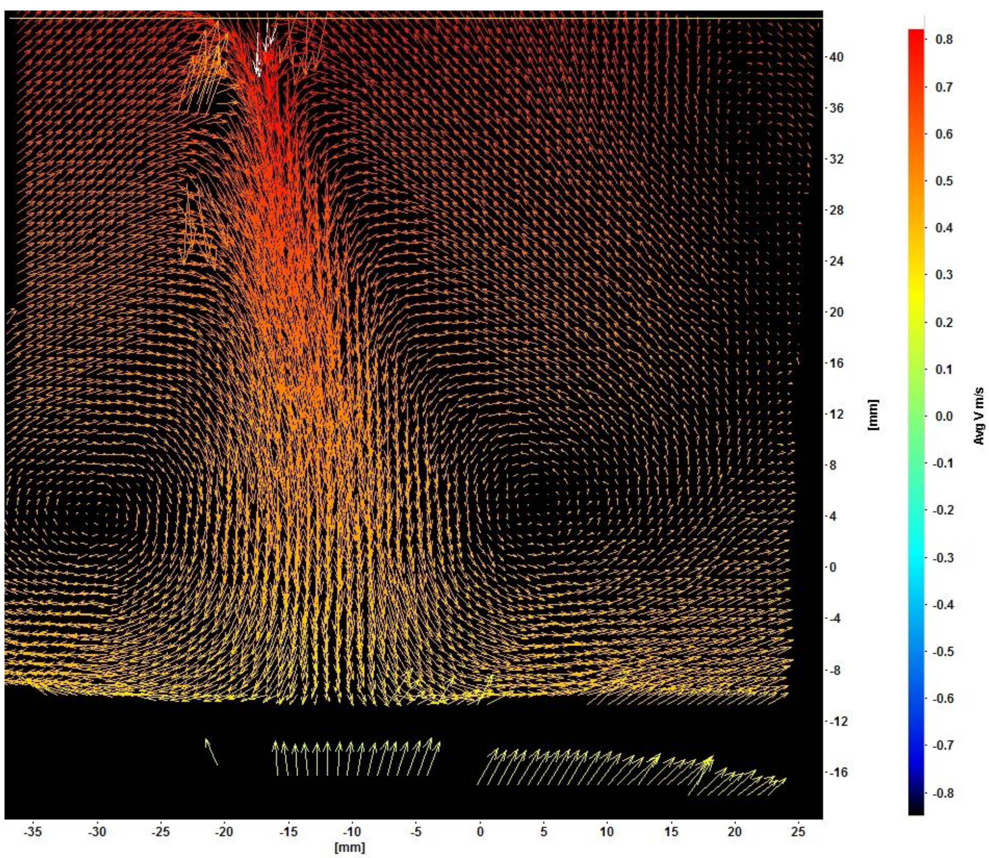


***Figure 4.5:*** *PIV image of 18 $\mu$ (500 RPM)*

It is evident from the image that 18 micron tracer particle more faithfully follow the fluid flow than 74 micron. This is because inertial effect of 74 micron tracer particles are more pronounced than the 18 micron one at the same impeller speed.

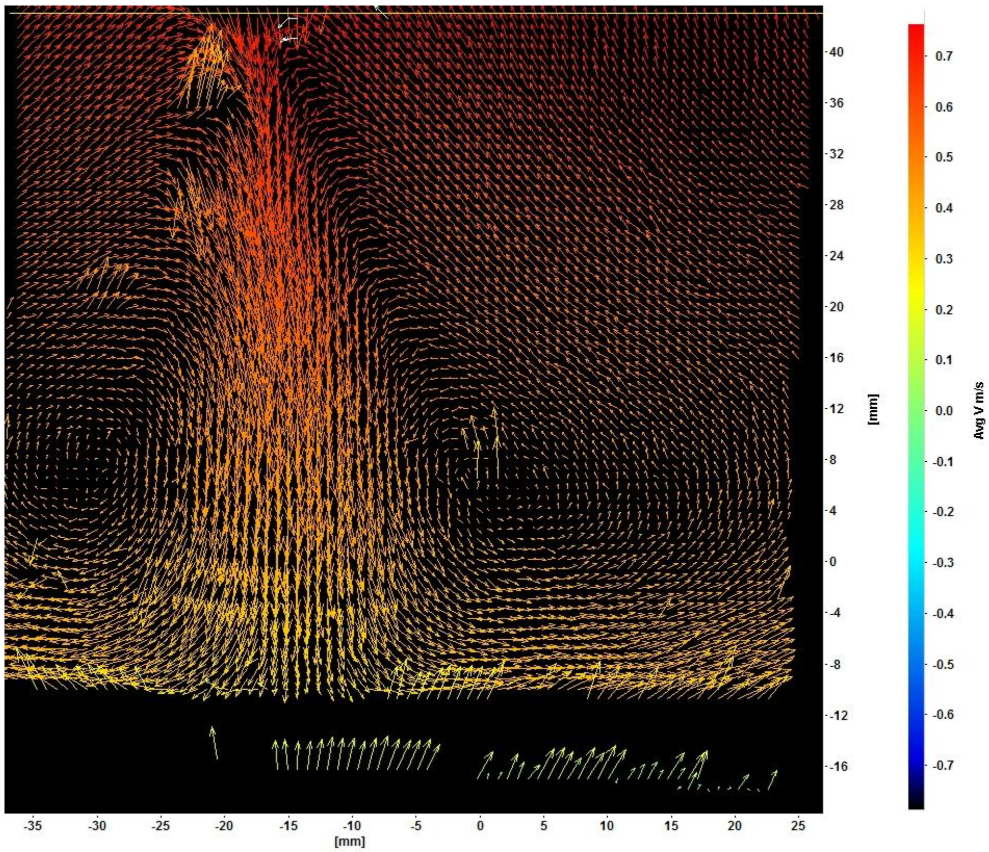


***Figure 4.6:*** *PIV image of 74 $\mu$ (500 RPM)*

### 4.2.2.1 Velocity profiles of the impeller stream at different radial locations

Figure 4.12 shows the radial velocity component in the impeller stream normalized with the impeller tip velocity versus normalized radial distance for 18 micron tracer particles. It can inferred that the impeller jet is not symmetric about the impeller mid-plane (z=0). This is because of the gravitational force tends to drag the closer to the bottom of the vessel. At distances closer to the impeller tip than the wall, the impeller jet is very dynamic and has a high velocity over a narrow range of axial distance. For example between z/H=0 to z/H=0.33, impeller stream has the highest radial velocity at r/R=0.4. As one moves closer to the wall (r/R=0.64, 0.74, 0.84) the jet settles and exhibit self-similar axial profile.

As the jet spreads out the velocity with increasing radial distance, the velocity towards each end increases. As such the radial velocity at r/R=0.64, 0.74, 0.84 is greater than the others at the same axial distance towards the end of the jet on each side.

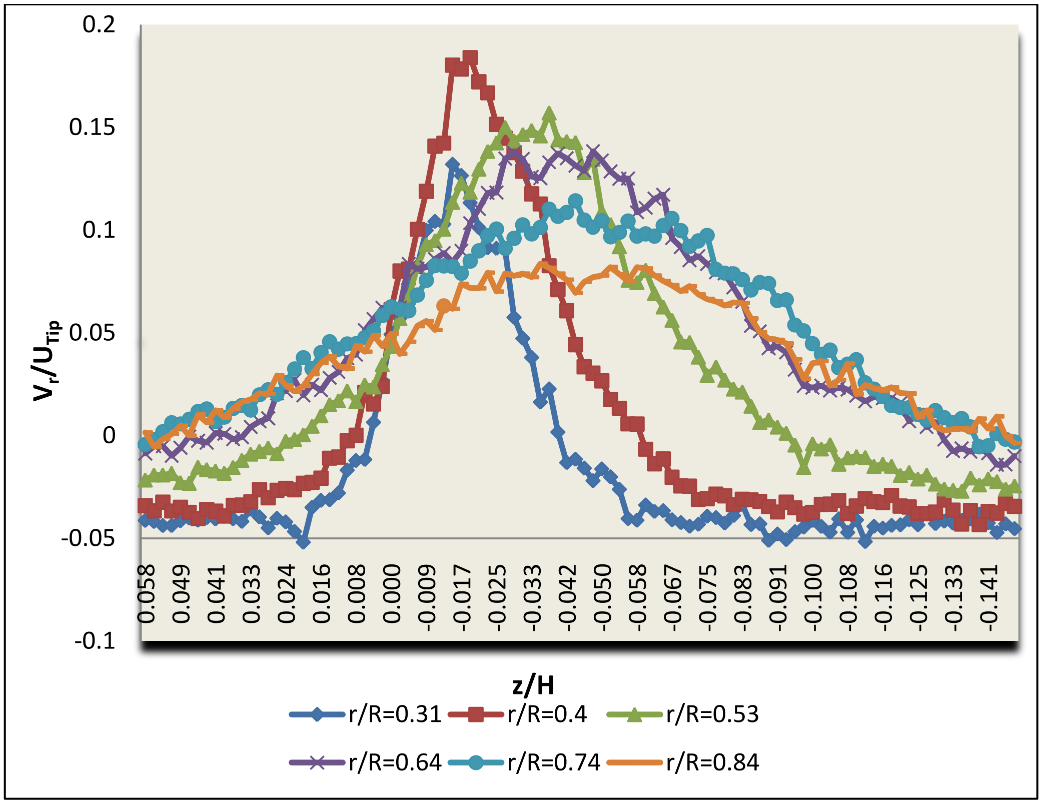


***Figure 4.7****: Normalized radial velocity at different axial distances*

#### 4.2.2.2 Thin Film Effect

If the radial velocity profiles at layers very close to the wall are compared, the effect of thin film can be observed. Figure 4.8 the velocities of 18 micron tracer particles at layers close to the wall at different axial locations in the impeller stream.. It can be noticed that as one moves closer to the wall the velocity difference increases. This is due to the thin film present just in front of the wall which retards the motion of the solids trying to penetrate it.

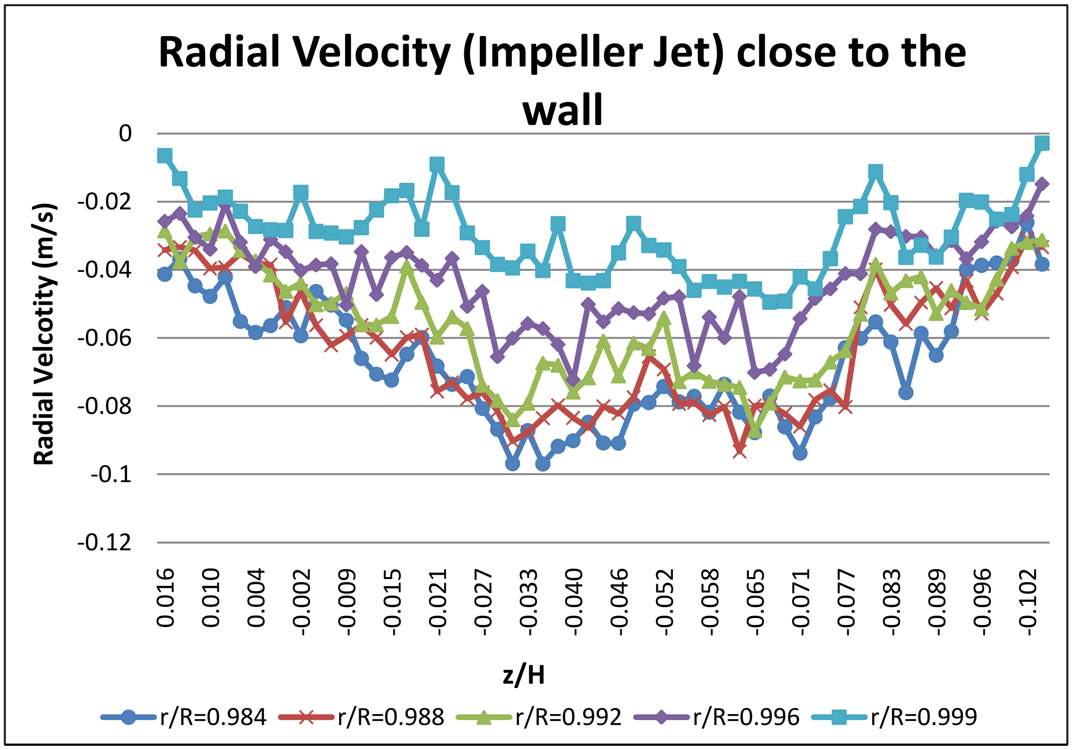


***Figure 4.8***: *Declaration of the solids particles due to the presence of thin film*

#### 4.4.2.3 Impact velocities

Radial, tangential and axial velocities at r/R =0.992, 0.996, 0.999 , across the entire axial distance captured by the cameras are shown in the Figures 4.8, 4.9 and 4.11 below for 74 micron particle with density 2500kg/m$^3$. Region I & III is the part of upper and lower circulation loop respectively while region II represents the impeller stream. It should be noted that Region II is the source of fluid for the fluid layer near the wall (Wall Jet) in Region I & III. In Figure 13, radial velocity profiles at r/R=0.992 & r/R=0.996 approximately follow each other; but the velocity profile at r/R=0.999 is distinct with more peaks pointing towards the positive direction. Peaks pointing towards the positive directions in region II indicate that the particles have hit the wall and have changed their direction.

The changes in velocities are the result of energy and momentum transfer at the walls. In region II, the velocity at the layer r/R=0.996 can be approximated as the normal impact velocity and the velocity at the layer r/R=0.999 can be approximated as the rebound velocity. In region I, the velocity decreases from layer at r/R=0.999 to the subsequent layers because the particles after leaving the wall starts mixing with the bulk fluid which leads to reduction in the radial velocity.

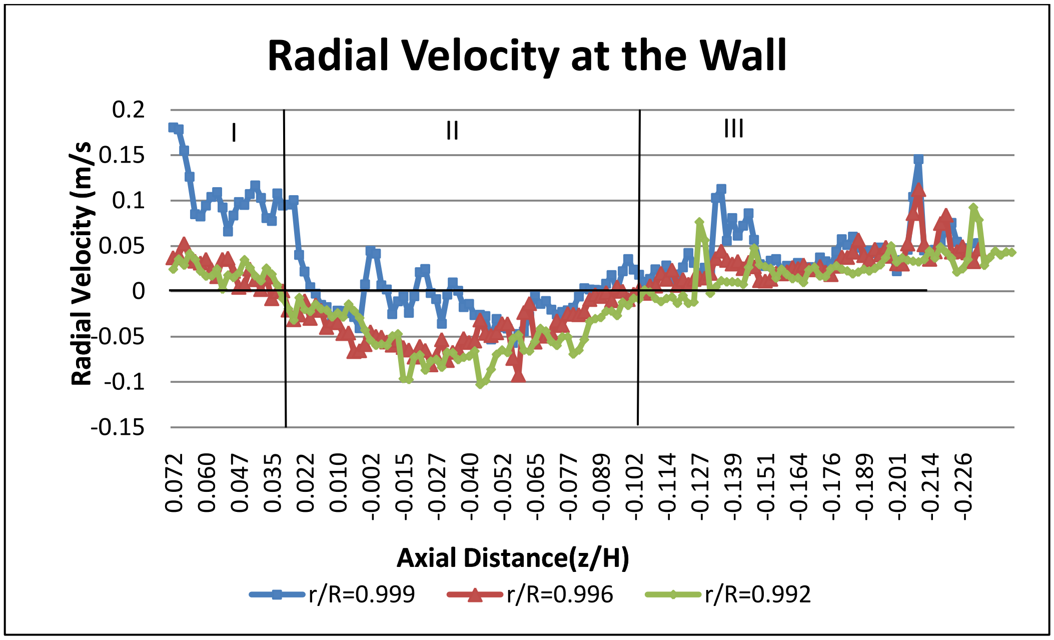


***Figure 4.8***: *Radial velocity at the wall*

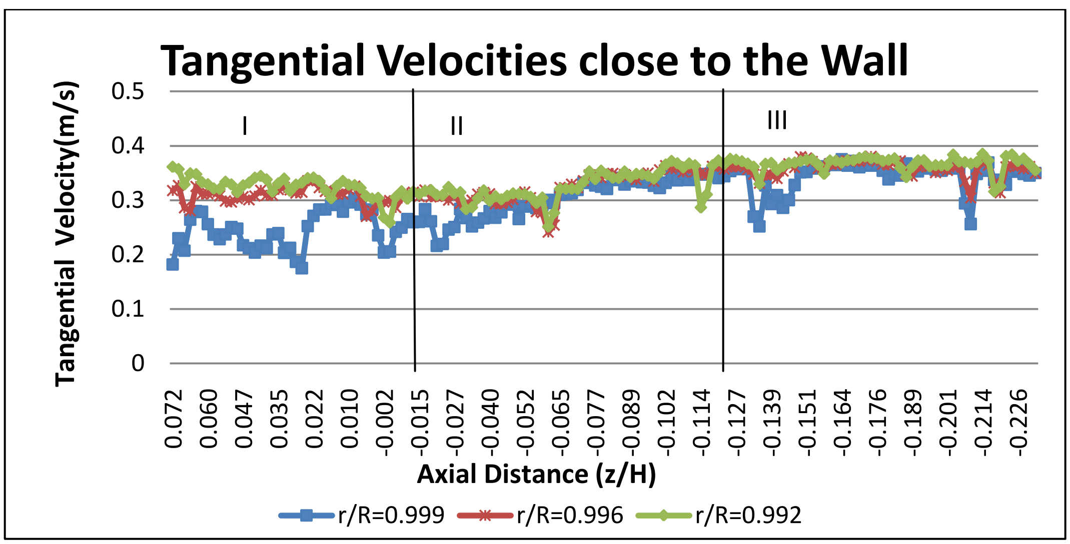


***Figure 4.9***: *Tangential Velocity at the wall*

The tangential velocities are relatively much higher than the radial and axial velocities. This suggests that there can be significantly high abrasive wear. The tangential velocities closely matches in the layers at r/R=0.992 and r/R=0.996 closely matches with each other while at the layer closest to the wall (r/R=0.999), the velocities are less than the other two layers. This can be attributed to the presence of a boundary layer just in front of the wall.

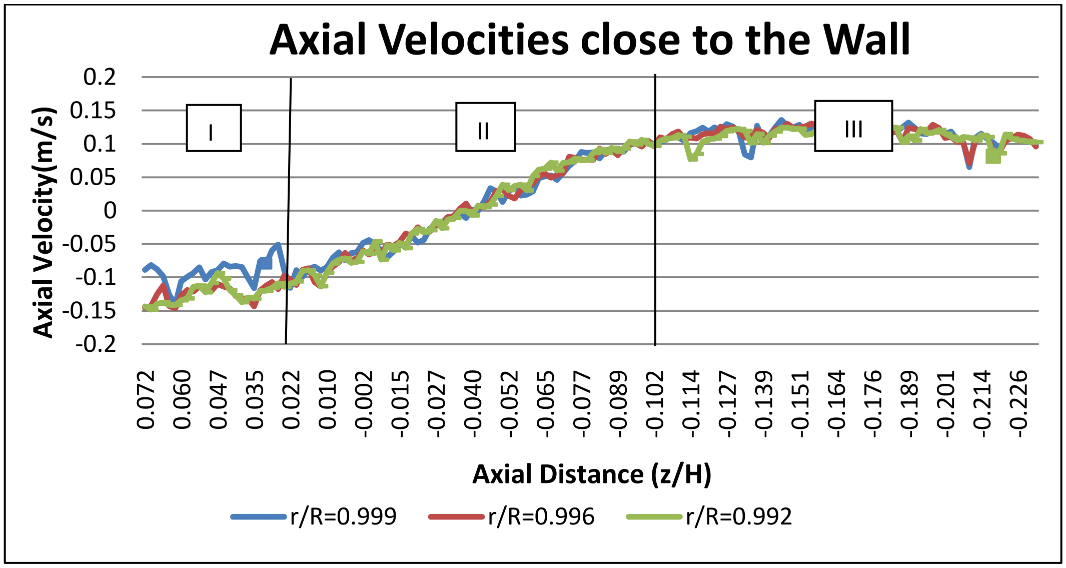


***Figure 4.11****: Axial Velocity at the wall*

The axial velocity profile at all three layers approximately matches with each other. After the impingement of the impeller jet on the wall, the jet splits into two one move towards the open end of the vessel and the other moves towards the bottom. This is the reason that the axial velocity moves from negative to positive direction while crossing zero in the middle of region II.

### 4.2.2.4 Impact angle

Using the velocity information from the PIV results (74 micron tracer particle), it was possible to calculate the impact angles in impeller stream both $r-z$ plane. The axial and radial velocities in the layer at r/R=0.996 were divided to get the impact angles in $r-z$. In Figure 4.12, it can be observed that the incident angle crosses the $\theta = 0$ once in the impeller stream and three times over all. The Figure illustrates the reason.

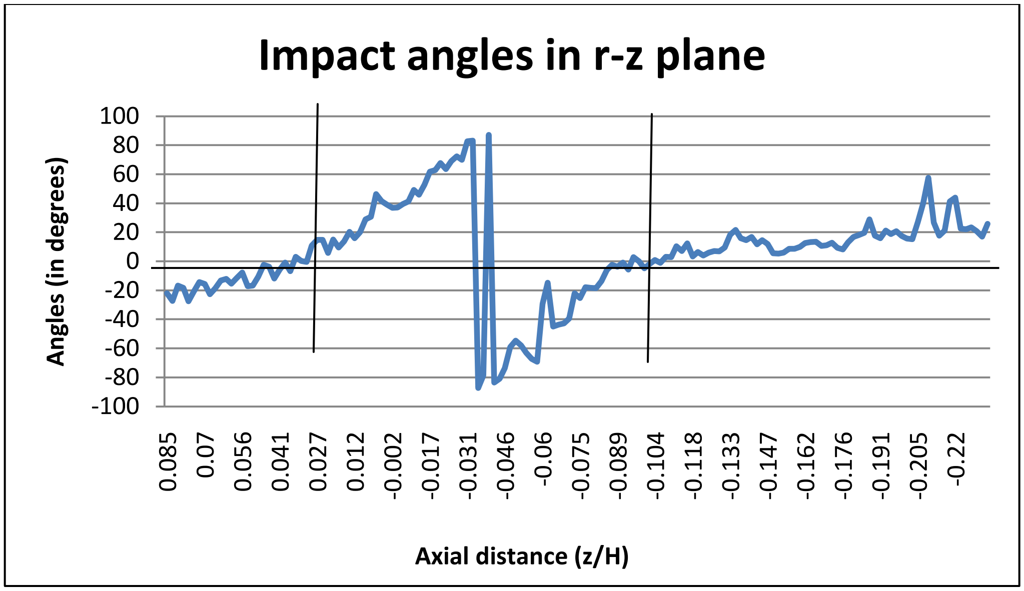


***Figure 4.12****: Impact angles in* $r-z$ *plane*

Since the impact angle is greatest at the impeller mid-plane and decreases as one moves away from it, it can be inferred that deformation type wear is greatest at the wall in region II. The cutting action becomes dominant as the impeller stream enters the two circulatory zones. In $r-\theta$ plane the impact angle at the walls is calculated by dividing the radial velocity by the tangential velocity of the particle. Figure 4.13 shows the impact angle in $r-\theta$ plane at various axial distances.

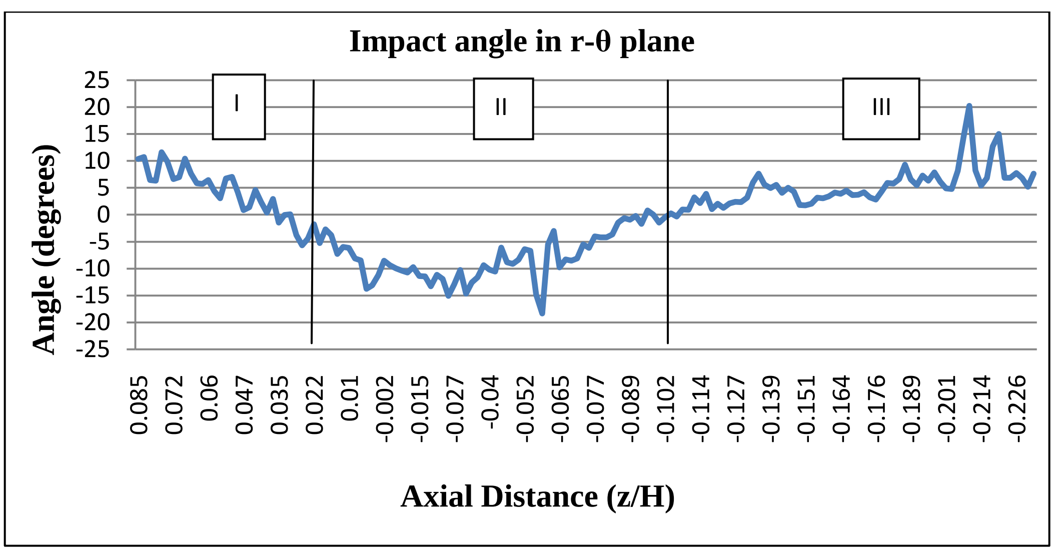


***Figure 4.13****: Impact and in* $r-\theta$ *plane*

It can be inferred from Figure 4.17 that in attack angles are shallow; hence, cutting action is dominant. The impact velocity and the impact angles can be utilized to find the amount of material removed.

Figure 4.14 and figure 4.15 was obtained while comparing the Platzer's [1] fluid flow model and the PIV results at two different radial distances.

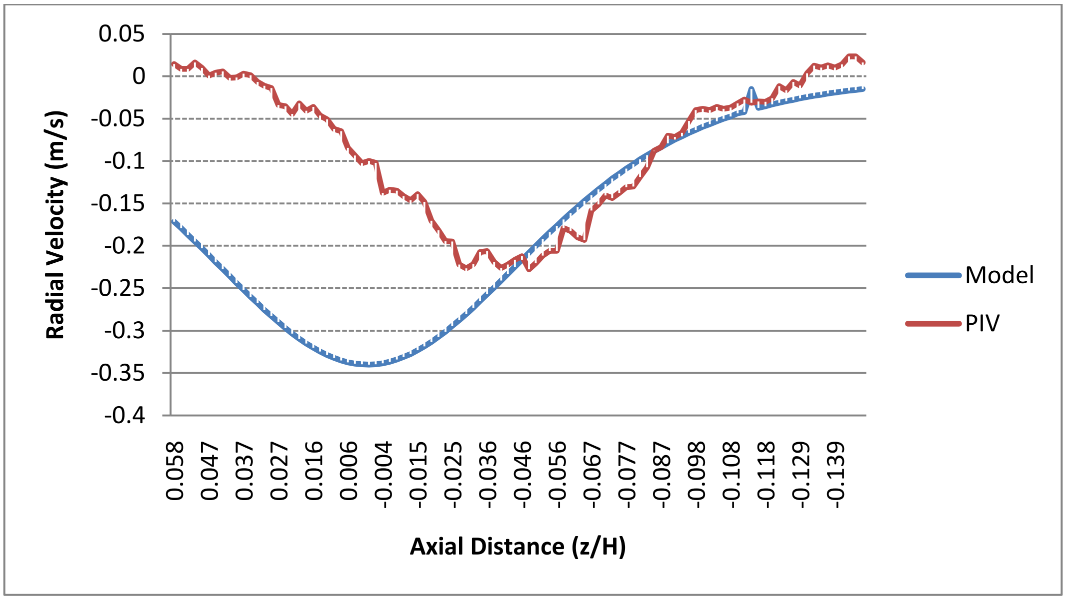


***Figure 4.14****: Radial velocity predicted by model (blue) and PIV (red) at r/R=0.64*

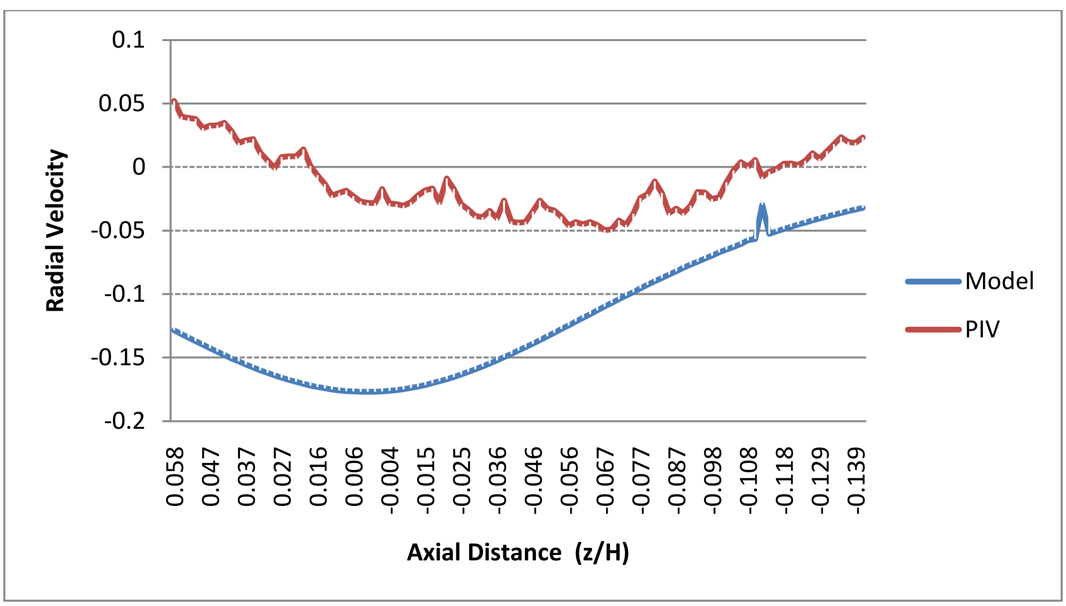


***Figure 4.15****: Radial velocity predicted by model (blue) and PIV (red) at r/R=0.99*

It can be observed that the model over predicts the velocity. This may be possible because the model assumes a straight impeller jet axis parallel to the bottom of the vessel but as noted by PIV experiment impeller jet axis inclines towards the bottom of the vessel. The possible explanations for the inclination of the axis are: a) the wall at the bottom stifles the fluid entrainment; b) the volume of the lower circulation loop is less than that of the upper one hence, the fluid in the upper circulation loop pushes the impeller jet fluid. Further investigation is required to explain the difference in prediction from the model and PIV result.

## 4.3 Wear Measurements

One approach to measure erosion damage is the multi-layer paint scheme [6]. The technique presents a way to produce highly visible and accelerated erosion damage. The multilayer paints well represent materials which show mixed ductile-brittle erosion characteristics such as mild steel, titanium because the multilayer paints exhibit similar properties [6]. In the technique different colors of are sprayed onto the test material and the typical thickness of each layers is 0.7 mm. In case of mixing vessels, rectangular metals sheet made of mild steel can be used as substrate. After applying the paints of uniform thickness, the sheet metal can be curved to make the cylinders with diameter equal to the internal diameter of the mixing vessel (Figure 4.16).

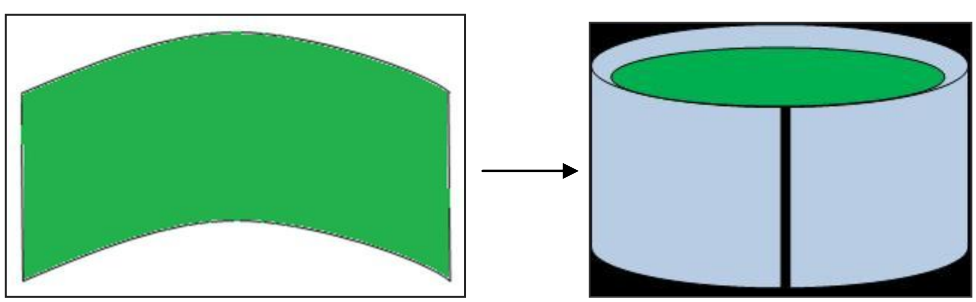

Sheet metal with multilayer paints        Cylindrical sheet metal to fit the vessel

***Figure 4.16**: Multilayer paints applied to sheet metal*

A very preliminary qualitative test was conducted to observe the nature of erosion. To this end, thin galvanized steel sheets (59×25 cm) were sand blasted to prepare the surface suitable for adhesion. The sheets were then rolled into cylinders. Using enamel spray paint six layers of paint were applied. The base color was grey premier followed by blue, green, yellow, red, and black. Each paint layer was left to dry for five hours approximately. The thickness of the paints were approximately 0.7 mm. Figure 4.20 shows the finally painted cylindrical metal sheet.

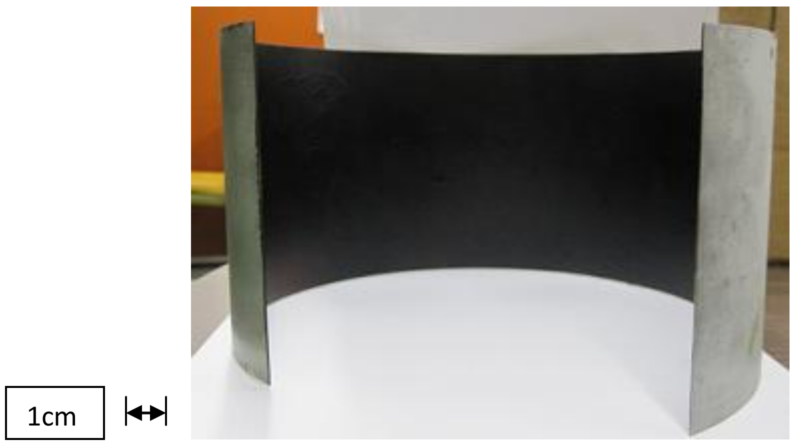


***Figure 4.17****: Color applied on cylindrical sheet metal*

Mixing vessel and impeller of different size from that used in PIV experiment but of same dimensional ratio was used to emulate the mixing environment. The diameter (D) of the vessel was 9 inches and that of the impeller (d) was 3 inches. (d=D/3). The off bottom clearance (C) was 3 inches (C=D/3). Sillica particles of size 40-50 US mesh size was added to 4 litres water. For the initial trail, one of the painted metal sheet was immersed in vessel with the concentration of the sand particles being 7.5 percent by weight and the impeller speed being 900 RPM. Figure 4.18 shows the photograph taken after 30 minutes of operation. It can be noticed that at some places the black paint has eroded and the red paint appears on the surface. Appearance of the second (red) layer confirms the occurrence of abrasive wear due to the tangential motion of the solids near the wall.

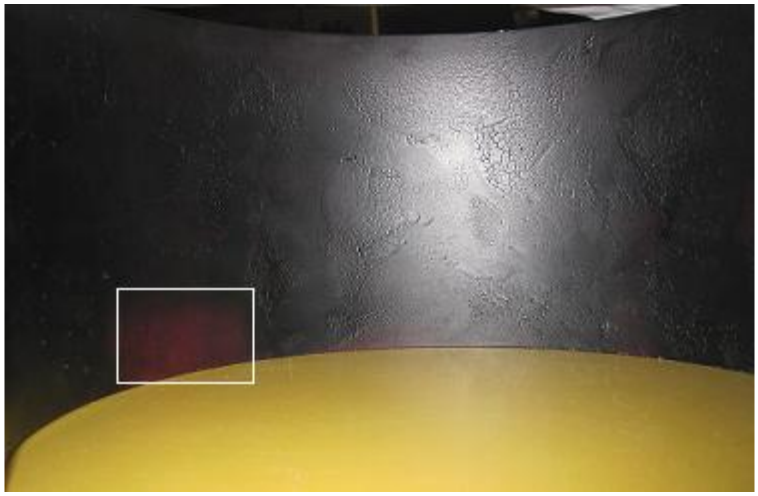


***Figure 4.18****: Painted metal sheet after 30 minutes of operation*

Using the second painted metal sheet and the particle concentration of 10 percent, the impeller was run at 1800 RPM and photographs were taken after each 1 hour. Figure 4.19 (a) shows the photograph taken just after first hour of operation. Abrasion due to tangential motion has eroded the black layer. Figure 4.19 (b) shows the photograph of taken after second hour. Apart from the surface turning slightly reddish, the individual impact events are encircled. The direction of the arrow approximately indicates the direction of impact. Due to the impact, the material (black paint in this case) has been scoped out to form small hillocks type shape. If the approximate shape and size of these hillocks can be estimated, then it is possible to calculate the material loss.


***Figure 4.19 (a****): Surface of the painted metal sheet after one hour of operation*

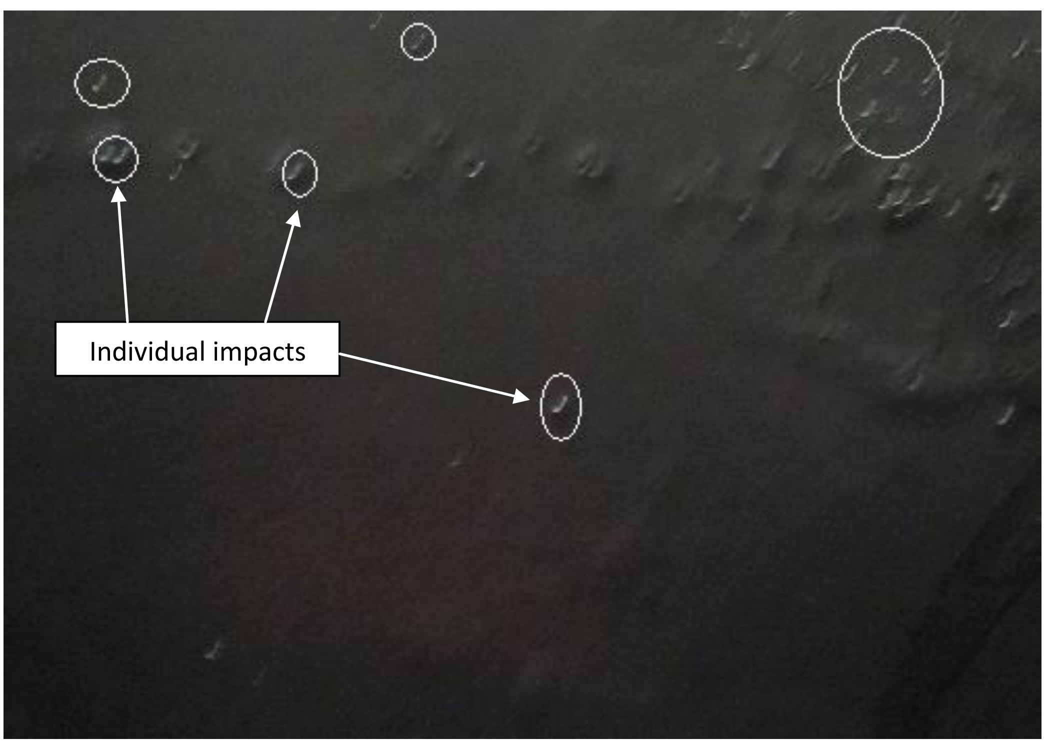


***Figure 4.19 (b):*** *Surface of the painted sheet metal after 2 hours*

Figure 4.19 (c) shows a different section of the metal plate after 2 hours of operation. The erosion is more obvious in this particular section with the yellow layer being exposed. As show in the figure, the impact direction can be decomposed in axial and tangential direction. The tangential pattern of the eroded paint suggests that tangential velocity is greater than the axial velocity. PIV results confirm the interpretation.

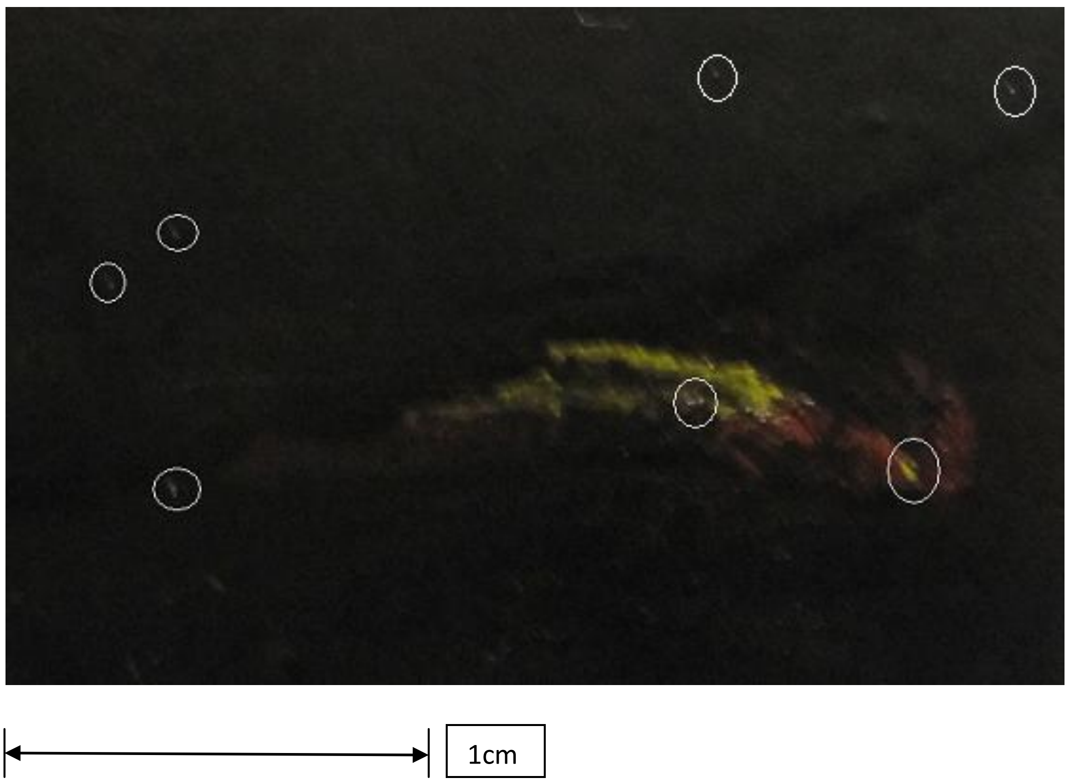


***Figure 4.19 (c):*** *Surface from another section of the painted sheet metal after 2 hours*

Figure 4.19 (d) shows the paint layer after 3 hours. The erosion has been so severe that at some places there is almost not any black layer left. Thus, due to the damage accumulation over three hours the black layer totally eroded from some regions. If the impact angles and impact velocities of the particle are know it is possible to calculate the total damage accumulation by using equation 4.32.

The centre of the wear pattern and impeller mid-plane are approximately at the same level. Hence, the maximum erosion was observed in the impeller jet region.

The wear pattern was localised and not evenly distributed. This can be due to the following possible reasons:

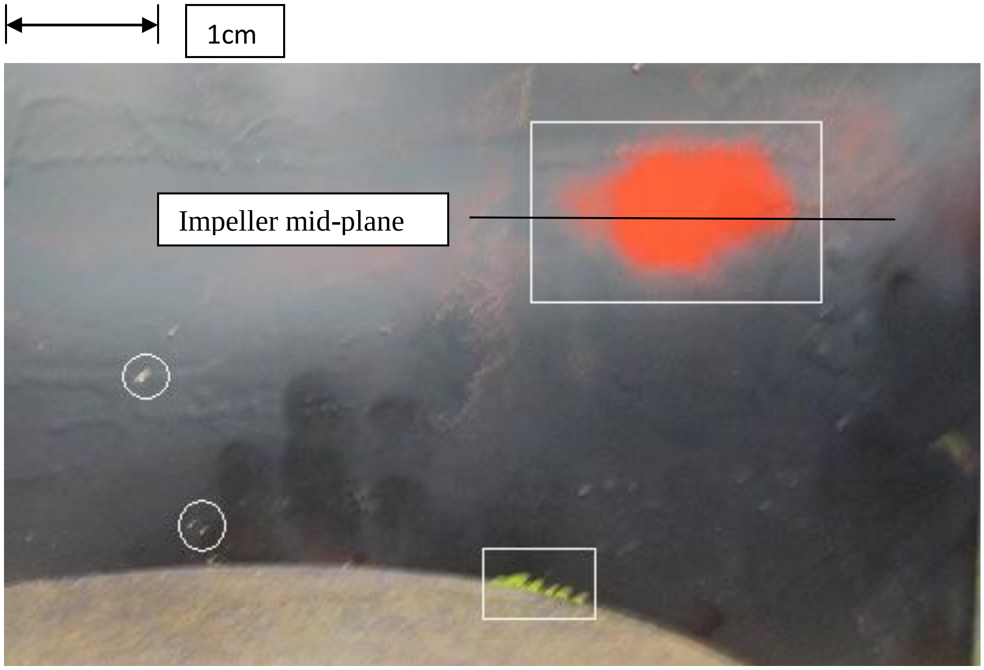


***Figure 4.19 (d):*** *Surface from another section of the painted sheet metal after 3 hours*

1) Since the metal sheet was not a closed cylinder, one of the free ends did not properly stick to the wall. Hence, it was little closer to the impeller than rest of the metal sheet and suffered the maximum damage. This can also lead to the conclusion that if the walls were closer to the impeller (d>D/3), then severity of erosion increases.

2) The paint layer in this region was not as thick as other regions and therefore it eroded quickly than the other regions.

## 4.6 Discussion

From modeling to date, there are a number of observability issues in measuring all of the variables in the damage model. Some understanding of the nature of the particle impingement is needed to determine g($\theta$) and E(90) at different locations.

By understanding the nature of the flows and the particle and material properties, it would be possible to design tests to emulate those process conditions and thereby predict damage rates. Synergistic effects such as erosion-corrosion have not been considered.

For condition monitoring, it is sufficient to measure the material removal rate (or equivalently the change in geometry) at intervals of time short enough to prevent a catastrophic failure of the rotating components or pressure boundary. Particle impact events may be detected acoustically, with acoustic emissions used to determine when impacts exceed a damage threshold.

Now that a working physical model exists for wear in a cylindrical mixing tank, it is important to validate the phenomenological model of the combined process of flows and damage. Particle tacking techniques can employed for tracking the individual particles. Techniques such as laser profilometry, optical microscopy, scanning electron microscopy can be used to quantify the exact amount of material removed.  The next stage is to scale up to geometries and conditions that are applicable in industry. From there, the next logical step will be to take the results obtained from the mixing tank model, and apply them to other components, such as the impellers themselves and the internals centrifugal pumps.

# References

[1] B. Platzer and G. Noll, Modelling of the local distributions of velocity components and turbulence parameters in agitated vessels – Method and results, *Chem. Eng. Process.* 23 (1988), pp. 13–31

[2] H.M. Clark and L.C. Burmeister, The influence of squeeze film on particle impact velocities in erosion, *International Journal of Impact Engineering* **12** (3) (1992), pp. 415–426

[3] Y.I. Oka, K. Okamura and T. Yoshida, Practical estimation of erosion damage caused by solid particle impact. Part 1: effects of impact parameters on a predictive equation, *Wear* 259 (2005), pp. 95–101.

[4] Y.I. Oka and T. Yoshida, Practical estimation of erosion damage caused by solid particle impact. Part 2. Mechanical properties of material directly associated with erosion damage, *Wear* 259 (2005), pp. 102–109.

[5] M.C. Roco and G.R. Addie, Erosion wear in slurry pumps and pipes. *Powder Technol.* **50** (1987), p. 35.

[6] J. Wu, B. Nguyen, L. Graham, Y. Zhu, T. Kilpatrick and J. Davis, Minimizing impeller slurry wear through multilayer paint modeling, *Can. J. Chem. Eng.* **83**(5) (2005), pp. 835–842

**Chapter 5**

# Conclusions and Recommendations for Future Work

## 5.1 Summary

The study presented in the thesis had two related objectives: 1) determine the feasibility of using hyperspectral features of the ore and the process streams as an additional set of variable that would relate to processibility; 2) modeling wear damage in flotation cells. For the meeting the first objective, a set of flotation experiments were designed and conducted based on a standard protocol. Qualitative and quantitative evaluations of the ore and the froth were made based on visual observation and standard Dean Stark analysis respectively. Color of the froth (qualitative feature) correlated well with the processibility (based on quantitative analysis). The model based on hyperspectral features was able to predict the fines and bitumen content in the ores with reasonable accuracy. Two class classifications were devised on the oil sands based on the color of the froth. Using hyperspectral analysis, it was possible to isolate these two classes. Hence, it can be inferred that hyperspectral features relates to processibility and can be used for extracting timely information from the froth.

For meeting the second objective, a theoretical model was developed to estimate the damage. The model has three sub levels of modeling: 1) fluid flow in the vessel; 2) fluid-particle interaction model and; 3) particle-surface interaction model. In order to closely approximate the near wall particle-fluid and particle-surface phenomenon, the effect of thin film and kinetic energy lost at the surface was incorporated in the model. Standard reliability concept was eventually used to estimate the cumulative damage over a period of time. Particle Image Velocimetry technique was used determine the flow fields in the vessel. A set of PIV experiments was designed and conducted to this end. Analysis of the PIV results gave the information about impact angles and the impact velocities. The preliminary multi-layer paint wear test helped in understanding the wear pattern.

The specific contributions made are the following:

1) Proving that froth generated in the bitumen flotation process can be used to observe and control the process.

2) Developing erosion model for cylindrical mixing vessel using flow model and wear model which existed in literature.

3) Inclusion of the thin film effect in erosion to account for velocity reduction just in front of the wall

4) Development of damage model which relates to the total damage occurred over a period of time.

## 5.2 Future Work

Hyperspectral feature based analysis related well with color of the froth but the work has to be extended to relating the hyperspectral analysis to the processibility. This would help to develop froth based control of the flotation process. Detailed analysis of mineralogy is proceeding to determine how components that may adversely affect processibility may be observed as the extraction process is operating. Additionally, to be able to build more robust classification schemes and predictive models based on hyperspectral features, the technique must be tested out on many more samples of oil sands. Additional flotation experiments for repeatability. The temperature of the slurry in the vessel can also be varied to see the effect of change in temperature.

The empirical model developed for the flow field needs to be compared with PIV results for its accuracy. More advanced techniques which can determine the velocities of heavier particles and at high concentration can be employed to have a better understanding of the solid phase in liquid. Experiments on estimating the impacts frequency of the particles can be designed to complete the damage accumulation equation. Investigations can be carried on understanding exactly which impact events contribute to damage.  More quantitative experiments should be conducted to evaluate the material lost in the wear process to validate the damage model. If the results from the experiments conforms the model, the model development idea can be extended to more complex geometries such as pumps, chokes etc.

# APPENDIX

## A-1: Protocol for Flotation Experiment Using Denver Cell

1. Wear personal protective equipment; safety glasses, gloves and lab coat.

2. De-frost a bag of oil sand sample, note the I.D. on the work sheet.

3. With the agitator raised, turn on the agitation and adjust to 1500 rpm, then turn it off. Open the air line (bench valve) and the air stopcock on agitator. Adjust the flow meter to the desired rate (black ball at 80 = 150 ml/min). Then turn off the air stopcock on the agitator only.

4. Using the 1 litre flotation cell, add 300 gr of oil sand then 950 ml of tap water.

5. Place the prepared sample in the agitator. While holding the crank handle apply some pressure to release the locking mechanism on the other side. Carefully lower the agitator into the sample till the agitator comes to rest.

6. Put the first bread pan under the lip of the flotation cell.

7. Start agitation for 5 minutes (oil sand conditioning stage). Use the stopwatch. During this time, record the initial temperature. Do not collect any froth.

8. Turn on the air (stopcock on agitator); double check that the flow rate is correct.

9. Use a spatula to start collecting the bitumen froth floating on the slurry surface into a container (bread pan) for 3 minutes. Try not to drag too much water into the pan. Continue collecting the froth into a second pan for 2 minutes (5 minutes total). Finally, collect into a third pan for another 5 minutes (10 minutes total from initial aeration).

10. Turn off the aeration and agitation. Place the 3 collected froth containers aside for assay (Dean Stark analysis). Record the final temperature and pH of the tailings.

11. Holding the locking mechanism out, raise the flotation cell to its maximum height and re-lock in place. Transfer the flotation tailings to a 1 litre graduated cylinder and set aside for settling (for Zeta Potential Analysis). After 30 minutes, use a pipette to draw 10 ml of the tailings water for Zeta Potential Analysis. Also, fill two 50 ml centrifuge tubes with the tailings water and centrifuge at 10,000 g for 10 minutes. Set this clarified (process water) aside to use for Zeta Potential Analysis of the froth and tailings.

12. Re-mount the cell under the agitator. Lower the shaft part way into the cell and wash with tap water. Raise it again and pour the wash water and remaining tailings into the waste pail. Re-mount the cell and lower the agitator to the bottom.

13. Put toluene into the cell, turn on the agitation for a few minutes to remove and wash away any bitumen stuck on the shaft, inside the rotator and on the cell. Raise the agitator and pour waste Toluene into an organics only waste container.

14. Proceed to Dean Stark apparatus to conduct assay.

# A-2: Assembly Parts for Flotation Test Set-up

| | Assembly | Parts | Quantity | Part number | Supplier |
|---|---|---|---|---|---|
| | | | | | |
| 1) | Air flow connections | fitting | 1 | B-400-1-4 | Edmonton valve &fittings( Local) |
| | | Neddle valve | 1 | B-2/4JNA1 | Edmonton valve &fittings( Local) |
| | | Insert | 4 | B-405-170 | Edmonton valve &fittings( Local) |
| | | Adapters | 2 | B-400-1-2 | |
| | | | | | |
| 2) | Air regulator | | 1 | R-364-02C | Gregg distributors (Local) |
| | | | | | |
| 3) | Pressure Gauge | | 1 | 9484043 | Gregg distributors (Local) |
| | | | | | |
| 4) | Direct read rotameter | | 1 | FLDA3324C | Omega (US) |
| | | | | | |
| 5) | Water Bath | Heater Hose | 20 feet | 65015 | Gregg distributors (local) |
| | | Hose bar | 4 | 126-5B | Gregg distributors (local) |
| | | | 4 | 125-5B | Gregg distributors (local) |

# A-3: Drawing of the Mixing System for Particle Image Velocimetry Experiments

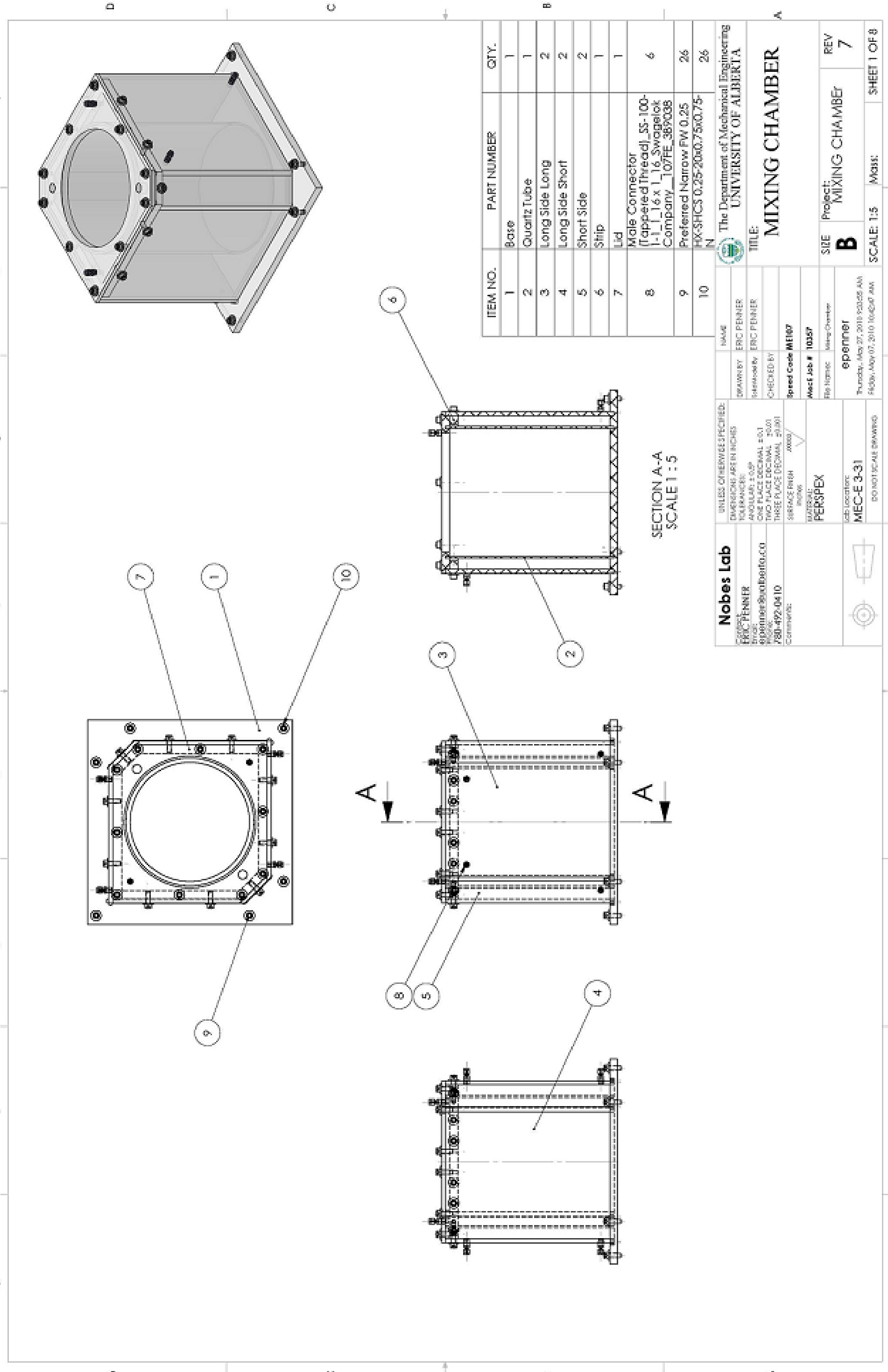


***Figure A3-1**: Mixing Chamber*

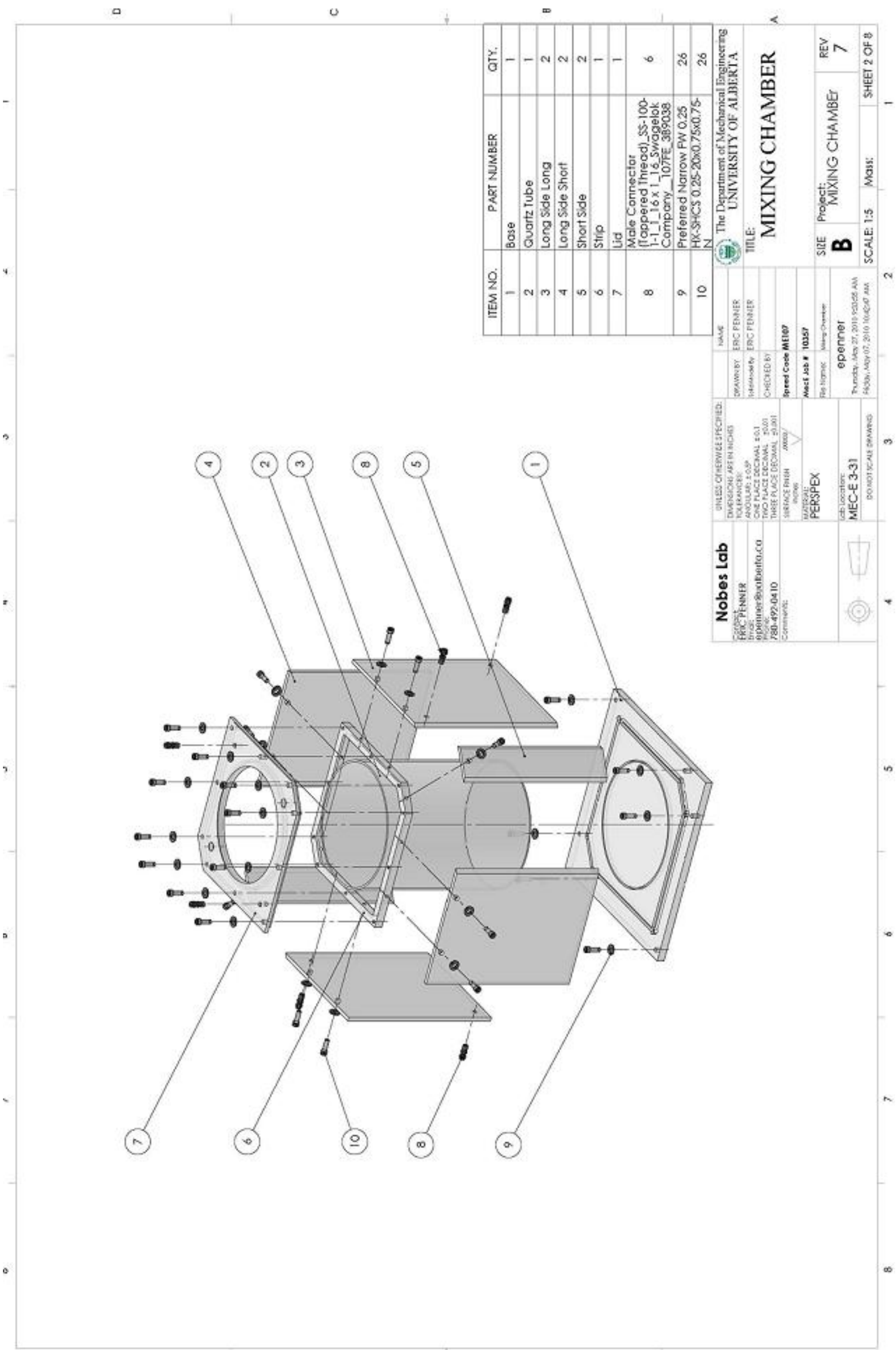


***Figure A3-2****: Exploded View of Mixing Chamber*

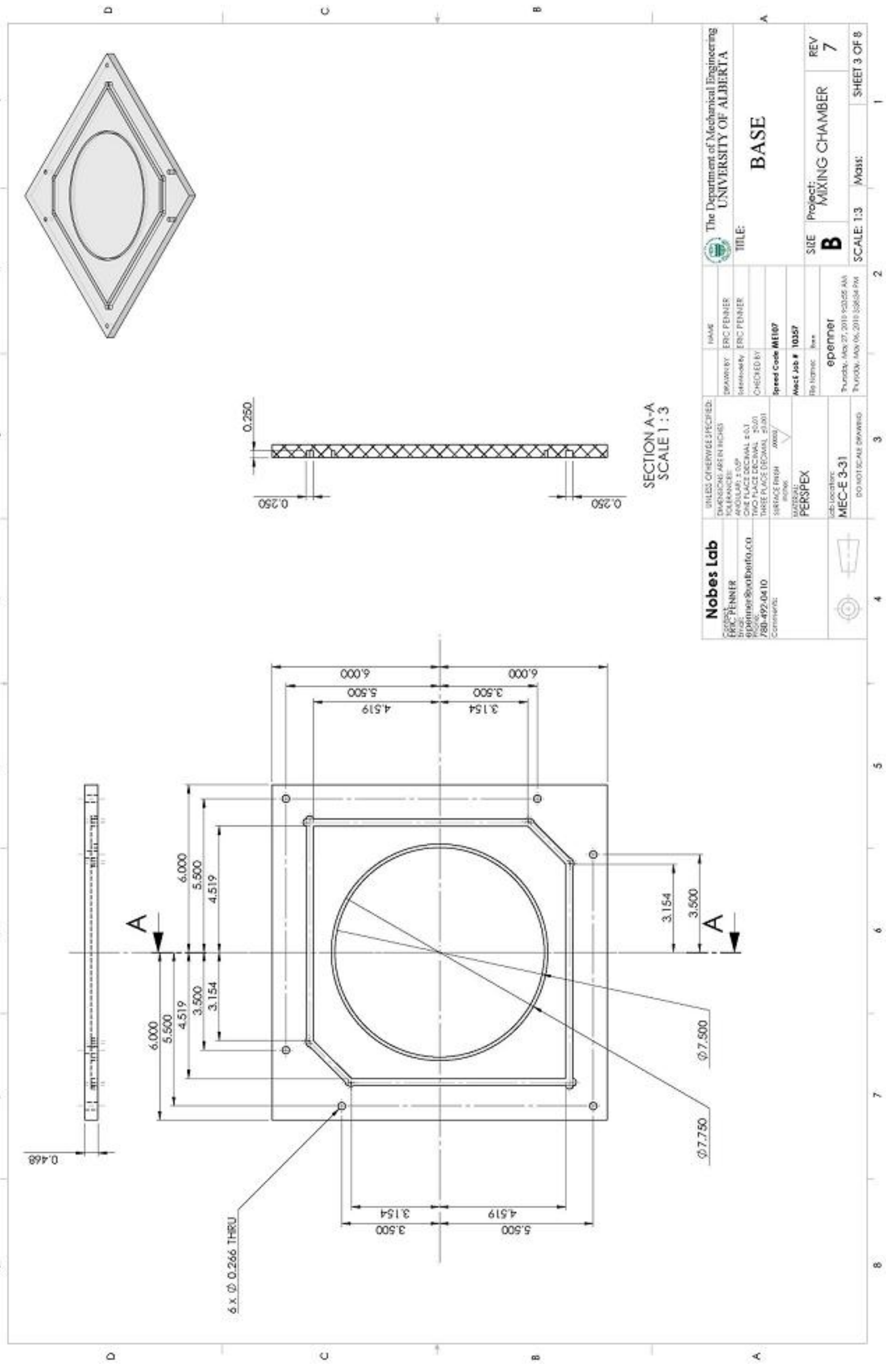


***Figure A3-3**: Base of the Mixing Chamber*

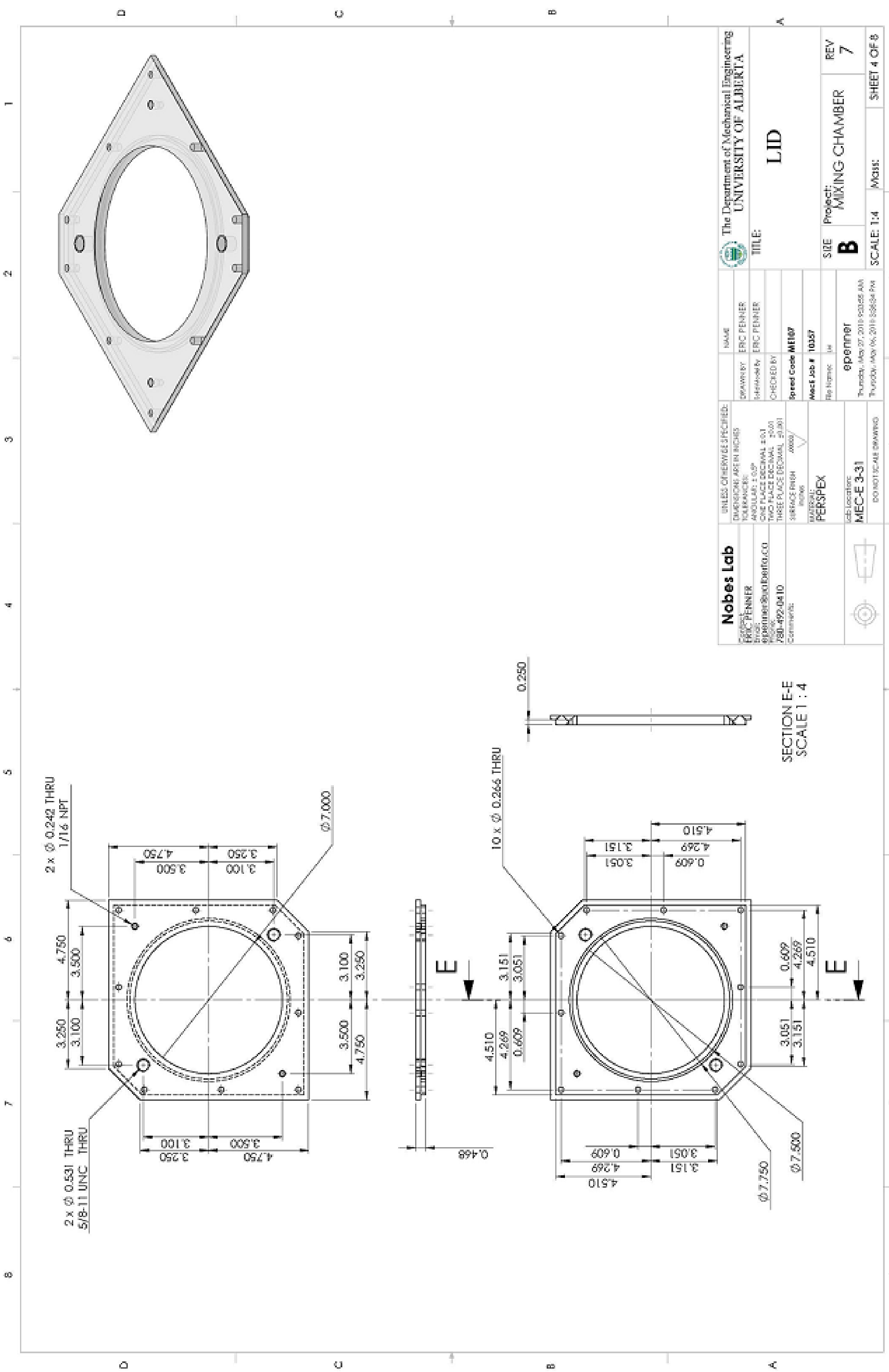


***Figure A3-4**: Lid of the Mixing Chamber*

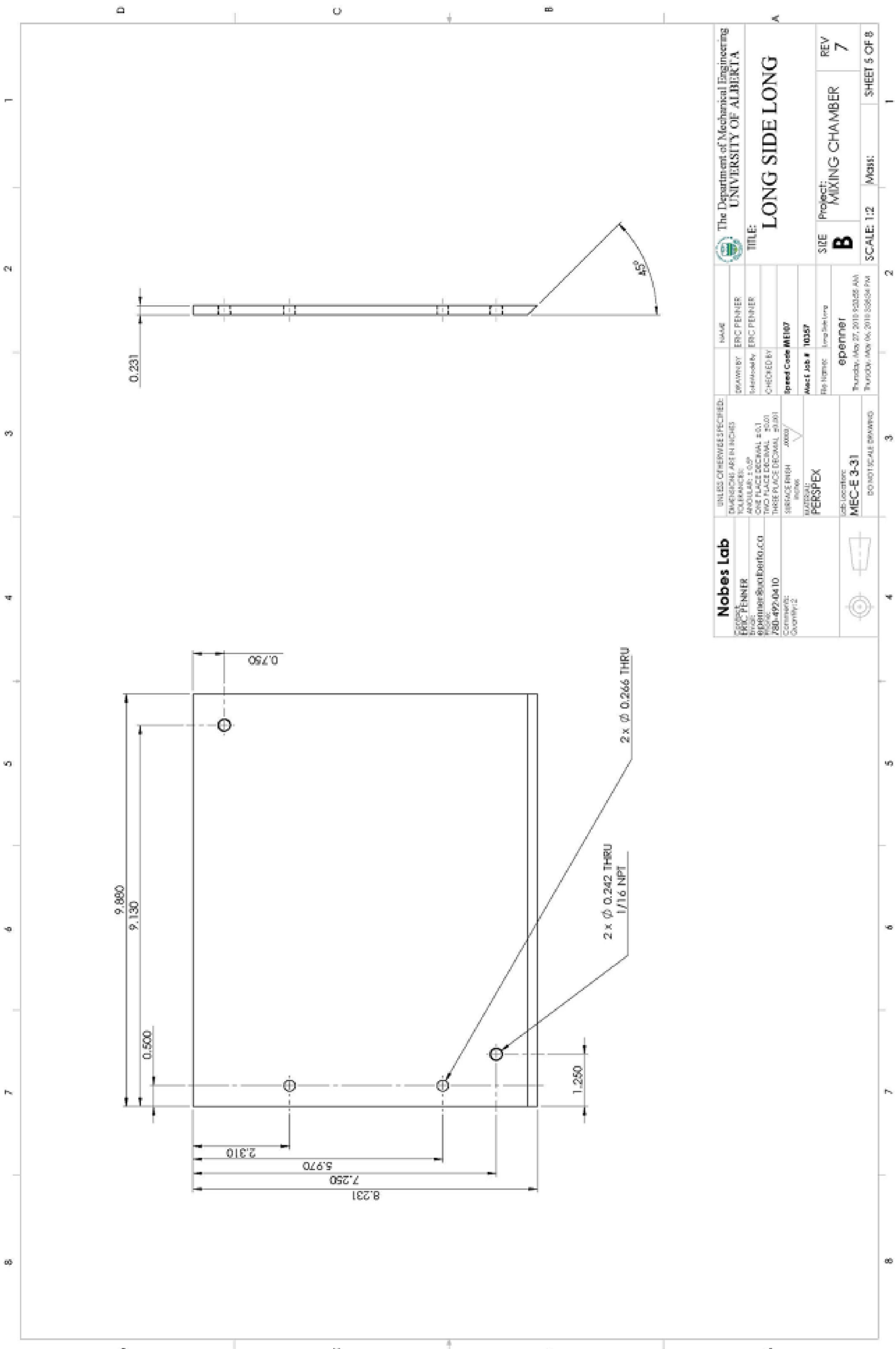


***Figure A3-5****: Long side Long*

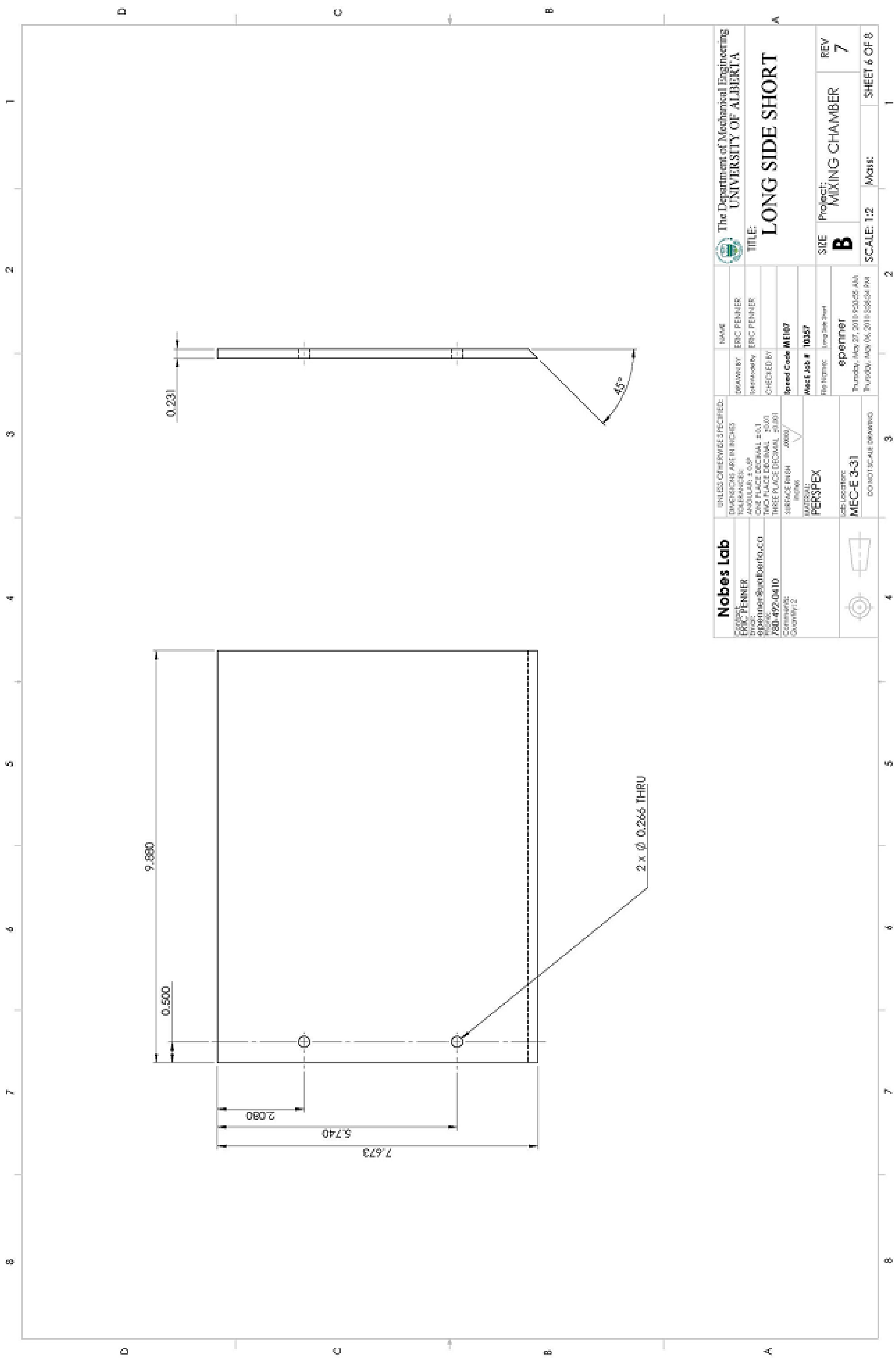


***Figure A3-6:*** Long Side Short

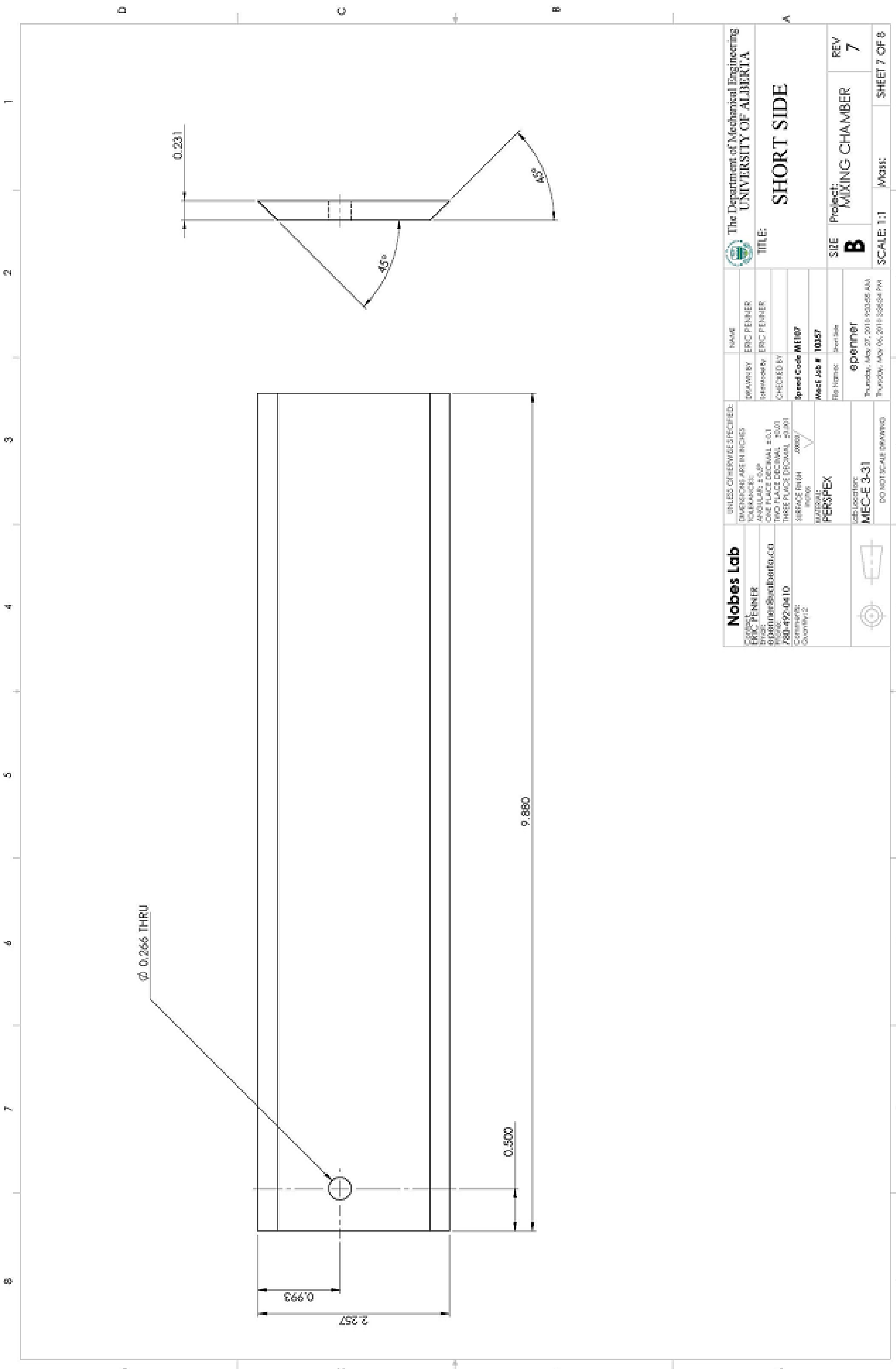


***Figure A3-7:*** Short Side

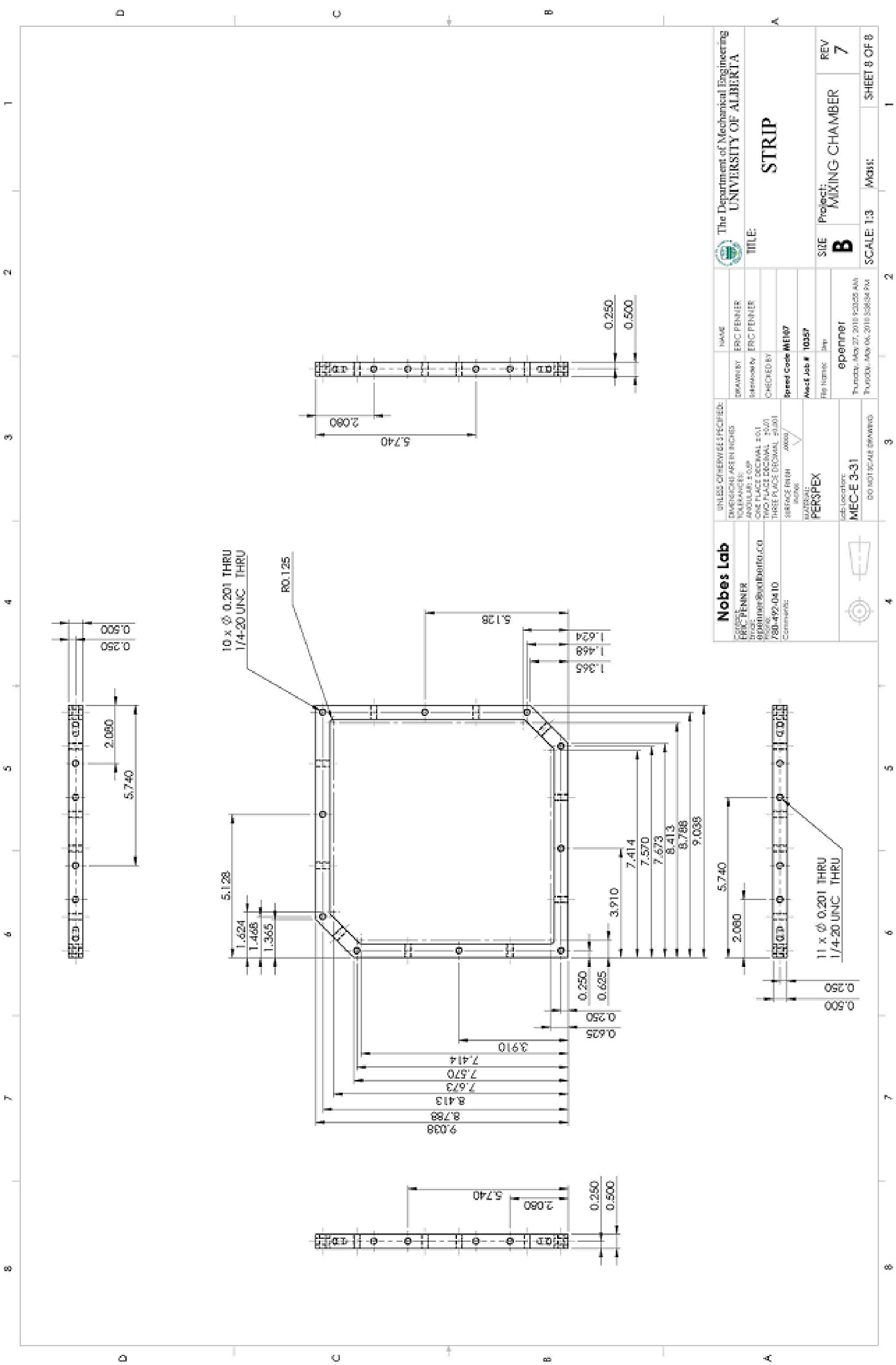


*Figure A3-8:* Strip

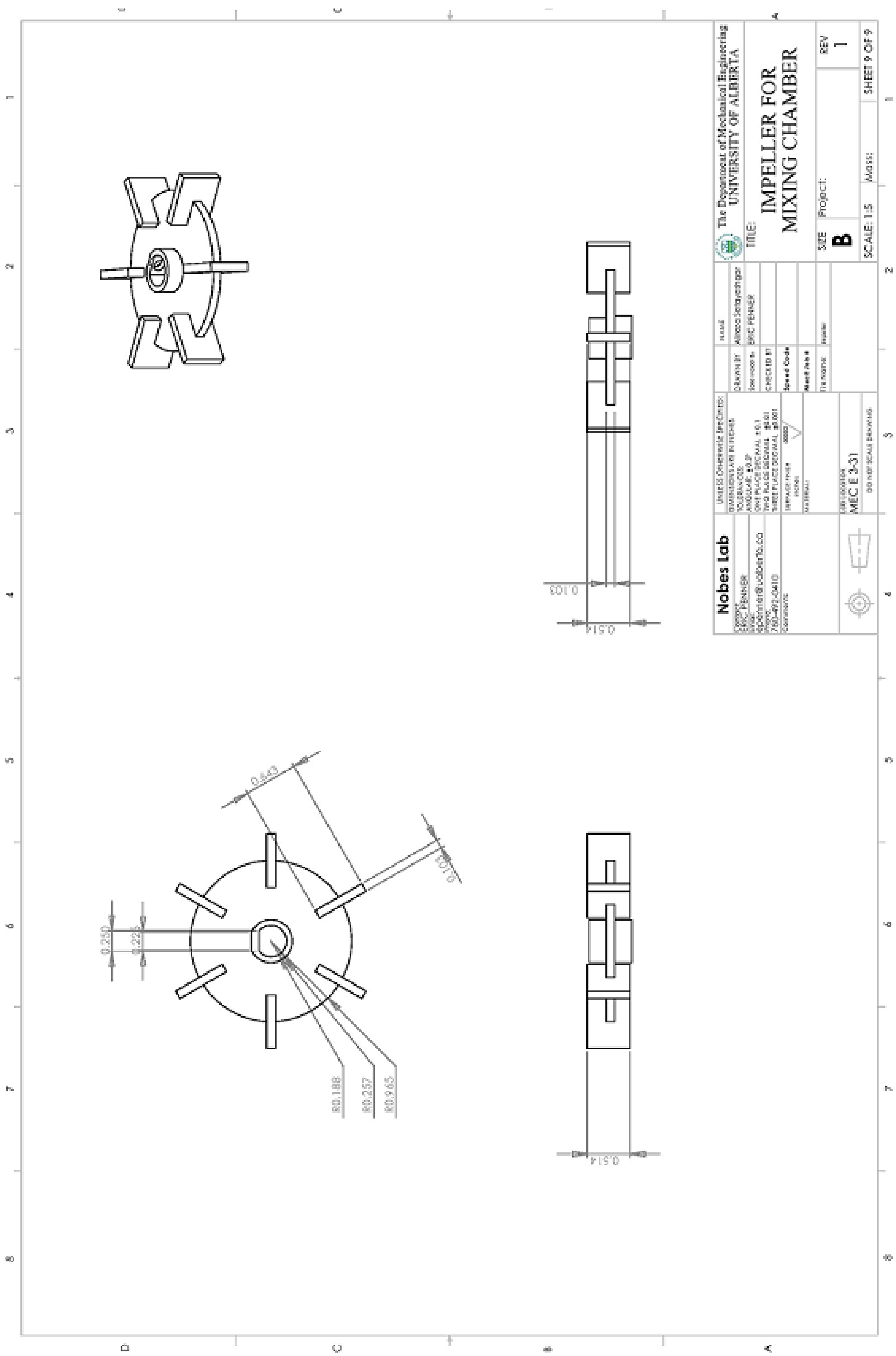


***Figure A3-9:*** Impeller

## A-4: Specifications of Laser and Camera Used for Experiments

Table A4-1 gives the specifications of Solo PIV 120 Laser system (Nd: YAG) used in the experiment

***Table A4-1:*** Specification of laser

| Feature | | Value |
|---|---|---|
| Repetition Rate (Hz) | | 15 |
| Energy[1] (mJ) | 532 nm[5] | 120 |
| | 355 nm[5] | 35 |
| | 266 nm[5] | 25 |
| Energy Stability[2] (± %) | 532 nm[5] | 4 |
| | 355 nm[5] | 7 |
| | 266 nm[5] | 9 |
| Beam Diameter (mm) | | 4.5 |
| Pulse Width[3] (ns) | | 3-5 |
| Divergence[4] (mrad) | | <2 |
| Beam Pointing Stability (urad) | | <100 |

The superscripts 1, 2, 3, 4, and 5 used in the table are explained below:

1-Optical losses due to optional attenuator will reduce maximum energy by 10%

2- Pulse-to-pulse for 98% of shots after 30 minute warm up

3- Full width half maximum

4- Full angle for 86% of the energy, at 1/e2 point

5- For single-head operation. Only one laser head may be optimized for 355 nm.

Table A4-2 gives the specification of the LaVision Imager Intense Camera used in the experiment

***Table A4-2:*** *Specification of the LaVision Imager Intense camera used*

| **Exposure time** | **Number of pixels** | **Pixel size** | **Sensor format** | **Spectral response** | **Maximum QE** |
|---|---|---|---|---|---|
| 500 ns to 1000 s | 1376 × 1040 | 6.45µm× 6.45µm | 2/3" | 280 nm to 1000 nm | 65% @ 500 nm |
| **CCD temperature** | **Dynamic range** | **Scan rate** | **Readout frequency** | **Readout noise** | **CCD quality** |
| -12°C | 12 bit | 16 MHz | 10 frame/s | 4 e- to 5 e- @ 16 MHz | Grade 0 |

# A-5 Permission to reproduce

E-mail of the permission:

"Good afternoon Vivek,

I've heard back from our team, and we are happy to provide you with permission to use the image. Please credit the image to "Alberta Innovates – Technology Futures."

Kind regards,
Allan

**Allan Tesorio | Communications Officer**
Communications
Alberta Innovates - Technology Futures
250 Karl Clark Road | Edmonton | AB | T6N 1E4
780 450 5555 o
780 901 9754 c
allan.tesorio@albertainnovates.ca
www.albertainnovates.ca

**From:** Doug Lillico
**Sent:** Monday, March 14, 2011 12:31 PM
**To:** Allan Tesorio
**Cc:** Yvonne Mariacci
**Subject:** RE: Seeking Permission to reproduce a diagram

No problem – with attribution

**From:** Allan Tesorio
**Sent:** March 14, 2011 12:01 PM
**To:** Doug Lillico
**Cc:** Yvonne Mariacci
**Subject:** FW: Seeking Permission to reproduce a diagram

Good morning Doug,

I've received an email from a student seeking permission to use a diagram from the ARC (image attached, link is currently at http://www.globaloilsands.com/Processing/index.shtml). He would like to use as part of his thesis explaining the bitumen process. I'm not entirely sure who owns the image, but credit would have to be given to us, with the "Used with Permission" disclaimer.

Please let me know your thoughts.

Regards,
Allan

**Allan Tesorio | Communications Officer**
Communications
Alberta Innovates - Technology Futures
250 Karl Clark Road | Edmonton | AB | T6N 1E4
780 450 5555 o
780 901 9754 c
allan.tesorio@albertainnovates.ca
www.albertainnovates.ca

**From:** Vivek Bhushan [mailto:bhushan@ualberta.ca]
**Sent:** Monday, March 14, 2011 11:53 AM
**To:** Allan Tesorio
**Subject:** RE: Seeking Permission to reproduce a diagram

Hi Allan,

Thank you very much for the response. Please find the image attached. The link to the image is:

http://www.globaloilsands.com/Processing/index.shtml

Thanks,
Vivek

**From:** Allan Tesorio [mailto:Allan.Tesorio@albertainnovates.ca]
**Sent:** March-14-11 11:48 AM
**To:** bhushan@ualberta.ca
**Subject:** FW: Seeking Permission to reproduce a diagram

Good morning Vivek,

I've received your request, and I can look into it for you. Do you have the image you can send to me, or do you have a current link to where the image is? We've gone through website changes with merger of our organization, and I'm not sure which image you would like to use.

Thank you kindly,
Allan

**Allan Tesorio | Communications Officer**
Communications
Alberta Innovates - Technology Futures
250 Karl Clark Road | Edmonton | AB | T6N 1E4
780 450 5555 o
780 901 9754 c
allan.tesorio@albertainnovates.ca
www.albertainnovates.ca

**From:** Vivek Bhushan [mailto:bhushan@ualberta.ca]
**Sent:** March 10, 2011 6:32 PM

**To:** Referral Mail
**Subject:** Seeking Permission to reproduce a diagram

Hi,

My name is Vivek Bhushan and I am a graduate student at University of Alberta. I wanted to put the bitumen production diagram available in your web site in my thesis for explanation purpose. The details are of the diagram is:

Sustainable Development of Oil Sands – Challenges in Recovery and Use, John R McDougall, Alberta Research Council, presentation to Western US Oil Sands Conference, 21 September 2006.( www.arc.ab.ca )

I am thus seeking permission. Please let me know if it is OK to put the diagram.

Thanks,
Vivek Bhushan,
MSc (Engineering Management)
University of Alberta, Edmonton”